

ABSTRACT

Title of Dissertation: CRYOGENIC TRAPPED-ION SYSTEM FOR
LARGE SCALE QUANTUM SIMULATION

Wen Lin Tan
Doctor of Philosophy, 2021

Dissertation Directed by: Professor Christopher Monroe
Joint Quantum Institute (JQI)
University of Maryland Department of Physics

One of the useful applications of a quantum computer is quantum simulation. While the quest for a universal quantum computer is still undergoing research, analog quantum simulators can study specific quantum models that are classically challenging or even intractable. These quantum simulators provide the opportunity to test particular quantum models and scale up the system size to gain insight into more exciting physics. The analog quantum simulator featured in this thesis is a cryogenic trapped-ion system. It serves the purpose of a large-scale quantum simulation by reducing the background pressure for storing a large ion chain with a long lifetime. This work presents the construction and characterization of this cryogenic apparatus and its performance as a trapped-ion quantum simulator.

Quantum information is encoded in the atomic state of the ion chain. The entangling operation in trapped ions uses the collective motion of the ion chain for quantum simulation. Therefore, it is imperative to develop a cooling mechanism to prepare the ion chain to near motional ground-state for achieving high

fidelity operations. Here, with this system, we explore another ground-state cooling mechanism with electromagnetically induced transparency (EIT) in a four-level system ($^{171}\text{Yb}^+$). EIT cooling allows simultaneous ground-state cooling across a bandwidth of motional modes, which it is useful in a large ion chain. Finally, we report the observation of magnetic domain-wall confinement in interacting spins chains. Such confinement is analogous to the color confinement in quantum chromodynamics (QCD), where hadrons are produced by quark confinement. We study the implications of such confinement in many-body spin system by observing the information propagation after applying a quantum quench of the confinement Hamiltonian. We also measure the excitation energy of domain-wall bound states from non-equilibrium quench dynamics. At the end of this experiment, we explore the number of domain wall excitations created with different quench parameters, which can be challenging to model with classical computers.

Cryogenic Trapped-ion System for Large Scale Quantum Simulation

by

Wen Lin Tan

Dissertation submitted to the Faculty of the Graduate School of the
University of Maryland, College Park in partial fulfillment
of the requirements for the degree of
Doctor of Philosophy
2021

Advisory Committee:

Professor Christopher Monroe, Chair/Advisor

Professor Norbert M. Linke

Professor James Williams

Professor Alexey Gorshkov

Professor Christopher Jarzynski

© Copyright by
Wen Lin Tan
2021

For Mom and Dad

Acknowledgments

Every single Ph.D. journey has its very own story. My Ph.D. story has its ups and downs. I am incredibly grateful to have crossed paths with everyone. In this journey, I have learned a lot. The complete list of people to thank for is exceptionally long. This acknowledgment does not do justice to everyone, but here is my sincere gratitude to you all. Thank you, and I hope to stay in contact with all of you.

First and foremost, I want to thank my advisor Chris Monroe for the excellent opportunity to work in his lab at the University of Maryland, College Park (UMD). I attend graduate school because I enjoy working with trapped ions and Chris' group is surrounded by many trapped-ions experts who I can learn a lot from them. Chris has the right balance of being hands-off and present, which greatly benefits me as a researcher. At the start of my Ph.D., I remember expressing to Chris that I would like to work in his group's Cryogenic Quantum Simulation (Cryo) lab. Till now, I still appreciate that Chris assigned me to this lab because I learn to build a lab and perform trapped-ion experiments. In addition, with Chris's support, I can focus full-time on research from the start. Therefore, I thank Chris for my comprehensive Ph.D. experience.

I also thank my undergraduate advisor, Boris Blinov for the research opportunity in his lab at the University of Washington (UW), Seattle, marking the beginning of my journey with trapped ions. I am thankful for the hands-on research experience as an undergraduate, which prepared me well for grad school. One of my fondest memories of Boris is when I asked him if I should accept the offer from the UW

Physics graduate school and continue researching in his lab or join the Joint Quantum Institute (JQI) at UMD. Without any hesitation, he advised me to join JQI for Chris' group. He even jokingly mentioned 'kicking' me out from his lab would greatly benefit me. And thus, I left the city I love – Seattle.

The next person that I am thankful for is Guido Pagano. He was a postdoctoral researcher for Cryo when I first joined. Building an experiment is not the easiest task, especially a cryogenic trapped-ion system (hopefully, it gets easier when going cryo is prevalent). We faced failures in building this system. However, Guido's resilience taught me that failures are expected, but a person's reaction in solving the problem makes a difference. Here, I wish the best for his trapped-ion group at Rice University. I also thank Phil Richerme and Paul Hess for designing and building the Cryo lab and Harvey Kaplan, the first grad student in this lab, who made everything more fun!

Next, I appreciate the support from the whole Quantum Simulation (QSim) team for the collaboration, support, and friendship developed over the years. It made collaboration between both QSim labs fun. Special thanks to Antonis Kyprianidis, Patrick Becker, Kate Collins, William Morong, Jiehang Zhang, Lei Feng, Arinjoy De, Abhishek Menon, Albert Chu, Nate Dudley, Daniel McVicker, Micah Hernandez, and Eric Birckelbaw. The QSim experiment is not complete without the theory team. Thanks to Alexey Gorshkov, Fangli Liu, Rex Lundgren, and Seth Whitsitt.

Furthermore, I would like to thank the rest of my awesome lab mates (past and present) for the knowledge, help, and support. In no particular order, they are Daiwei Zhu, Allison Carter, Drew Risinger, Qingfeng (Kee) Wang, Marko Cetina, Ken

Wright, Kevin Landsman, Sophia Scarano, Laird Egan, Jameson O'Reilly, Debopriyo Biswas, Sagnik Saha, George Toh, Ksenia Sosnova, Michael Goldman, Marty Lichtman, Clayton Crocker, Caroline Figgatt, Steven Moses, Jason Amini, Jonathan Mizrahi, Volkan Inlek, and Shantanu Debnath. Furthermore, I thank Kristi Beck and David Wong-Campos for being amazing mentors and friends. Your advice has much helped me! Thank you to Crystal Noel for all the support and I wish you success with your future trapped-ion group. I also appreciate the awesome Samantha Suplee as the former lab manager, who helped us in administrative tasks, and is a great friend. Besides that, I thank Norbert Linke and his trapped-ion group. Thank you for the hospitality, and I wish the best for your group too.

Most importantly, the end of my Ph.D. journey would not have been possible without the committee members: Chris Monroe, Alexey Gorshkov, Norbert Linke, Chris Jarzynski, and Jimmy Williams. Thanks!

Moreover, I am grateful for my mentor, Beth Etscheid. Thank you for being there and give me advice. Also, I thank Dr. Susan Martin from the UMD Graduate School, University Career Center & The President's Promise for the support in my career development. Additionally, I would like to express my gratitude to Jenni, Matt. B, Zishuo, Jing Ying, Sieh Yen, Andrea, Karen, Nate, Lily the Cat, and Rini for all the support!

Finally, I would like to thank my parents, and thus, this thesis is dedicated to them. Words cannot fully describe my gratitude towards both of you all. Still, thanks a lot!

Table of Contents

Dedication	ii
Acknowledgements	iii
List of Figures	ix
List of Abbreviations	xii
1 Introduction	1
1.1 Chapter Summary	2
2 Experimental System - Part I	5
2.1 $^{171}\text{Yb}^+$ Ion for Quantum Simulation	5
2.1.1 Doppler Cooling	5
2.1.2 Optical Pumping and Detection	7
2.2 The Fundamentals of RF Trap	8
2.3 Motional Modes of the Trapped Ions	13
2.4 Experiment Linear RF-Blade Trap	14
2.4.1 A Brief History of Traps Used in this Lab	18
2.4.2 Segmented and Unsegmented RF trap COMSOL analysis along the axial direction of the RF-blade trap	19
2.4.3 Trap #2	24
3 Experimental System - Part II	28
3.1 Introduction	28
3.2 The Cryostat	29
3.3 Cooling-down procedure	32
3.4 Warm-up and cryostat-moving procedure	35
3.5 Helical Resonator	38
3.6 RF stabilization	43
3.7 Characterization of cryogenic vacuum	45
3.7.1 Inelastic collision	48
3.7.2 Elastic collision	49

3.7.3	Other Methods	51
3.8	Characterization of the vibration in the system	52
3.9	Coherence lifetime of the system	57
3.10	Maintenance	59
3.10.1	VIS Maintenance	59
3.10.2	Cold head Maintenance	61
3.10.3	Filter water and chiller	63
4	Quantum Simulations Toolbox	67
4.1	Two-level System	68
4.2	Three-level System	69
4.2.1	Time-Dependent Schrödinger Equation	71
4.2.2	Adiabatic Elimination - Two-level Dynamics	73
4.2.3	Carrier Transition	74
4.2.4	Sideband Transitions	74
4.3	Generating Long-Range Transverse Field Ising Model	76
4.3.1	Ising Interaction	76
4.3.2	Ising Interaction with Transverse B-fields	80
4.3.3	Cross Terms of Magnus Expansion	80
4.4	Details about the experiment on Raman	83
4.4.1	Estimation of the angle between a principal axis to Raman	83
5	Ground-state Cooling	85
5.1	Resolved sideband cooling	85
5.2	Electromagnetically induced transparency (EIT) cooling	88
5.2.1	Three-level system for EIT cooling	88
5.2.2	EIT Cooling in a Tripod System	94
5.2.2.1	Simplification from four-level tripod system to effective Λ system	95
5.2.2.2	Four-level tripod numerical result	97
5.2.2.3	Four-level tripod experimental result	98
5.2.2.4	EIT calibration and qualitative discrepancy in numerical and experimental data	107
6	Analog Quantum Simulation	111
6.1	Information propagation	111
6.2	Confinement model	112
6.2.1	Analogy of confinement in with the Ising model	114
6.2.2	Long-range TFIM for Confinement	116
6.3	Experimental results of Confinement	118
6.3.1	Information Propagation due to the Effects of Confinement	120
6.3.2	Bound-state Energies of Low Energy States	124
6.3.2.1	Initial State and Measurement	126
6.3.2.2	Extracting Oscillation Frequencies	129
6.3.3	Number of Domain Walls at Various B-field Strength	132

6.3.4	Domain-walls number at large B-field and at infinite temperature	133
6.4	Summary	136
	Bibliography	137

List of Figures

2.1	Energy levels of $^{171}\text{Yb}^+$ ion.	6
2.2	Doppler cooling, optical pumping, detection schemes for $^{171}\text{Yb}^+$ ion. . .	9
2.3	Linear RF trap in a cryogenic setup.	11
2.4	Wire bonding electrode.	15
2.5	Two different CAD designs of the linear RF-blade trap.	16
2.6	Trap #1 with both enriched ^{171}Yb and natural Yb abundance ovens near the trap.	17
2.7	Cross-section view of the cryostat.	20
2.8	Aftermatch of DAC malfunction on the oven.	21
2.9	Axial view of the trap model for COMSOL.	22
2.10	COMSOL potential simulations for the segmented and unsegmented RF traps along the axial (x) direction of the yz -center of the trap. . .	23
2.11	Trap frequencies were measured with two counter-propagating Ra- man beams to probe the motional modes of the ion chain.	25
3.1	The cryostat that houses the RF trap.	32
3.2	Helium gas to VIS.	36
3.3	Water condensation on the re-entrant window (imaging window). . .	37
3.4	Electrical connections to the RF trap in the 4 K region.	39
3.5	Resonator design.	40
3.6	Resonator performance at different temperatures.	41
3.7	Allan deviation of the voltage difference between the reference signal and the input to the PID box ϵ at different averaging/integrating time τ	44
3.8	A chain of ions.	47
3.9	Inelastic collision measurements per ion γ_{in} at different temperatures with 33 ions for a time period varying from 3-12 hours.	50
3.10	Elastic collision γ_{el} per ion as a function of the energy barrier $\Delta\omega$ between ‘zig’ and ‘zag’. configurations at different temperatures. . .	52
3.11	Michelson interferometers for vibration measurement along x, y, z di- rections of the apparatus.	53
3.12	Vibrations along the three principal axes of the trap.	54

3.13	Vibration improvement after adding mechanical support on the resonator.	55
3.14	Finite element analysis of the mechanical structure of the system. . .	56
3.15	Raman coherence with Ramsey.	58
3.16	VIS maintenance.	60
3.17	Water in VIS.	61
3.18	4.6 hours drift measurement of a single ion, taken by the imaging camera.	62
3.19	The x and y ion displacements with time.	63
3.20	Cold head.	64
3.21	Chiller to compressor.	65
4.1	Stimulated Raman Transition in a Λ -system.	70
4.2	Raman orientation with respect to the principle axes of the trap. . . .	84
5.1	Raman sideband cooling.	87
5.2	EIT cooling of the three-level system.	89
5.3	EIT cooling with dressed State.	93
5.4	EIT cooling in $^{171}\text{Yb}^+$	95
5.5	Numerical calculation of the four-level tripod system of $^{171}\text{Yb}^+$ for EIT cooling with Rabi frequencies $\Omega_{-1} = 0.7\Gamma$, $\Omega_0 = 0.35\Gamma$, $\Omega_1 = 2.0\Gamma$ and detunings $\Delta_{-1} = 3.69\Gamma$, $\Delta_0 = \Delta_1 = 4.47\Gamma$	97
5.6	Numerical result of average phonon number with EIT cooling.	99
5.7	EIT laser configuration in the experiment.	100
5.8	EIT cooling performance of a single ion.	101
5.9	Long ion chain EIT cooling performance.	103
5.10	The red (in red) and blue (in blue) Raman sideband spectra of 31-ions chain after 2 ms of Doppler cooling.	104
5.11	The performance of three different cooling schemes with a 36 ion chain characterized with a motion-sensitive carrier Rabi oscillations. .	106
5.12	Ramsey measurement for calibrating EIT cooling beams.	108
5.13	Coupling from polarization impurity.	110
6.1	Hadronic particles.	113
6.2	Domain-wall confinement analogy to color confinement in QCD. . . .	115
6.3	Confining potentials in the short-range and long-range TFIM are drawn for visualization.	117
6.4	Effective confining potential and experiment sequence.	121
6.5	Confinement dynamics at $B/J_0 \approx 0.75$, $L = 11$	123
6.6	Initial states that predominantly overlap with the low-energy eigenstates of the confinement Hamiltonian.	125
6.7	Low-energy excited states.	127
6.8	$\Delta E_{0,1}/J_0$ of all system sizes L at $B/J_0 \approx 1$ for Fig. 6.7 f).	128
6.9	$\Delta E_{0,1}/J_0$ extracted from Lorentzian fit in different system sizes L . .	130

6.10	The Fourier-transformed spectrum of the bound-state energies with three different initial center-domain-size states in the $L = 11$ spin chain.	131
6.11	Evolution of domain wall population.	134
6.12	Number of domain walls in two dynamical regimes.	135

List of Abbreviations

AOM	Acousto-optic modulator
CAD	Computer-aided design
COM	Center of mass
DAC	Digital-to-Analog Converter
DC	Direct current
EIT	Electromagnetically induced transparency
EMCCD	Electron Multiplying Charge-Coupled Device
EOM	Electro-optic modulator
LRTFIM	Long-Range Transverse Field Ising Model
PCB	Printed Circuit Board
QCD	Quantum Chromodynamics
RF	Radiofrequency
RSC	Resolved sideband cooling
RWA	Rotating Wave Approximation
TFIM	Transverse Field Ising Model
UHP	Ultra-High-Purity
UHV	Ultra-High Vacuum
VIS	Vibration Isolation System
VVA	Voltage Variable Attenuator
XHV	Extreme High Vacuum

Chapter 1: Introduction

Trapped ions platform is a promising candidate for quantum computing [1, 2] and quantum simulations [3] for its long coherence time [4, 5], high fidelity qubit state detection [6, 7], and entanglement [8]. Despite all these accomplishments in this field, many improvements are still needed. Scalability remains a challenge. As the number of qubits increases, high fidelity detection can be compromised due to detection crosstalk [9], and entanglement schemes can get more complex [10], especially in performing quantum computing. Analog quantum simulation, on the other hand, has less restricted requirements. A quantum simulator may not be a universal quantum computer, but it can be tailored to study quantum physical models, notably the quantum Ising model in this thesis.

Furthermore, for quantum computing and quantum simulations in trapped ions, the quality of the ultra-high vacuum (UHV) in the apparatus can limit the lifetime of the ion chain due to background gas collisions with the chain. Such collisions decrease the lifetime of the chain as the system size gets larger. One of the brute force methods to overcome this challenge is to build a cryogenic ion trap to reduce the pressure in the vacuum by cryo-pumping. Hence, the work in this thesis focuses on analog quantum simulations with long ion chain in a cryogenic ion trap.

Throughout the lifetime of this experiment [11], we have demonstrated a significant longer ion chain lifetime relative to its predecessor, the room-temperature quantum simulation apparatus. However, integrating a cryostat into the ion trap system adds complications in building the system. Therefore, this thesis will serve as a guide in building a better next-generation cryogenic ion trap.

As an experimental physics graduate student, I am fortunate to build this apparatus and learn physics with analog quantum simulations. The chapters in this thesis are arranged to include the constructions of the apparatus till the quantum simulation experiments that we have done with this device.

1.1 Chapter Summary

Chapter 2

Chapter 2 introduces the fundamentals of ion trapping, including $^{171}\text{Yb}^+$ as the qubit and the linear RF-blade trap for trapping ions. In this lab, we have cycled thru three RF-blade traps in which this chapter will describe the characteristics of such RF traps. Notably, this chapter also explores the implication of segmented and unsegmented RF blades in such trap design with the COMSOL simulation. Finally, it provides the measured performance of trap #2.

Chapter 3

This chapter introduces the cryogenic apparatus, which provides a cryogenic environment (4 K-10 K) to the RF trap. It first presents the motivation and details of the cryogenic trapped-ion system. Following the building of the RF trap in

a cryostat, it features the performance of the system, specifically the pressure improvement compared to the room-temperature counterpart of this experiment. With the improved pressure around the ion trapping region, the cryostat also introduces vibration into the system. We have characterized and measured the consequences of such vibration with a Raman Ramsey test. Finally, we describe the maintenance required for this system.

Chapter 4

Chapter 4 features the quantum simulations toolbox with a pair of counter-propagating Raman beams to perform arbitrary single-qubit rotation and entanglement between ions in the chain. With these basic operations, we then describe the generation of the long-range transverse field Ising model. This chapter ends with the extension of generating such model in the experiment . It also calculates the overlap of the principal axes of the RF trap to the Δk of the counterpropagating Raman beams.

Chapter 5

Before jumping ahead to the analog quantum simulation experiment, this chapter introduces another ground-state cooling mechanism with electromagnetically induced transparency (EIT). The motivation of EIT cooling is simultaneous ground-state cooling of motional modes within a bandwidth. It describes the theory behind EIT cooling in a three-level system and extends EIT cooling to a four-level tripod system, notably in $^{171}\text{Yb}^+$ [12]. By exploiting the concepts of EIT cooling in a three-level Λ system, the four-level tripod system can also be simplified to an effective three-level system. Following the theoretical and numerical studies of EIT

cooling, we experimentally implemented EIT cooling in the system. Finally, this chapter features the combination of resolved sideband cooling and EIT cooling that can decrease the total ground-state cooling time while achieving a low motional quanta of energy.

Chapter 6

At the end of this thesis, it features an analog quantum simulation experiment of “Domain-Wall Confinement and Dynamics in a Quantum Simulator” [13]. The effect of confinement here is similar to confinement in Quantum Chromodynamics (QCD), where the confining potential increases asymptotically without bound as the particles separate. In QCD confinement, quarks are confined into hadronic particles by the strong interaction that increases with particle separation. Compared to QCD confinement, the domain wall (the region between two anti-aligned spins) is analogous to quarks, and the bound pair of domain walls is similar to meson (a type of hadronic particles). We first study the consequences of such confinement in a many-body system by observing the information spreading and the excitation energy of domain-wall bound states from non-equilibrium quench dynamics. Finally, we go beyond the confinement regime to explore the number of domain walls after such quantum quenches with various transverse B -field strengths.

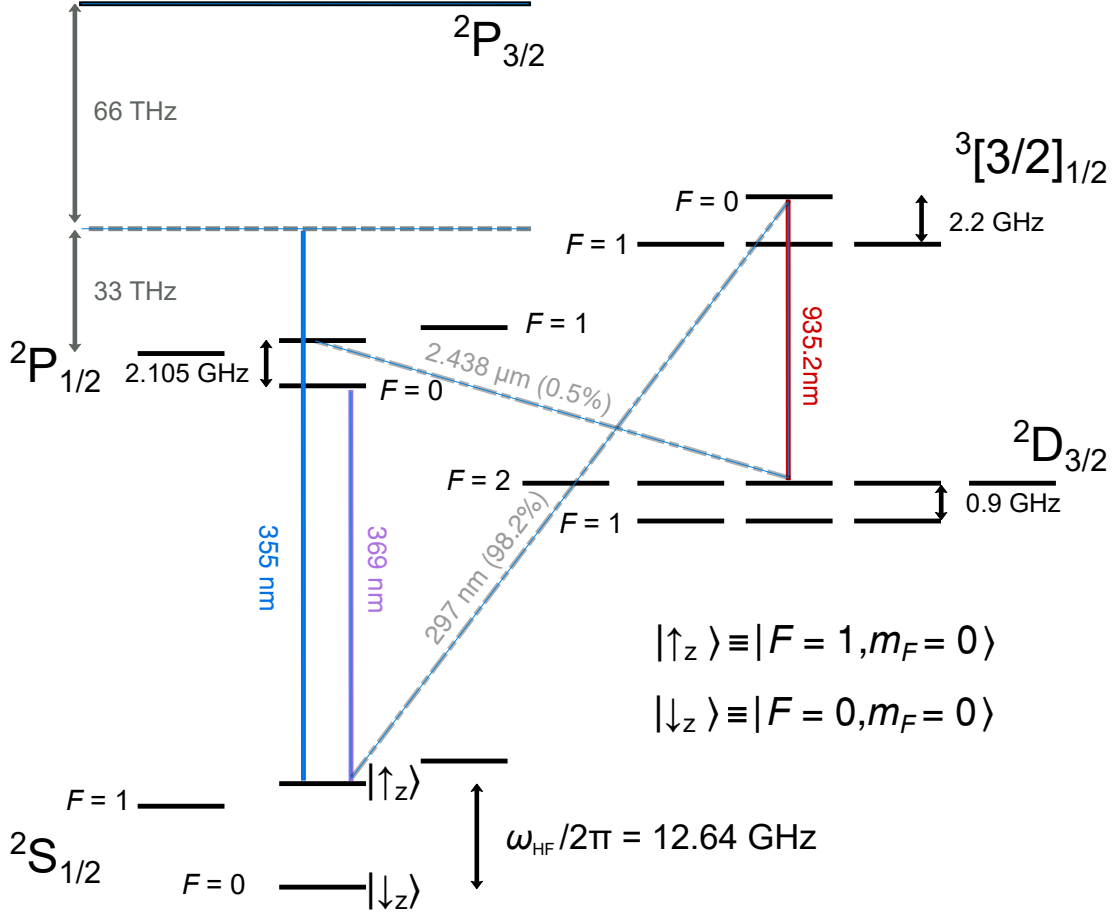
Chapter 2: Experimental System - Part I

2.1 $^{171}\text{Yb}^+$ Ion for Quantum Simulation

In the experiment, we trap $^{171}\text{Yb}^+$ ion, which has nuclear spin, $I = \frac{1}{2}$, in a RF trap. The quantum simulation experiments in this thesis work with spin- $\frac{1}{2}$ system. Each of the spin states is encoded in the two hyperfine states of the $^2\text{S}_{1/2}$ manifold as $|\downarrow_z\rangle \equiv |F=0, m_F=0\rangle$ and $|\uparrow_z\rangle \equiv |F=1, m_F=0\rangle$ (Fig. 2.1). In $^{171}\text{Yb}^+$ ion, the $^2\text{S}_{1/2} \leftrightarrow ^2\text{P}_{1/2}$ transition is almost a cycling transition, but there is a 0.5% of spontaneous emission events that the state decays to $^2\text{D}_{3/2}$. Therefore, to close the cycling transition, a 935 nm laser is on all the time to repump the state to $^3[3/2]_{1/2}$ and then decays back to $^2\text{S}_{1/2}$. Doppler cooling, optical pumping, and detection can be done by addressing the transition $^2\text{S}_{1/2} \leftrightarrow ^2\text{P}_{1/2}$ with a 369 nm laser [14, 15] (Fig. 2.2). We implement all these protocols by controlling the frequencies of the 369 nm light with Acoustic-optic modulators (AOMs) and Electro-optic modulators (EOMs).

2.1.1 Doppler Cooling

After loading $^{171}\text{Yb}^+$ ions from the oven, we Doppler cool these ions with a red-detuned 369 nm laser on $^2\text{S}_{1/2} \leftrightarrow ^2\text{P}_{1/2}$ transition (Fig. 2.2 a). The efficiency of



All frequencies listed are in $\omega/2\pi$, where ω is angular frequency.

Figure 2.1: Energy levels of $^{171}\text{Yb}^+$ ion. The $2S_{1/2}$ hyperfine manifold represents the spin states of the spin- $\frac{1}{2}$ system where $|\downarrow_z\rangle \equiv |F=0, m_F=0\rangle$ and $|\uparrow_z\rangle \equiv |F=1, m_F=0\rangle$ are separated by hyperfine splitting $\omega_{\text{HF}} = 12.64\text{GHz}$. The 369 nm laser addresses the transition from the $2S_{1/2} \leftrightarrow 2P_{1/2}$, which is used for cooling, optical pumping, and detection. There is 0.5 % chance for the state at $2P_{1/2}$ to decay to $2D_{3/2}$. To repump the state back into $2S_{1/2} \leftrightarrow 2P_{1/2}$, the 935 nm laser excites the state from $2D_{3/2}$ to $3[3/2]_{1/2}$, then the state decays back to $2S_{1/2}$. The off-resonant 355 nm Raman laser is used to perform coherent manipulation on the spin, which includes spin rotations and simulating spin- $\frac{1}{2}$ systems.

the Doppler cooling in reducing the average kinetic energy on the ions depends on the scattering rate from $^2P_{1/2}, F = 0$. The scattering rate¹ can be written as:

$$\gamma_s = \frac{s\gamma/2}{1 + s + 4(\Delta/\gamma)^2} \quad (2.1)$$

where the linewidth of $^2P_{1/2}$ $\gamma = 19.7$ MHz, saturation parameter $s = I/I_{sat}$, with I as the beam intensity and $I_{sat} = \frac{\pi\hbar c\Gamma}{3\lambda^3}$, c is the speed of light and \hbar is the Planck constant, and Δ is the detuning from the $^2S_{1/2}, F = 1 \leftrightarrow ^2P_{1/2}, F = 0$ transition. For optimal Doppler cooling that maximizes the scattering rate at $\Delta = \gamma/2$, the Doppler cooling temperature and average phonon numbers \bar{n} are:

$$k_B T = \hbar\Gamma/2 \quad (2.2)$$

$$\hbar\omega_m(\bar{n} + 1/2) = \hbar\Gamma/2$$

ω_m is the motional modes of the ion chain.

The Doppler cooling laser has all polarizations π and σ_{\pm} and is red-detuned from the transition between $^2S_{1/2}$ on $F = 1$ and $^2P_{1/2}$ on $F = 0$. For more efficient cooling in $^{171}\text{Yb}^+$, we also couple the states in the $F = 0$ in the $^2S_{1/2}$ manifold for Doppler cooling (Fig. 2.2 a) with the second sideband of a 7.14 GHz EOM².

2.1.2 Optical Pumping and Detection

The spin states are initialized to $|\downarrow_z\rangle$ via optical pumping [14]. The first sideband of the 2.105 GHz EOM excites the state from $^2S_{1/2}$ on $F = 1$ and $^2P_{1/2}$ on $F = 1$, then the state of the spins will decay to $|\downarrow_z\rangle$ (Fig. 2.2 b). This process will

¹The scattering rates formula here is derived from the steady-state solution of the Optical Bloch equation for a two-level system [16]. A detailed derivation of two-level system Doppler cooling is shown in [17, 18]. One can also find the optimal Doppler cooling parameters in $^{171}\text{Yb}^+$ ion as a function of B -field to include the Zeeman levels at the $F = 1$ of the $^2S_{1/2}$ manifold.

²There was no 14.7 GHz EOM when we set up the lab. Nowadays, 14.7 GHz EOM is commercially available for 369 nm.

continue till all the states are in $|\downarrow_z\rangle$. From here, the spin states can be prepared to product states along any axis of the Bloch sphere by applying rotation pulses with microwave or Raman operations.

We detect the state of the spins in ion chain by collecting the spin-dependent fluorescence on an Andor IXon Ultra 897 EMCCD camera with site-resolving imaging. A resonant 369 nm laser between $^2S_{1/2}$ on $F = 1$ and $^2P_{1/2}$ on $F = 0$ is shined during state detection. Photons are scattered off when the spin state is in $|\uparrow_z\rangle$, but a negligible number of photons is scattered when the qubit is in $|\downarrow_z\rangle$ (Fig. 2.2 c). We can rotate the measurement along with any basis using global rotation pulses, which allows the measurement of all individual magnetizations and many-body correlators along any single axis.

At the beginning of the data taking, we calibrate the number of photons scattered from the bright $|\uparrow_z\rangle$ and dark $|\downarrow_z\rangle$ states of each spin to find the binary threshold for spin-state discrimination. The bright and dark states of the setup in this thesis have an average fidelity $> 97\%$, which is sufficient for the quantum simulation experiments described here³. The dominant error sources here are off-resonant mixing of spin states during detection, crosstalk between adjacent ions, electronic camera noise, and laser noise.

2.2 The Fundamentals of RF Trap

Based on one of Maxwell's equations, $\nabla \cdot \vec{E} = 0$, the electric field has no divergence in a region with no free charge density. From this equation, Earnshaw

³For quantum computing purposes, a higher state detection fidelity $> 99\%$ in $^{171}\text{Yb}^+$ can be achieved [7].

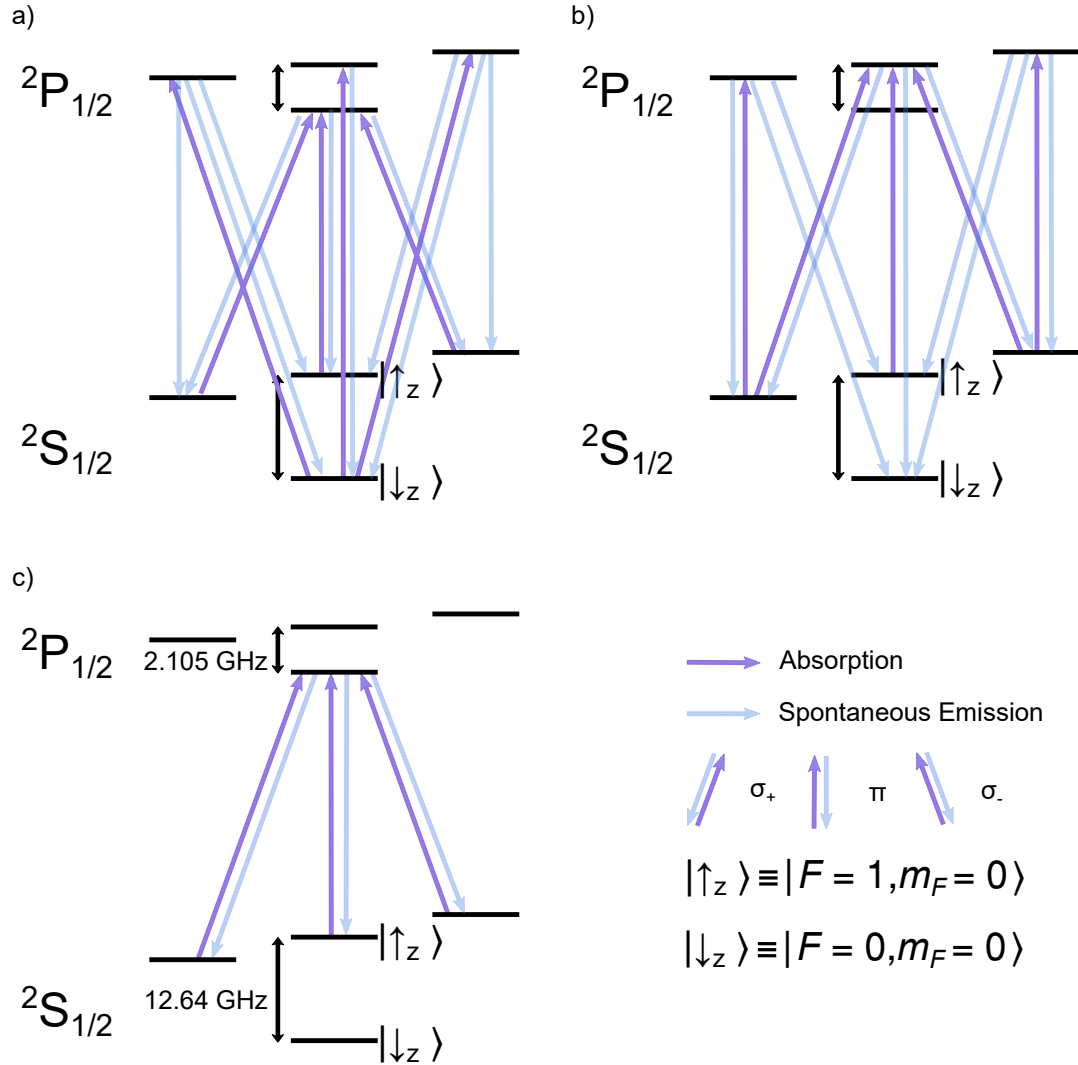


Figure 2.2: Doppler cooling, optical pumping, detection schemes for $^{171}\text{Yb}^+$ ion. a) Doppler cooling: the second-order sideband of the 7.14 GHz EOM pumps the states out from $^2S_{1/2}, F=0$ to $^2P_{1/2}, F=1$. b) Optical pumping: the first-order sideband of 2.15 GHz EOM is applied to the resonant light of the $^2S_{1/2} \leftrightarrow ^2P_{1/2}$ transition to excite the state to the $F=1$ of the $^2P_{1/2}$ manifold. Optical pumping continues till all the states decay to $|\downarrow_z\rangle$. c) Detection: resonant light of $^2S_{1/2}, F=1$ to $^2P_{1/2}, F=0$ transition is shined to the ion chain for spin-dependent detection. Scattered photons indicate the state is in $|\uparrow_z\rangle$. Conversely, detecting a negligible number of photons indicates the state is in $|\downarrow_z\rangle$.

proved that a charged particle could not be confined in all directions simultaneously in a static electric field. However, a combination of static electric and magnetic fields (Penning trap) or oscillating electric fields (RF trap) can confine charged particles. Here, this experiment focuses on RF trap. In the experiment, we use a linear RF trap with four gold-plated blades, which consist of two RF blades and two-segmented static blades electrodes (Fig. 2.3). The total potential of the RF trap is first simulated using finite element techniques with COMSOL, and the properties of the trap are studied experimentally. However, for simplicity in understanding a linear RF trap [19], the total potential at the center of the trap is:

$$V(x, y, z, t) = \underbrace{\frac{\kappa V_0}{2} \left(1 + \frac{x^2 - y^2}{R^2}\right) \cos \Omega_d t}_{V_1} + \underbrace{\frac{\rho U_0}{Z_0^2} \left(z^2 - \frac{x^2 + y^2}{2}\right)}_{V_2} \quad (2.3)$$

where κ and ρ are the geometric factors that depend on the trap geometry and the orientation of the RF and static electrodes of the ion trap. The V_0 (U_0) is the RF drive amplitude (axial) voltage, R (Z) is the transverse (axial) distance from the ion to the electrode, and Ω_d is the RF drive frequency. In this derivation, x and y are the transverse directions of the trap, and z is the axial direction, which is along the trap axis. V_1 from Eq. 2.3 describes the time-varying potential near the axis of the trap that the gradient of the electric fields yields the effective pseudopotential, which confines the ion chain radially. V_2 in Eq. 2.3 is a static potential that traps the ion chain axially. From Eq. 2.3, the total electric field is

$$\mathbf{E}(x, y, z, t) = -\frac{\kappa V_0}{R^2} \begin{bmatrix} x \\ -y \\ 0 \end{bmatrix} \cos \Omega_d t - \rho \frac{U_0}{Z_0^2} \begin{bmatrix} -x \\ -y \\ 2z \end{bmatrix} + \begin{bmatrix} E_x \\ E_y \\ E_z \end{bmatrix}.$$

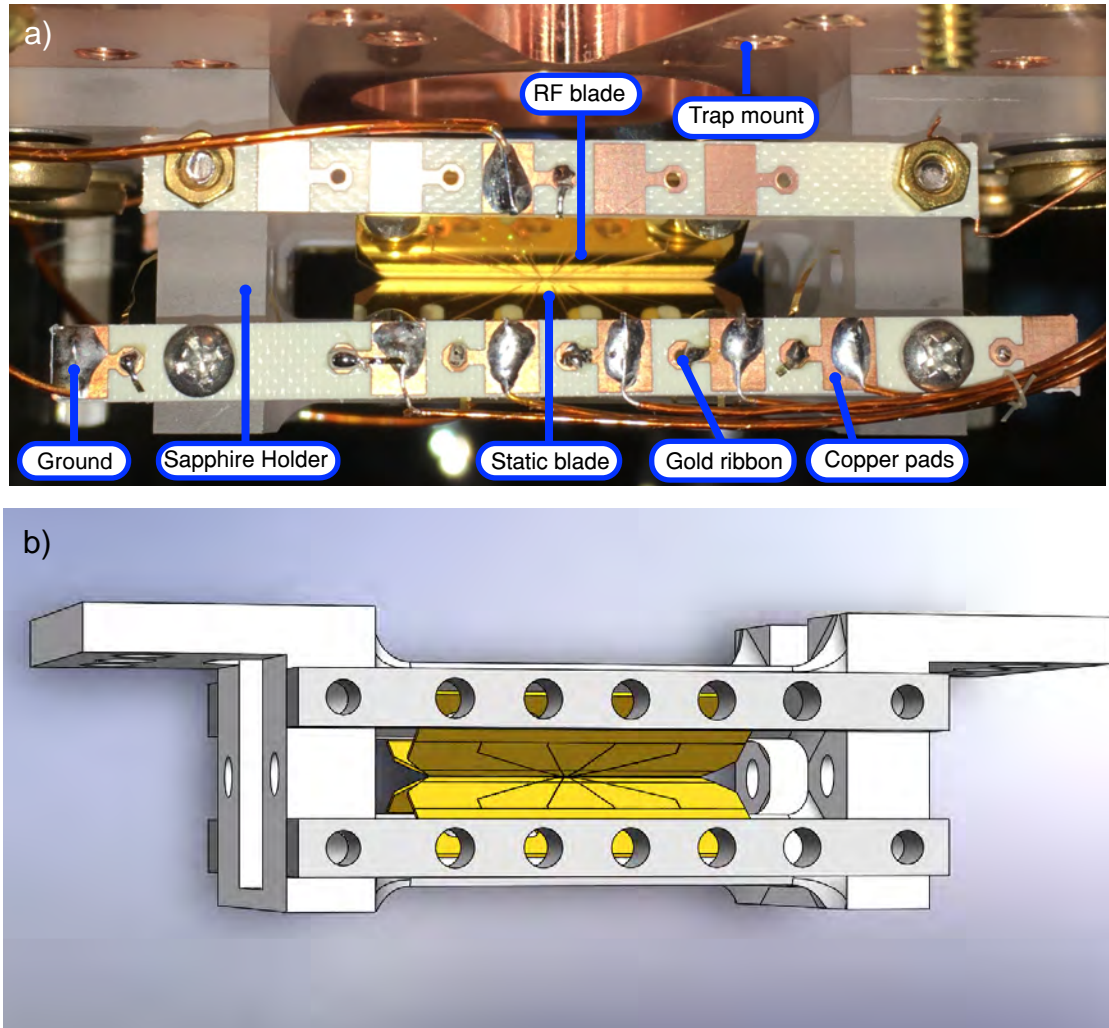


Figure 2.3: Linear RF trap in a cryogenic setup. a) The physical mounting of the linear RF trap with four gold-plated blades. b) The CAD model of the linear RF trap in a).

Here, we assume $E_x = 0$, $E_y = 0$, $E_z = 0$. Using the total electric field, we can find a set of equations of motion for a single ion with charge e that resembles the Mathieu equation [20]:

$$\begin{bmatrix} \ddot{x} \\ \ddot{y} \\ \ddot{z} \end{bmatrix} + \frac{\Omega_d^2}{4} \begin{bmatrix} a_x x + 2q_x \cos(\Omega_d t) x \\ a_y y + 2q_y \cos(\Omega_d t) y \\ a_z z + 2q_z \cos(\Omega_d t) z \end{bmatrix} = 0 \quad (2.4)$$

where $a_x = a_y = -\frac{1}{2}a_z = -\frac{4e\rho U_0}{mZ_0^2\Omega_d^2}$ and $q_x = -q_y = \frac{2e\kappa U_0}{mR^2\Omega_d^2}$, $q_z = 0$. By making the substitution of $\Omega_d t = 2\tau$, Eq. 2.4 is in the form of $\ddot{u} + (a_u + 2q_u \cos(2\tau))u = 0$. The stable solution of the Mathieu equation can be expressed as:

$$u(\tau) = P_1 \sum_{n=-\infty}^{\infty} C_{2n} \cos((2n + \beta)\tau) + iP_2 \sum_{n=-\infty}^{\infty} C_{2n} \sin((2n + \beta)\tau) \quad (2.5)$$

where P_1 and P_2 depend on the initial conditions. β and coefficient C_{2n} can be solved by plugging this stable solution into the Mathieu equation. The details of this calculation can be found in [21, 22] with the assumption all the $|a| \ll 1$ and $|q| \ll 1$. The solution of Eq. 2.4 can be approximated as

$$\begin{bmatrix} x(t) \\ y(t) \\ z(t) \end{bmatrix} \approx \begin{bmatrix} x_1 \cos(\omega_x t + \phi_x) [1 + \frac{q_x}{2} \cos(\Omega_d t)] \\ y_1 \cos(\omega_y t + \phi_y) [1 + \frac{q_y}{2} \cos(\Omega_d t)] \\ z_1 \cos(\omega_z t + \phi_z) [1 + \frac{q_z}{2} \cos(\Omega_d t)] \end{bmatrix} \quad (2.6)$$

where x_1 , y_1 , z_1 are the first-order amplitude of the ion positions in all directions, $\phi_{x,y,z}$ are the phases that determine by the initial conditions of Eq. 2.4 and $\omega_{x,y,z} \approx \frac{1}{2}\Omega_d \sqrt{a_{x,y,z} + \frac{1}{2}q_{x,y,z}^2}$ are the secular frequencies of the ion in all directions. Therefore, for a single ion case, the ion will experience a secular motion in a harmonic oscillation with frequencies $\omega_{x,y,z}$ and amplitude x_1, y_1, z_1 for each direction. Furthermore, due

to the RF-field generating the pseudopotential for trapping ion, there is an ion motion depends on the $\cos(\Omega_d t)$. This is called the ‘intrinsic micromotion’ of the trap. In addition, a uniform static electric field (E_{dc}) or stray electric field can cause ‘excess micromotion’. Eq. 2.4 will be in the form $\ddot{u} + 2q_u \cos(2\tau)u = \frac{eE_{dc}\hat{u}}{m}$, where \hat{u} is a unit vector. The solution is approximated as:

$$\begin{bmatrix} x(t) \\ y(t) \\ z(t) \end{bmatrix} \approx \begin{bmatrix} (x_0 + x_1 \cos(\omega_x t + \phi_x)) [1 + \frac{q_x}{2} \cos(\Omega_d t)] \\ (y_0 + y_1 \cos(\omega_y t + \phi_y)) [1 + \frac{q_y}{2} \cos(\Omega_d t)] \\ (z_0 + z_1 \cos(\omega_z t + \phi_z)) [1 + \frac{q_z}{2} \cos(\Omega_d t)] \end{bmatrix} \quad (2.7)$$

which the excess micromotion term $(x_0, y_0, z_0) = \frac{eE_{dc}}{m} \cdot (\frac{\hat{x}}{\omega_x}, \frac{\hat{y}}{\omega_y}, \frac{\hat{z}}{\omega_z})$ with \hat{x} , \hat{y} and \hat{z} as unit vectors for all three directions of the trap. Depending on the degree of control on the static electric field of the trap, this excess micromotion term can be nulled by compensating the stray electric field with trap electrodes.

2.3 Motional Modes of the Trapped Ions

From section 2.2, the effective pseudopotential and static potential in RF traps confine the ions with secular frequencies, $\omega_{x,y,z}$, along each direction. As more ions are added, the ions in the chain will push each other away due to the Coulomb repulsion. When these two attractive and repulsive potentials balance out each other to have minimum energy, the ion chain will be in an equilibrium position. The notable configurations of the equilibrium position ion chain in this thesis are linear and zigzag ion chains. We mainly use a linear ion chain for quantum simulation purposes. The condition to obtain N number of ions in a zigzag chain is when

the ratio of the transverse frequencies ω_t to the axial frequency ω_{axial} , $\omega_t/\omega_{\text{axial}} < N/\sqrt{\log(N)}$ [23], where the ion chain is squeezed axially.

However, when the ion positions are perturbed from equilibrium, the ions will experience oscillations with respect to the equilibrium position. These oscillations can be Fourier transformed to find the normal modes of vibration in the N -ion chain, and there will be $3N$ motional modes which consist of two sets of transverse modes and one set of axial modes. The motional modes along the transverse directions are higher than the axial motional modes due to the stronger transverse confinement. The transverse center-of-mass (COM) motional mode is the highest transverse frequency. Conversely, the axial COM motional mode is the lowest frequency. In trapped-ion quantum computing, these motional modes mediate the spin-spin interaction via the Mølmer-Sørensen scheme [24,25] to generate entangled state in trapped ions. As for quantum simulation, this scheme is implemented where motional modes are off-resonantly excited to generate the Long-Range Transverse Field Ising Model (TFIM)⁴.

2.4 Experiment Linear RF-Blade Trap

In the experiment, we choose a linear RF-blade trap for its high optical access in all directions. The trap consists of two RF blades and two static blades. Each of the blades is made of alumina. They are coated with a 100 nm titanium layer followed by a $1\mu\text{m}$ layer of gold. Each blade is electrical-connected with a gold ribbon, which is wire-bonded onto the blade, and the other end of the ribbon is

⁴The details are in Chapter 4.

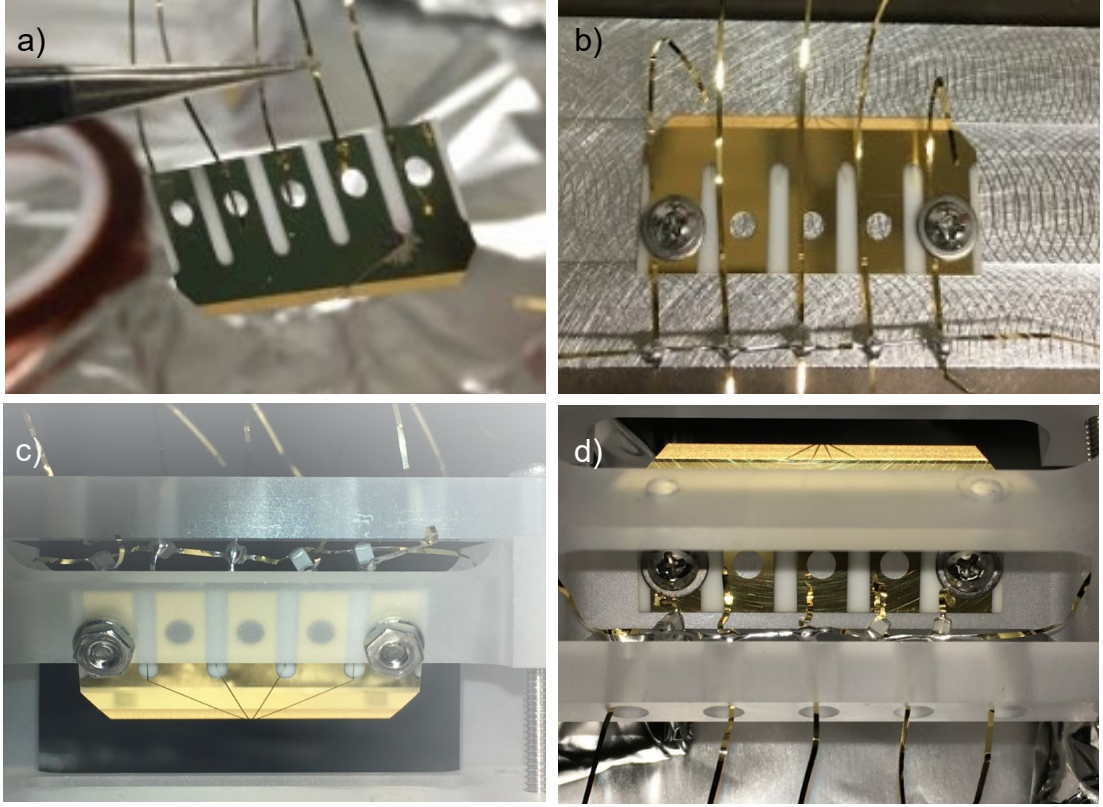


Figure 2.4: Wire bonding electrode. a) This an example of wire bonding a 0.015" wide and 0.001" thick gold ribbon onto a static blade with five different electrodes in it. b) We solder 800 pF capacitors for each static electrode to shunt RF pickup voltages. c) The blades are mounted on the sapphire holder. d) Each gold ribbons goes through the holes on the sapphire holder, and the other end of the ribbon are soldered to a copper pad (Fig. 2.3 b).

soldered to the copper pads (Fig. 2.3 and 2.4). These blades are mounted in $60^\circ/30^\circ$ configuration onto the sapphire holder, which also acts as an effective heat sink for the higher thermal conductivity of sapphire. The detail of the trap construction is in Ref. [11]. In the lab frame, the axial direction of the trap is x , and the transverse directions are y and z .

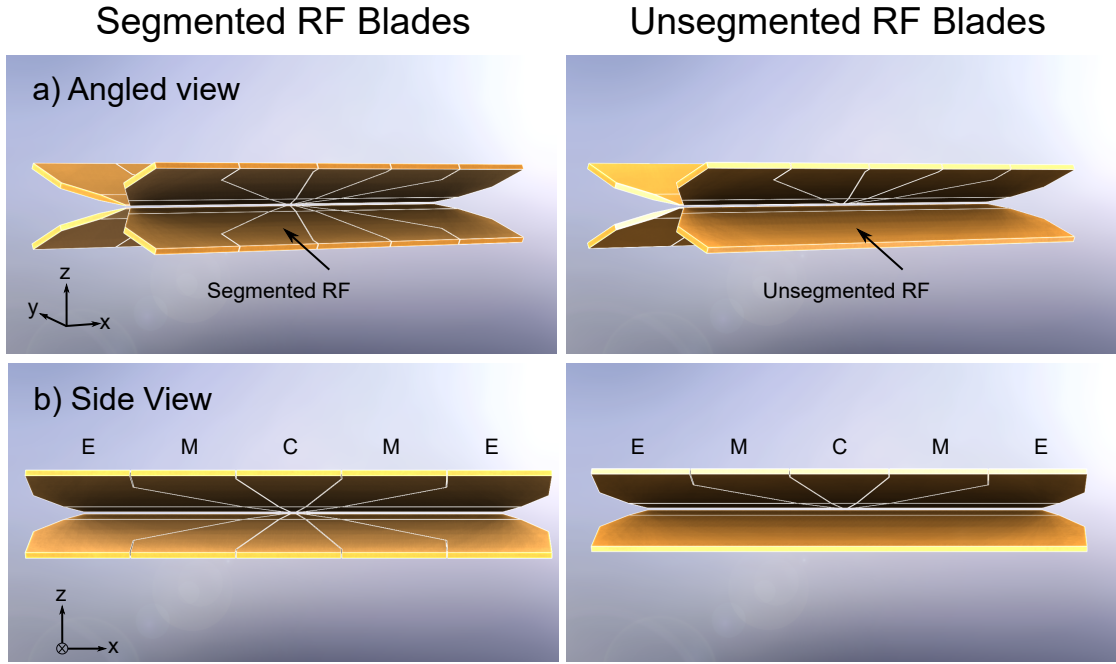


Figure 2.5: Two different CAD designs of the linear RF-blade trap. Both designs have two segmented static blades (each with five individually controlled electrodes) and two RF blades (each blade with a global RF bias). C (M, E) shows the center (mid, end) static electrodes. Left: The RF blades consist of a blade with five segments along the axial direction of the trapping region. Right: The RF blade consists of a blade with no segment. a) An angled view of the trap model in CAD. b) A side view of the trap model in CAD.

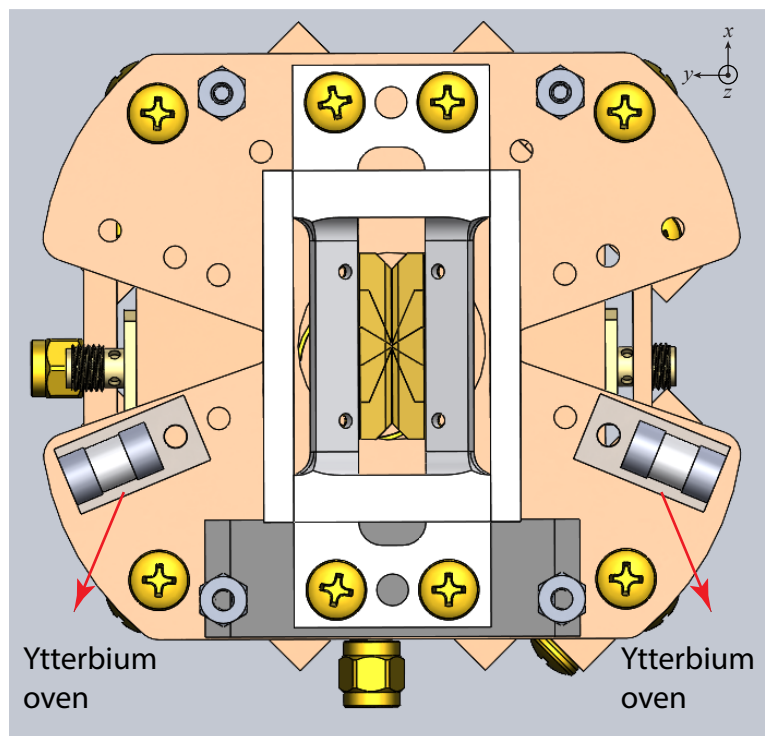


Figure 2.6: Trap #1 with both enriched ^{171}Yb and natural Yb abundance ovens near the trap.

2.4.1 A Brief History of Traps Used in this Lab

To date, we have used three variations of hand-aligned linear RF-blade traps. Each of them has four blades, with two as the static⁵ blades and another two as the RF blades. The same type of blades is aligned diagonally opposite with each other. The design of trap #1 and #2 are the same with their RF blades segmented (left of Fig. 2.5), unlike the unsegmented RF blades in trap #3 (right of Fig. 2.5).

Trap #1: The blades in this trap are damaged and are no longer in use. During the initial stage of the experiment setup, we placed the two Yb ovens (Fig. 2.6) near the RF trap, which were located at the 4 K stage of the cryostat⁶ (Fig. 2.6). The main flaw of having the ovens in the 4 K region was these ovens would heat the 4 K stage, and the trap would physically move due to thermal expansion/contraction. As a result, the alignment of the cooling lasers needed to be adjusted when the ovens are ramped up/down. After a few iterations of this inconvenient trapping process, the performance of trap #1 degraded as the gold coating on the blades was peeled off. We attribute this to the temperature gradient from the heating the oven and the 4 K environment of the trap.

Trap #2: This is the trap that we are currently using. It has the same design as Trap #1, but the enriched ¹⁷¹Yb oven is located at the room temperature section of the apparatus (Fig. 2.7). There is a line of sight between the oven and the ion trap at 4 K such that Yb flux can enter the trap during ion loading. One disadvantage of this setup is compromising the 4 K stage background pressure. This setup exposes

⁵Also known as constant voltage or DC in lab terms.

⁶The details of the cryostat will be explained in the next chapter.

the ion trap region to the room temperature vacuum region⁷. Ablation loading can be an alternative to oven loading in the cryogenic setup. With ablation loading, the 4 K region will be less exposed to the room temperature region, improving the overall pressure around the trap. Unfortunately, there was a DAC malfunction accident on the oven control. As a result, the trap was blasted and coated with Yb flux (Fig. 2.8)⁸. We cleaned up most of the Yb on the trap but the remaining Yb left has altered the electric field lines of the trap. Such change in the electric field lines is most prominent when we apply the 355 nm Raman beams in weak trap-axial confinement. The dielectric charging in the trap from the Raman beams pushes the ion chain along the axial direction.

Trap #3: This is a linear-blade RF trap. It uses unsegmented RF blades, unlike the previous traps. We are not using this trap. The combination of unsegmented RF blades with the segmented static electrodes creates an extra and unwanted axial confinement near the segmented regions. This results in the ion chain splitting into multiple sections, especially for large ion chain larger than the center electrode ($\approx 150\mu\text{m}$).

2.4.2 Segmented and Unsegmented RF trap COMSOL analysis along the axial direction of the RF-blade trap

The lab explores two different RF-blade trap designs: segmented and unsegmented RF traps with segmented static electrodes. The potentials of both trap

⁷We have 1×10^{-9} Torr pressure gauge on the room temperature vacuum region. The pressure of the room temperature region is on the order of 10^{-9} Torr, unlike the vacuum of the room-temperature apparatus that is $< 1 \times 10^{-11}$ Torr. Due to the low temperature and low background pressure from differential cryo-pumping, the background pressure of the cryogenic trap's surroundings is $\ll 1 \times 10^{-11}$ Torr.

⁸We kept the Yb coated window as our souvenir of this battle.

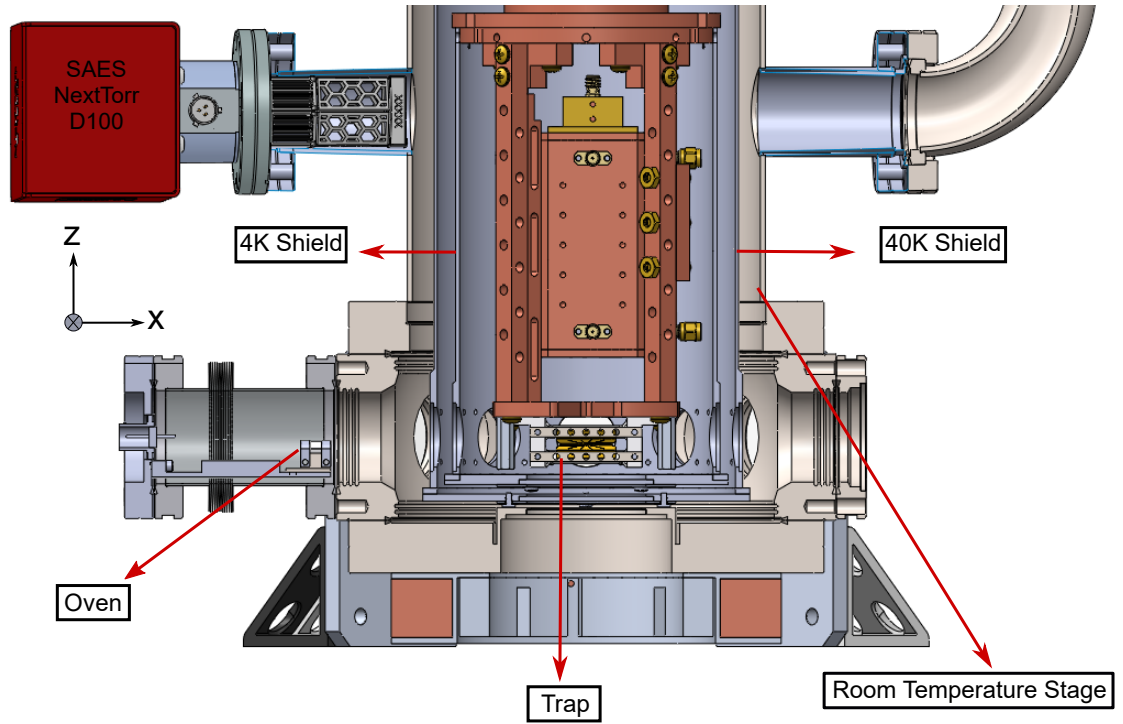


Figure 2.7: Cross-section view of the cryostat for the experimental region. It has both the 40 K and 4 K regions, which are enclosed by 40 K and 4 K shields. The oven is located outside the shields and in the room-temperature vacuum. The RF trap is in the 4 K region.

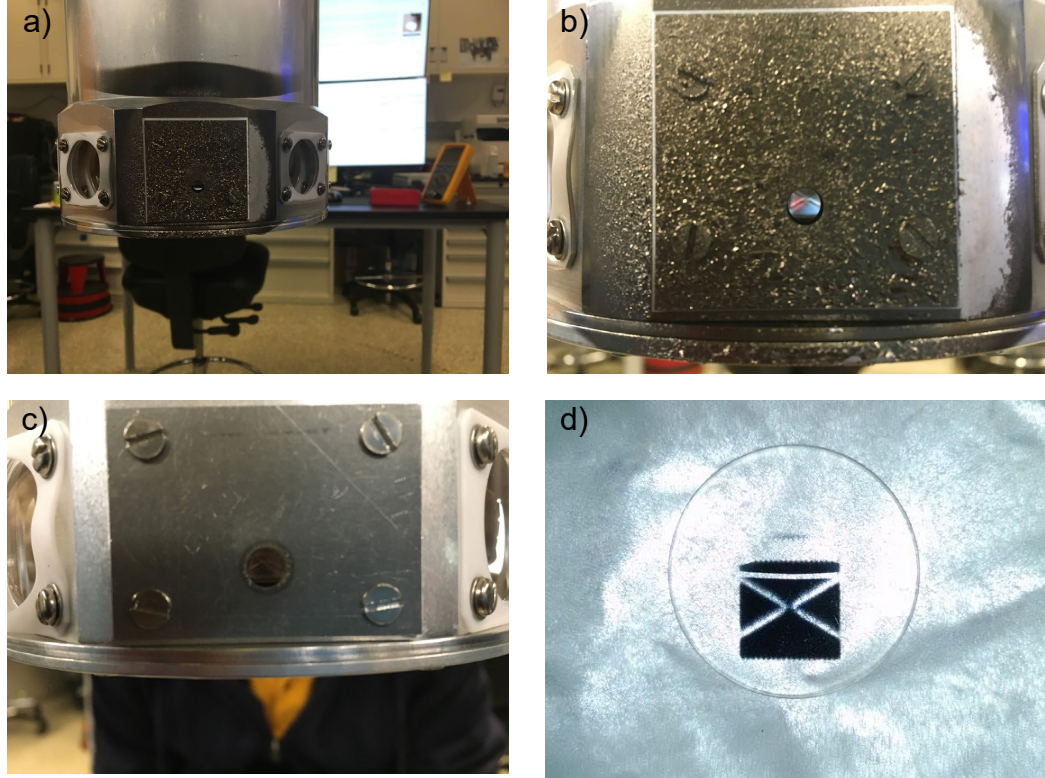


Figure 2.8: Aftermatch of DAC malfunction on the oven. a) This is the pinhole connecting the room temperature oven to the 40 K stage. b) Yb coated the 40 K pinhole. c) 4 K shield pinhole allowing Yb flux to enter the trap. d) Yb flux passed through the trap and imprinted on the window opposite the oven. A ‘negative image’ of the trap was formed.

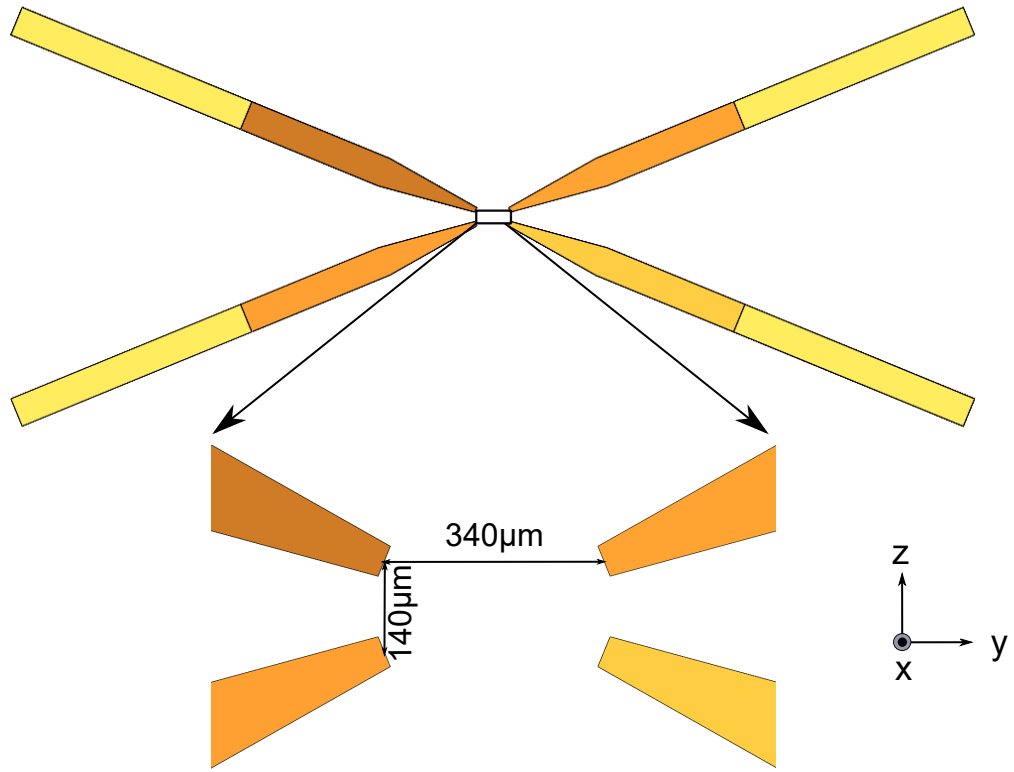


Figure 2.9: Axial view of the trap model for COMSOL. The distances between the tips of the electrodes are $340\mu\text{m}/140\mu\text{m}$. The bottom magnified view illustrates the distances between the tips of the electrodes

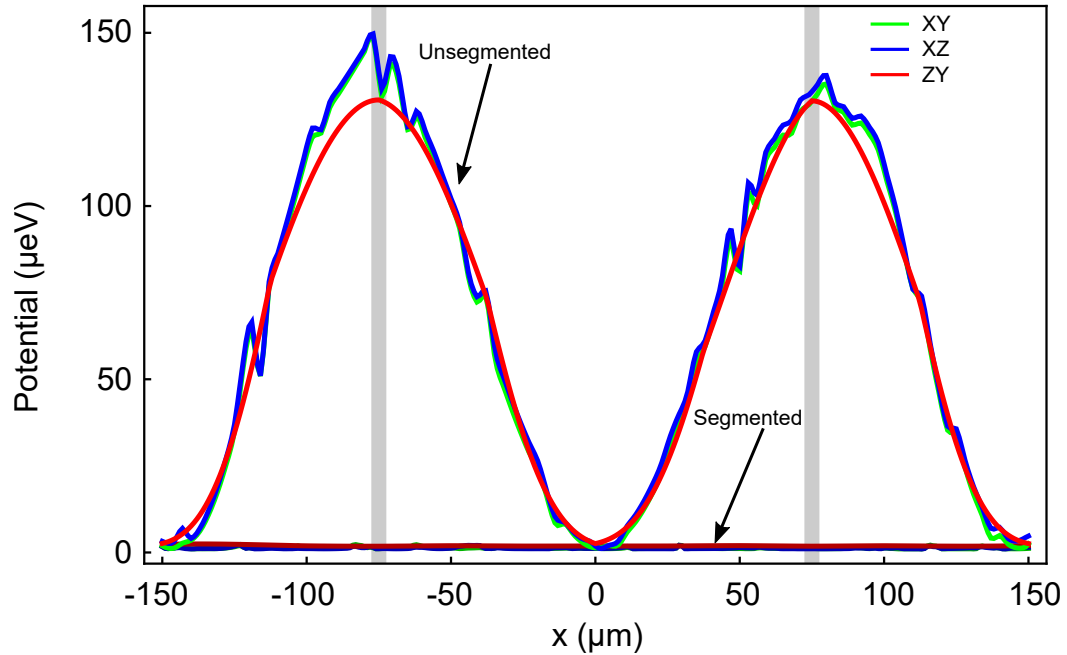


Figure 2.10: COMSOL potential simulations for the segmented and unsegmented RF traps along the axial (x) direction of the yz -center of the trap. The gray lines represent the gap locations between the center blades (length: $75\mu m$) and the two adjacent blades. The green (blue, red) displays the XY (XZ, ZY) potential along the x -direction of the trap. The segmented RF trap x -axis potential simulation (darker colors of green, blue and red) shows a more uniform potential along the x -axis. Conversely, the x -axis potential simulation of the unsegmented RF trap (lighter colors of green, blue and red) behaves sinusoidally.

designs are simulated with COMSOL. COMSOL provides a close approximation to the trap potential, although deviations from the simulation are expected as all the blades are hand-aligned. We import the CAD designs of the trap into COMSOL. For a direct comparison between the two models, the separation between electrodes (Fig. 2.9) is kept constant, and only RF voltage with max amplitude 500 V is accounted for both simulations. The simulation result of the unsegmented RF blades shows there is a non-zero potential along the axial direction which increases near the gap between the center DC electrode to the two adjacent electrodes (Fig. 2.10). As a consequence of the non-zero potential, long ion chain will have multiple ion-chain sections. We also observe this split experimentally. Conversely, for the segmented case, the potential along the axial direction is significantly lower, which is very useful to obtain a long ion chain (Fig. 2.10). As a result, we choose trap #2 even after the oven accident.

2.4.3 Trap #2

After investigating the simulations of the trap, we experimentally measured the secular frequencies of the trap. The data presented here was performed with trap #2 after the oven accident with $\omega_{\text{axial}}/2\pi \approx 400$ kHz on 2019-05-21⁹. Using a harmonic trap, we measure the trap frequencies at different ion positions using counter-propagating Raman beams¹⁰ to probe the motional modes of with ion chain size of two (Fig. 2.11). The Raman beams are aligned along the y -direction, and the two principal axes of the trap but not along the axial (x) direction of the trap.

⁹This is an example of trap frequencies measurement for future comparison. This trap has Yb coated on the blades, and the trap behavior might change with time.

¹⁰Raman operations will be explained in details in Chapter 4.

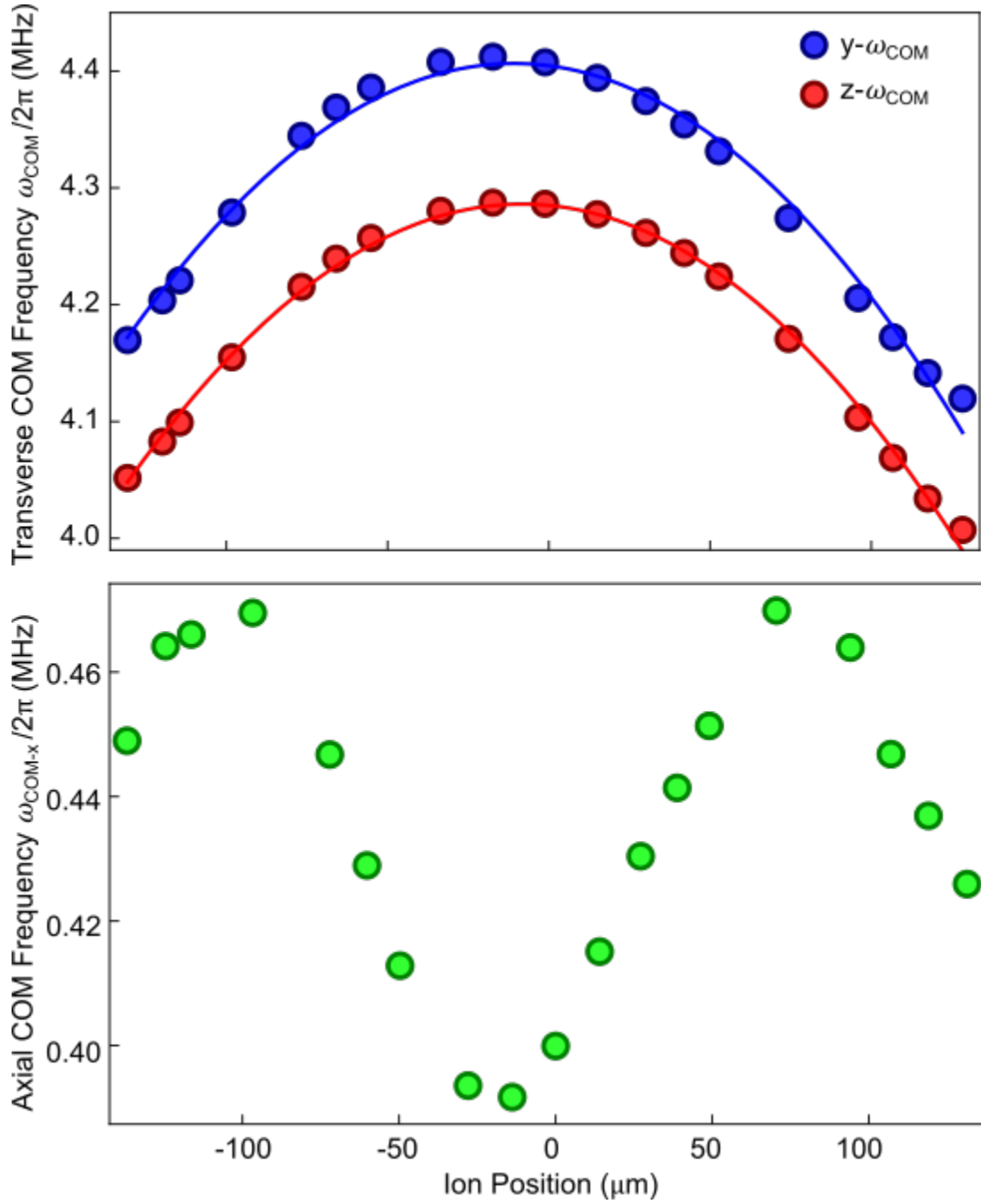


Figure 2.11: Trap frequencies were measured with two counter-propagating Raman beams to probe the motional modes of the ion chain. Color circles represent the data taken. Top: The two COM transverse frequencies of a single ion at different x -position. The solid color lines show the fit of data with $Ax^2 + Bx + C$. Bottom: The axial frequencies computed using $\sqrt{\omega_{\text{COM}}^2 - \omega_{\text{tilt}}^2}$.

The axial frequencies are computed by $\sqrt{\omega_{COM}^2 - \omega_{tilt}^2}$, where the tilt mode is the next motional mode after the COM mode. Although it is not shown in this thesis, ‘tickling’ is another method to measure the trap frequencies¹¹.

The ion chain is imaged into an ANDOR iXon Ultra 897 EMCCD camera first with a 0.43 NA Photon Gear objective and then with a 0.13 NA Thorlabs objective. Therefore, we need to understand the corresponding number of pixels in the camera to the real separation between the ions. The separation between the two ions $\Delta x_{2 \text{ ions}}$ in a harmonic trap [26] is given by:

$$\begin{aligned}\Delta x_{2 \text{ ions}} &= \frac{1}{2} l^{\frac{2}{3}} \\ l^3 &= \frac{Z^2 e^2}{4\pi\epsilon_0 M \nu_{\text{axial}}^2}\end{aligned}\tag{2.8}$$

where l is the length scale with Z as the degree of ionization of the ions, e as the electron charge, ϵ_0 as the permittivity of free space, and $\nu_{\text{axial}} = \omega_{\text{axial}}/(2\pi)$. We extract the $\Delta x_{2 \text{ ions}}$ by measuring ω_{axial} and obtain the number of pixels between each ion with the camera. Using this information, the calibrated conversion from the pixel to $\mu\text{m} \approx 0.161 \mu\text{m}/\text{pixel}$.

As the ion chain moves to the edge of the center static electrode, the COM transverse frequencies decrease, and the data trend is fitted to $Ax^2 + Bx + C$ (Fig. 2.11) as it is in a harmonic potential. The COM axial frequency also changes with distance and exhibits behavior similar to the unsegmented RF blades and static blades COMSOL simulation. Still, it differs from the COMSOL analysis of the segmented RF blades and static blades. The main difference between the simulation

¹¹‘Tickling’ the ion injects a small oscillating voltage into the trap through the static electrode. The motional frequencies of the ion will be excited when the ‘tickle’ frequency is resonant with one of these motional frequencies.

and the experiment setup is we apply non-zero constant voltages to all the static blades. As described earlier in this section, Trap #2 was also involved in the DAC malfunction which caused the Yb oven to release high Yb flux to this trap.

Chapter 3: Experimental System - Part II

One of the scaling challenges in a trapped-ion system is the rate of background gas collisions with the ion chain. Such collisions can disrupt the information of the qubit and cause the loss of the whole chain. Therefore, it is crucial to engineer an extreme high vacuum (XHV) environment to minimize the background gas pressure of the vacuum system. Another advantage of having an XHV environment is reducing the rate of ion re-ordering in the ion chain. This is especially useful for experiments with individual-ion addressing and/or mixed-species-trapped-ion system [27].

3.1 Introduction

The background gas pressure in a UHV system is due to degassing from the inner surfaces of the apparatus. In recent years, using titanium coating and heat treatment can achieve XHV in room-temperature vacuum system [28]. However, it remains a challenge to integrate a RF trap in such XHV room-temperature vacuum system as many components in the system may not be XHV compatible (i.e., electrical insulators such as Kapton). Therefore, housing the RF trap into a cryostat provides an alternative to achieve XHV. With a cryostat, the degassing from the components in the apparatus can be eliminated by cooling down the apparatus to cryogenic temperatures, where cryo-pumping turns the inner surface into getters

for trapping most of the residual background gas. The lowest pressure measured via cryo-pumping is $< 5 \times 10^{-17}$ Torr [29]. Besides that, the cryogenic environment reduces the average kinetic energy of the gas. The ion chain remains intact even when the background gas collides with it. Another advantage of using a cryogenic trapped-ion system is achieving a few order magnitude suppression of heating rates [30–32] due to surface patch potential and electric field compared to room-temperature setup. With these advantages, merging both RF trap and cryogenics is pursued and demonstrated [11, 33, 34].

3.2 The Cryostat

There are a few different kinds of cryostat in the market. One of them is a flow cryostat [35] which has low acoustic noise from the cryocooler but requires continuous replenishment of cold liquid coolant, which is expensive and time-consuming. Instead, the cryogenic trapped-ion system here [11] uses a close cycle Gifford-McMahon cryostat, which does not require constant refilling of the coolant. We choose this closed-cycle cryostat as it has a Vibration Isolation System (VIS) compared to other closed-cycle cryostats that suffer severe acoustics noise. The vibration from the cold finger is mechanically minimized from the main vacuum apparatus through an exchange gas region filled with helium gas¹. This region is kept 1 psi above the atmospheric pressure (Fig. 3.1 a). The only mechanical coupling between the cold head to the rest of the apparatus (which is mounted on an optical breadboard²) is

¹Hopefully, the cryostat technology will continue improving and an efficient and vibration-free solution will be achieved.

²The optical table is not floating to minimize the risk of having mechanical contact between the base of the VIS to the cold finger.

the VIS. In the VIS region, it is sealed with the rubber bellows³ that confines the helium gas. This helium gas serves as a thermal link between the cold finger and the sample mount where the RF trap is mounted on. With the VIS, the vibration of the system is minimized to < 70 nm rms amplitude (It will be discussed in section 3.8.).

The top of the cryostat (SHV-4XG-15-UHV from Janis Inc.) is a cold head (SRDK-415D2 from Sumitomo) that is powered by a F-70L Sumitomo helium compressor. This cold head features two stages with different cooling powers: the 40 K stage has 45 W, and the 4 K stage has 1.5 W. The RF trap and its resonator are mounted in the sample mount in the 4 K region. This region is shielded from the room-temperature black body radiation⁴ with two aluminum concentric cylindrical radiation shields at each of the 4 K and 40 K stages (Fig. 3.1 a). The estimated black body radiation heat loads are $\dot{Q}_{40K} \sim 5.5$ W and $\dot{Q}_{4K} \sim 550\mu$ W, which are lower than their respective stages cooling power. The thermal heat load due to most of the electrical wiring is negligible ($\sim 100\mu$ W). The four SMA cables connected to the RF electrical feedthrough, on the other hand, are not heat sunk, and the estimated heat load is ~ 500 mW at the 40 K stage and 220 mW at the 4 K stage. We observe a temperature increase of 0.4 K in the 4 K region when we raise the RF amplitude V_{RF} from $V_{RF} \approx 100$ V to $V_{RF} \approx 500$ V during ion loading, which takes about 3-4 minutes.

Furthermore, in designing the apparatus, it is essential to balance between

³We replaced the rubber bellow with a silicone bellow.

⁴The black body radiation heat load is estimated using Stefan-Boltzman law and the heat load for a given surface S is $\dot{Q}_{40K} = eS\sigma(T_1^4 - T_0^4)$, where $\sigma = 5.67 \times 10^{-8} \text{WK}^{-4}\text{m}^{-2}$, e is the emissivity (the ability of a surface to emit energy. $e = 1$ for ideal radiator).

the heat load and the optical access to send lasers to the RF trap with the given total cooling power of the cryostat. Therefore, the base of the cryostat is a spherical octagon to hold eight 1" diameter windows to provide optical access in the x, y -directions. The bottom of the cryostat features a 2.25" re-entrant window which allows a numerical aperture of 0.5 NA to image the ions along the z -direction. The cryostat is mounted on an elevated optical table to accommodate ion imaging optics from the bottom. The total heat loads from the recessed windows are estimated to be 2.4 W on the 40 K shield and 1.7 mW on the 4 K shield. This is below the heat load budget of the cryostat. Therefore, this cryostat can cool down the system to 4.5 K in about 5 hours with both the RF trap and helical resonator in it. We also have temperature probes (Lakeshore DT 670A1-CO) to monitor the temperatures on four locations: The resonator, RF trap, 4 K stage, and the 40 K stage. During the steady-state operation of the system, we have a heater to raise the temperature of the 4 K stage to 7 – 10 K to prevent helium gas from condensing around the cold finger⁵. As a result, the mechanical coupling of the cold head to the apparatus is reduced.

⁵A PID feedback loop can be set up to maintain the temperature above the helium condensation point. When the resonator temperature stabilizes, the RF-voltage V_{RF} to the trap stays constant. Therefore, the temperature PID feedback mechanism will be helpful as we lower down the V_{RF} during ion loading and then raise the V_{RF} after loading. During this process, the temperature of the 4 K region currently changes and takes about 5 minutes to equilibrate before further calibration and data taking. Without the feedback mechanism, it is crucial to wait for the temperature of system to settle down to minimize the drift of transverse frequencies with V_{RF} . In the current setup, we have a V_{RF} stabilization PID loop to compensate the drift. This will be explained in section 3.6.

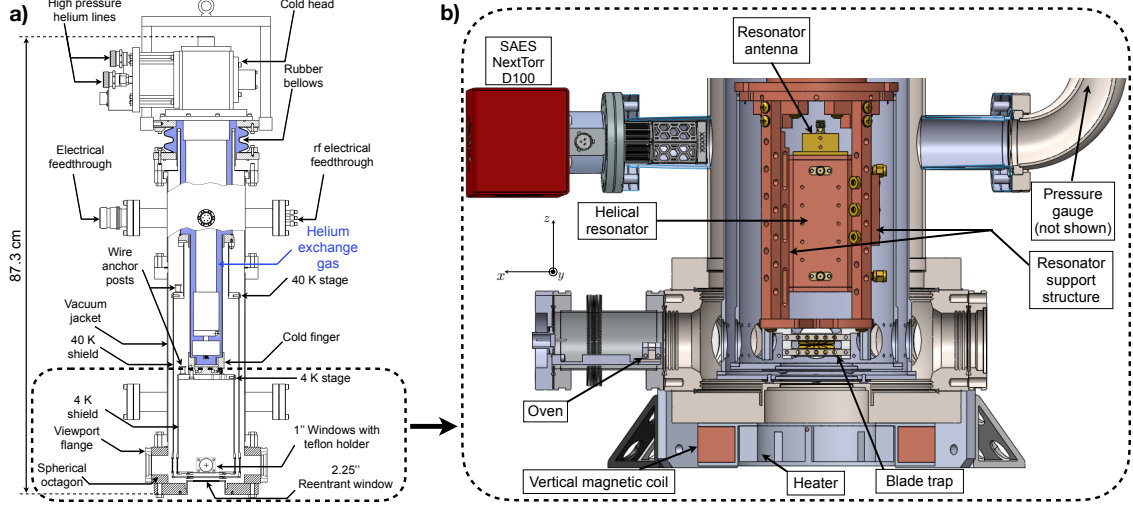


Figure 3.1: The cryostat that houses the RF trap. a) The side section view of the Gilford-McMahon cryostat. b) The magnified cross-section view of the lower part of the cryostat, which is rotated 90° with respect to a). A z -magnetic coil is mounted on the bottom of the re-entrant window flange. An aluminum fixture, with heaters in it, is mounted onto the inner diameter of the magnetic coil to the window flange to avoid water condensation on the surface of the window during the cool-down process. The heaters are kept active when the system is cooled down to < 10 K.

3.3 Cooling-down procedure

This apparatus is separated into two regions: The enclosure of the VIS and the UHV region (Fig. 3.1).

Enclosure of the VIS

Before activating the cold head, the VIS region (Fig. 3.2) is purged with 99.999% Ultra-High-Purity (UHP) helium gas. With the helium gas valve closed, a scroll pump evacuates this region until the bellow gets sucked in⁶. This VIS system is not UHV as it is sealed from the room environment with only screws going into a metal ring, the bellow, and the plate as shown as in Fig. 3.2. When the scroll pump

⁶We achieved 3.4×10^{-1} Torr in the VIS (the engineers at Janis/Lakeshore mentioned this is safe.) with the silicone bellow using the dry scroll pump of the TPS-compact Turbo Pumping System without activating the turbo pump. The baseline pressure with this scroll pump is 4×10^{-2} Torr with the valve to the VIS closed. However, the cryostat manual mentions to evacuate the shroud to $< 1 \times 10^{-4}$ Torr for a faster cooldown and lower final temperatures.

connection is closed, the bellow should stay sucked in for at least 15 minutes to check for any major leaks, otherwise the bellow would start to expand⁷. Then, the helium valve is opened to fill the VIS with helium. The safety valve here allows excess helium to escape, preventing the bellow from bursting. Following the helium-filled VIS, the helium valve is closed, and the scroll pump connection is opened to remove the gas in VIS and the helium gas. This procedure is repeated multiple times to purge the system with helium. Once the purging process is finished, close the scroll pump connection and regulate the VIS at 1 psi above the atmospheric pressure with helium to ensure that the helium is constantly occupying the VIS. This reduces the room's background gas (nitrogen gas, water vapour, oxygen etc.) from leaking into the VIS as the partial pressure of such gas is significantly lower in the VIS after purging. However, with the VIS seal, it is expected that the background gas to leak in, and these gases are frozen in the colder region. During warm up, specifically, ice in the VIS melts and deposits at the bottom of the VIS. Consequently, after many cycles of warming-up, a pool of water is deposited at the base of the VIS, increasing the mechanical coupling from the cold head to the apparatus⁸. The details will be

⁷This instruction is from Janis/Lakeshore's engineer in October 2020. However, after the replacing silicon bellow, we experience visible vibration on the ion occasionally. We attribute this to two factors. 1) The silicone bellow, which has a relatively larger diameter than the rubber bellow, touches the screws that hold the silicone bellow in place. When the silicone bellow is inflated, it changes the structural support, and mis-aligns the cold head, resulting mechanical coupling to transfer to the experiment region. This is fixed by re-aligning the cold head with the cold head off. If this is done while it is cool, the temperatures will shoot up. 2) Before the silicone bellow replacement, the initial rubber bellow was held by screws and also adhered to the top and bottom plates by epoxy. After the bellow was replaced, there is no epoxy used as instructed. We suspect the epoxy keeps the bellow in place relative to the flanges, preventing more air to enter the VIS. The current vibration could be due to icicles forming in the VIS, increasing the mechanical coupling. Till date (March 2021), we are corresponding with the engineer from Janis/Lakeshore for a solution.

⁸A sign of water build-up is the decrease of T2* coherence time of the qubit. T2* explanation is in the coherence section of this chapter (Section 3.9).

discussed in the Maintenance section (3.10).

The UHV region

Before the cooldown, the apparatus is pre-evacuated using a turbo-molecular pump (TPS-compact Turbo Pumping System) until the MKS-390511-0-YG-T (not shown in Fig. 3.1) gauge reaches about 2×10^{-5} Torr. This system also has a SAES NexTorrD-100 getter and ion pump (Fig. 3.1b) since hydrogen is the least efficiently cryo-pumped gas. The SAES NexTorrD-100 is activated during the cooldown.

The heater near the re-entrant windows needs to be switched on to prevent water condensation on the re-entrant window (Fig. 3.3)⁹. Once these steps are done, the compressor to power the cold head is activated, and the system is monitored. We monitor all the temperatures readings in the cryostat and the lab, the pressure from MKS, resonator, bellow condition, and helium supply to the VIS. The vector analyzer is connected to the trap to observe the trap resonance and Q factor. The valve from the turbo-molecular pump to the apparatus will stay opened until cryo-pumping works better than the turbo-molecular pump. Efficient cryo-pumping starts when the MKS pressure gauge is lower than the reading on the turbo-pump¹⁰. Further tests can be done by closing the valve of the system to the turbo-pump. At this moment, if cryo-pumping is working, the pressure reading from the turbo-pump will creep up, and the MKS pressure gauge will decrease. However, if cryo-pumping

⁹The temperature around the aluminum, which houses the heaters, is 36.5°C when the apparatus is cold. The real temperature around the re-entrant window is lower than 36.5°C as it is further away from the heaters.

¹⁰Based on my personal experience, this occurs when the pressure gauge is about an order magnitude lower than the pressure reading on the turbo and the temperature of the cryostat is about 100 K.

is not working well, open the valve of the system to the turbo-pump again and let the system settle down for the next try in closing the valve¹¹.

When the 4 K stage reaches 7-10 K, the 4 K stage heater can be switched on. The heater allows faster equilibration of the system to the working condition. When monitoring the trap resonance and Q factor is no longer required, the vector analyzer can be disconnected to send RF power into the trap. This can be done simultaneously with activating the 4 K stage heater, as sending RF power will raise the trap temperature. The base temperature of the cryostat of the 4 K region is $T_{4K} \approx 4.5$ K without these two temperature-raising factors.

3.4 Warm-up and cryostat-moving procedure

During the warm-up, the RF to the trap is disconnected. The turbo-molecular pump is attached to the cryostat. Once the MKS pressure gauge reading is higher than the turbo-pump, the valve is open. The 4 K stage heater can stay on throughout the warm-up with supervision. Permanent damage to the cold head may happen when the cold head exceeds room temperature. The high-pressure helium lines to the cold head can be detached once the apparatus is warmed-up to room temperature. All possible connections should be removed before moving the cryostat. The measurements on the micrometers of the imaging objective is recorded before the objective is lowered. The cryostat valve is closed, and the turbo-pump is detached. The top and bottom plates of the bellow are attached with four posts to constraint

¹¹Additional instructions in closing the valve to the cryostat while cooling down: If the pressure gauge spikes, open the cryostat valve and let the system to settle down before trying again. I would keep the turbo-pump running until the system has achieved a steady-state.

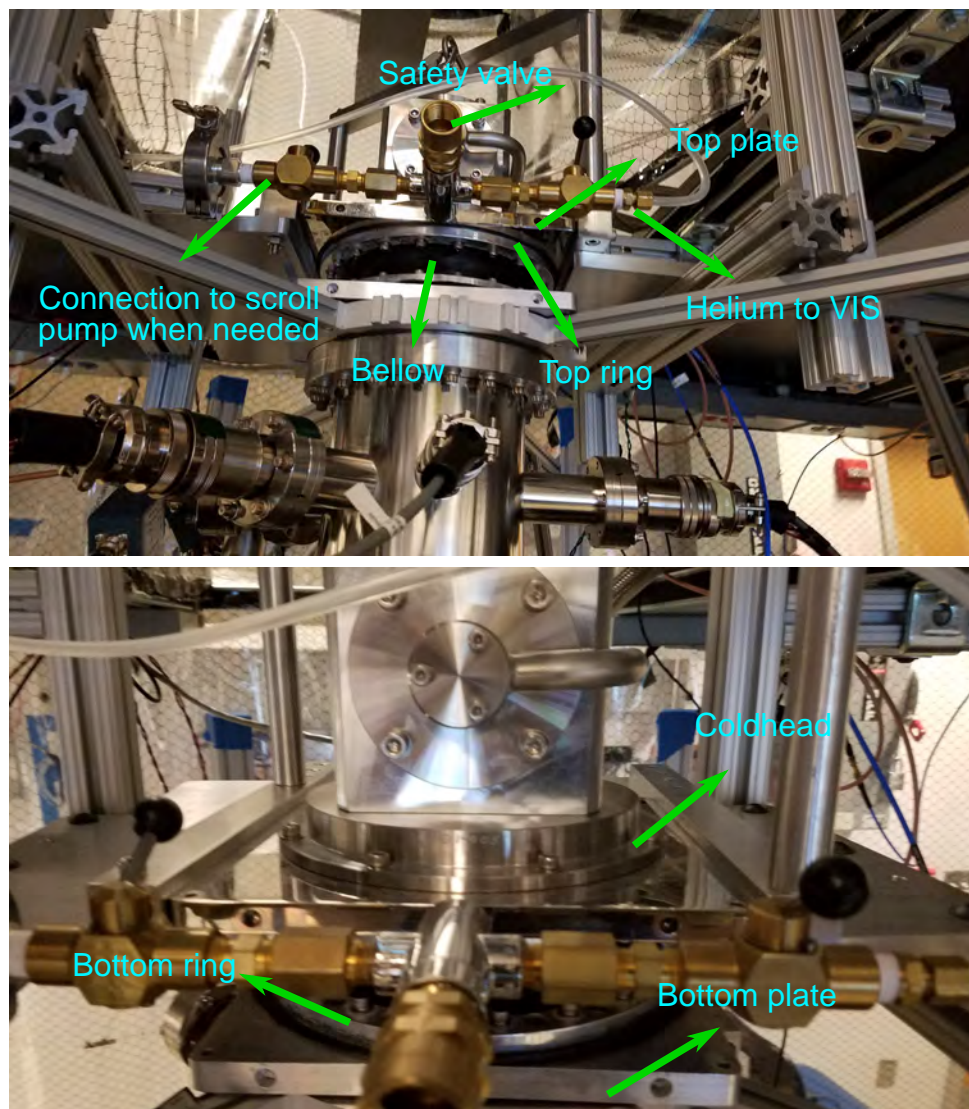


Figure 3.2: Helium gas to VIS. Top: The VIS needs to be filled with UHP helium gas. During the VIS gas evacuation process, a scroll pump is connected. Each side of the bellow is held in place with a metal ring and screws to the metal plates. Bottom: The top view of the VIS along the cold head. The screws labeled ‘cold head’ are removed for cold head servicing, separating the top of the cold head from the copper cold finger.

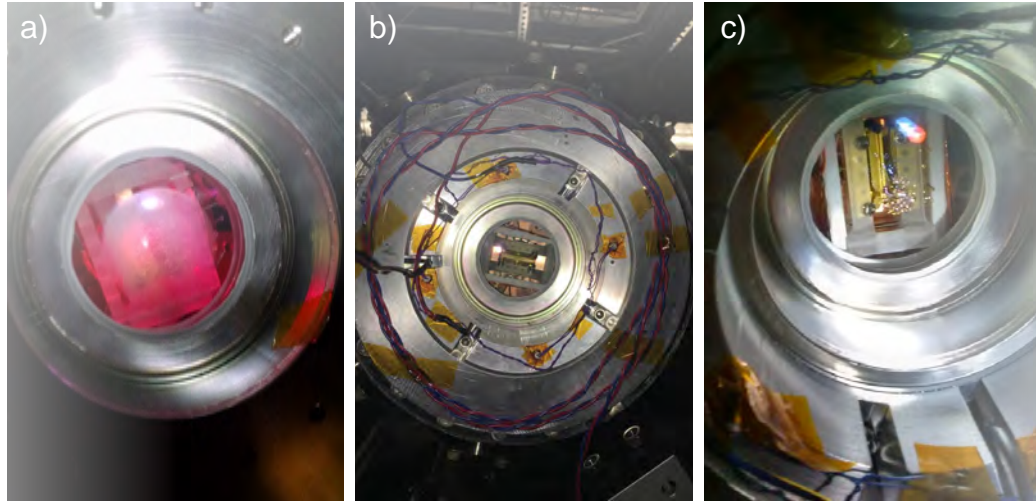


Figure 3.3: Water condensation on the re-entrant window (imaging window). a) The first observation of water condensation on the re-entrant window after cooled down with an imaging system below. The first imaging objective of the system is under this re-entrant window which causes the condensation to be as large as the diameter of the objective. b) Aluminum mount with cylindrical heaters attached to the vertical magnetic field coils for heating the re-entrant window to prevent condensation. c) The water condensation onto the re-entrant window during room humidity swing. We wiped the condensation and increased the heater temperature to account for humidity swings.

the relative movement of the cold head to the bottom part of the systems. Once the whole cryostat is securely chained to the I beam in the lab, we detach the top part of the external brackets that mount the cryostat onto the optics table. The cryostat is hoisted up slightly more than the optics on the table to provide clearance when sliding the cryostat out to the center of the lab. In this process, the imaging objective is covered with lens tissue, protecting the objective. Then, the cryostat is securely attached to a service station. The turbo-pump is again connected to the cryostat with the valve closed. Once the turbo-pump pressure is lower than the cryostat, the cryostat valve is opened.

3.5 Helical Resonator

A helical resonator impedance-matches the RF source to the trap by acting as a step-up transformer [36]. However, the parasitic capacitance and inductance of the 70 cm coaxial transmission cable, between the vacuum feedthrough to the RF trap in the cryogenic environment, make the impedance matching of the tuned resonator and the trap circuit difficult [37]. This limits the RF voltage delivered to the trap without heating the RF cables. In the current setup, we decide to house the helical resonator in the 4 K region of the cryostat to be as close as possible to the RF trap. This helical resonator is made up of a wound bifilar coil which one of its ends has two copper wires sticking out for the RF connections to the trap (Fig. 3.4). This setup also allows independent static potential offset, which is useful for micromotion compensation. The two coils are held in place by telfon holders¹² in

¹²The current resonator design can be further improved. In the past, we suffered electrical shorts between the blades of the trap. This problem was solved by inserting an aluminum plate to

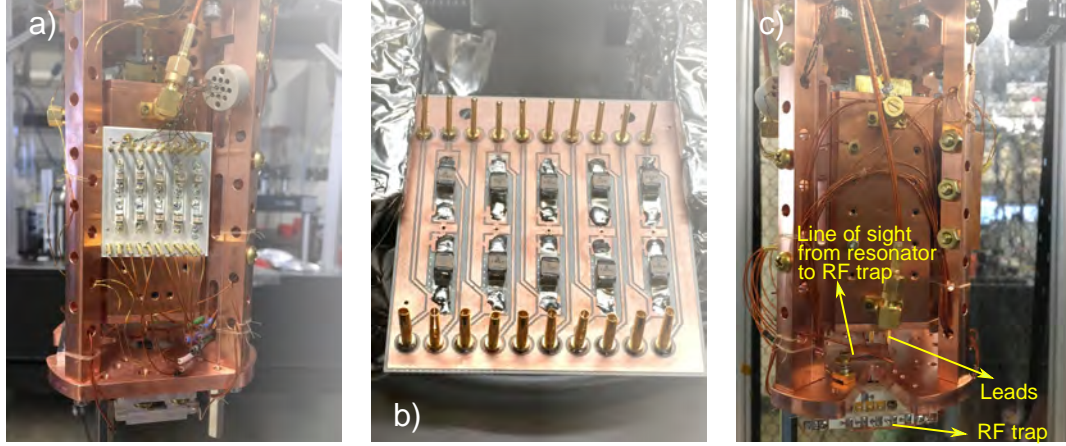


Figure 3.4: Electrical connections to the RF trap in the 4 K region. a) DC filter board mounted near the resonator to filter unwanted electrical signals to the static blades. b) The magnified view of the filter board before mounting to the resonator. c) 90° view from a). The yellow arrow points to the end of the resonator, which has two copper wires where the leads for the RF connections from the helical resonator to the trap. The house of the resonator is mounted on one of the pillars and supported with additional resonator supports as shown in Fig. 3.1 b). The inside of the resonator houses a bifilar coil, in which the two leads (yellow arrow) are connected to the RF blades of the trap.

the resonator house and shorted at RF with a 400nF capacitor. The resonator is made up of copper as it is a good heat conductor. The inner radius of the resonator is 2.3" and the bifilar coil is 1.5" radius with 0.19" pitch. A printed circuit board (PCB) with capacitive 100:1 pick off of the RF voltage is connected to the resonator for monitoring and stabilizing the transmitted RF voltage to the RF blades [38]. By loading the resonator with different test-capacitors, we measure the self-inductance $L_{res} = 2\mu\text{H}$ and self-capacitance $C_{res} = 8\text{pF}$. The performance of the resonator is tuned and then optimized by measuring the intrinsic (unloaded) resonator quality

block the line of sight between the trap to the resonator (Fig. 3.4 c). The current resonator design produces dust that landed on the gaps of the blades. We attribute the dust forming to two reasons. The first reason is the telfon holder is degrading due to the high voltage RF in the resonator. The dielectric dust generated landed on the gaps of the trap. Over time, the dust attracted metal which shorted the electrical connection. Another postulate was due to the multipactoring effect where the surface of the copper coils experiences an electron avalanche, generating copper dust which was shorting the blades with each other.

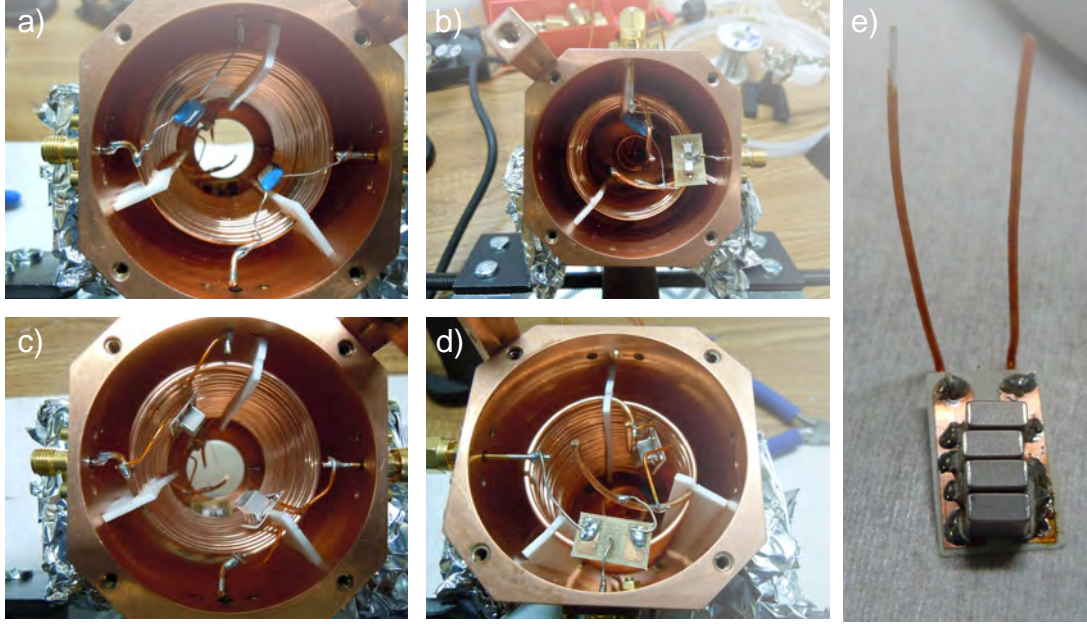


Figure 3.5: Resonator design. a) and b) The initial electrical connections of the bifilar coil at the bottom and end of the resonator respectively. a) The blue capacitor allows independent static potential offset from each RF blade. b) These two coils are shorted at RF with $1\mu\text{F}$ capacitor (blue capacitor). The PCB contains a 100 : 1 capacitive pick-off from the high voltage RF. c) and d) The current electrical connections of the bifilar coil at the bottom and end of the resonator respectively. The blue capacitors are replaced with an array of four 100nF capacitors (total of 400 nF), shown in e). e) An array of C5750C0G2J104J280KC 100nF capacitors from TDK Corporation on a PCB.

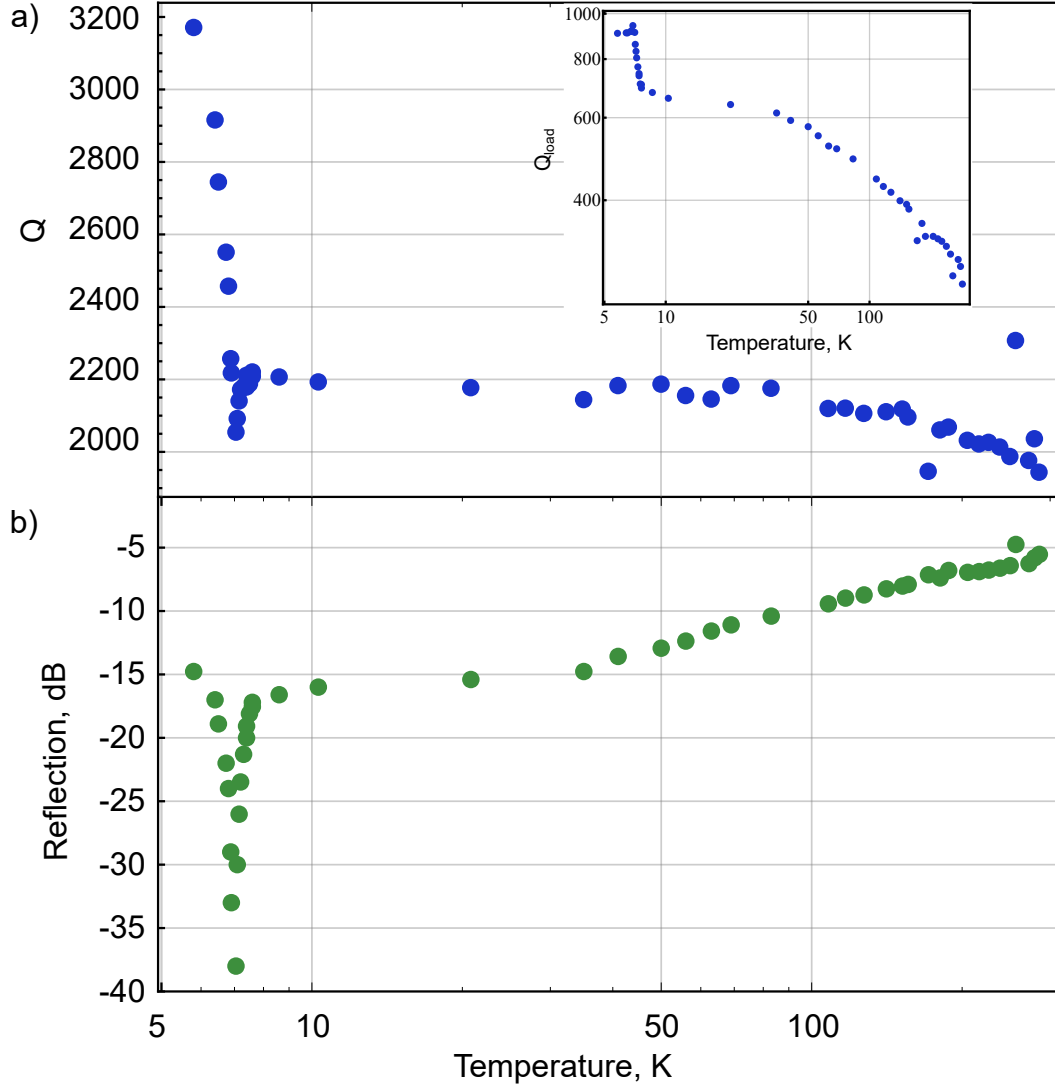


Figure 3.6: Resonator performance at different temperatures. The sharp variation at low temperatures is due to the decrease in the copper resistivity below 100 K. a) The Q factor of the resonator. As the cryostat cools down, the Q factor increases. The inset shows the loaded Q factor, $Q_{\text{load}} = \Omega_{RF}/\text{FWHM}$, where is measured with a vector analyzer. b) The reflected signal from the resonator is measured with the vector analyzer.

factor Q , where Q is defined as:

$$Q = 2 \frac{Q_{\text{load}}}{1 - \sqrt{R}} \quad (3.1)$$

where R is the reflected RF power due to impedance mismatch and loaded Q factor is $Q_{\text{load}} = \Omega_{\text{RF}}/\text{FWHM}$ accounting the full width at half maximum (FWHM) of the RF power at RF frequency Ω_{RF} . The resonator is inductively coupled with a small 0.5" diameter antenna-coil which its position is tuned to reach critical resonator coupling. This resonator design requires pre-tuning at room temperature before cooling because it does not have an external tuning degree of freedom when the chamber is sealed and cooled down¹³. Therefore, we purposely off-coupled the resonator at room temperature to reduce the intrinsic quality factor of the resonator $Q = 1050$. We reduce the mutual inductance between the antenna and the bifilar coil by pulling out the antenna holder. When the 4 K region of the system is in steady state, the Q value increases up to 3170 (Fig. 3.6) as the resistance of the whole RF circuit is reduced, changing the impedance matching conditions. In addition, the increase in Q factor is due to the decrease of copper resistivity [39] and skin depth at 4 K. However, we observe only 60% increase in the resonator Q . We attribute the other 40% to the oxide layers on the copper surface or the additional resistance contribution from the solder connections in the resonator. The whole cooldown takes 5 hours, and the resonator needs additional hours¹⁴ to settle down. The final drive

¹³In principle, adding a piezo to tune the resonator coupling externally will be helpful. The current method requires multiple iterations of cooling down the system to achieve the optimal configuration.

¹⁴We typically start the cooldown early and monitor the entire process. When the 4 K stage is about 5-10 K, the RF of the trap is connected to allow the resonator to settle down to the system operation temperature (7-8 K).

frequency Ω_{RF} increases typically by 0.6% after the cool down due to the reduction in the resonator self-inductance and self-capacitance at low temperature.

3.6 RF stabilization

With the capacitive 100:1 pick off of the RF voltage (Fig. 3.5), we use this pick-off voltage to actively stabilize the RF amplitude and the transverse frequencies of the trap¹⁵. This pick-off RF voltage from the cryostat is sent to a rectifier. The rectifier converts the RF signal to DC voltage signal where corresponds to the RF amplitude of the pick-off. The converted signal is then sent to a PID where its value is compared with a reference voltage set by an Arduino. The PID applies the feedback to a voltage variable attenuator (VVA)¹⁶ to correct the RF voltage applied to the trap. Finally, the PID is optimized.

Allan variance¹⁷ is obtained to understand the stability of the RF. One notable use of Allan variance is the measure of the stability for atomic clocks [40]. Here, we measure the Allan deviation of the difference between the reference signal and the input to the PID box, ϵ (Fig. 3.7). We compare the stability of ϵ with time before and after RF-stabilization. The Allan deviation is computed from the time series measurement:

$$\sigma^2(\tau) = \frac{1}{(2M-1)} \sum_{n=1}^{M-1} (y_{n+1} - y_n)^2 \quad (3.2)$$

with M as the number of sample/time bin and y_n as ϵ integrated over time τ . In both with and without PID feedback on ϵ , the Allan deviation decreases with increasing

¹⁵The dependence of the transverse frequencies is explained in Chapter 2.

¹⁶VVA is an active device that can inject noise to the system. A mixer, a passive device may perform better for this purpose.

¹⁷Allan variance is also useful to understand the slow drift in the experiment.

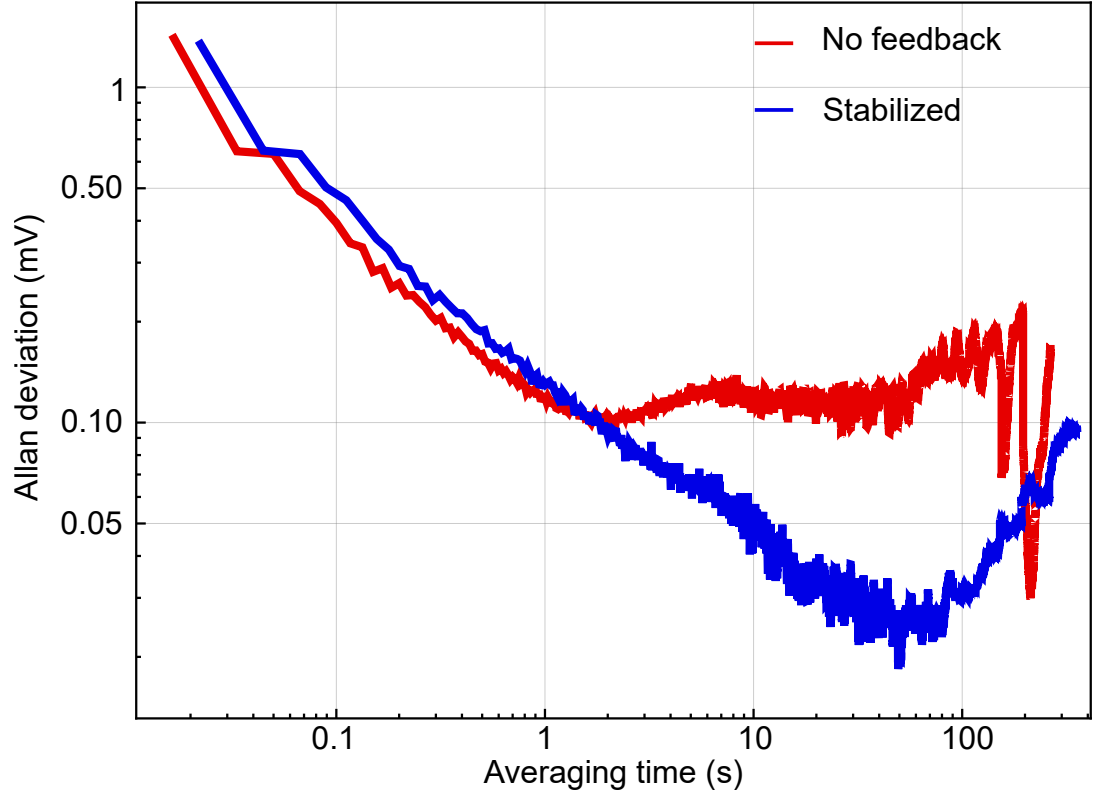


Figure 3.7: Allan deviation of the voltage difference between the reference signal and the input to the PID box ϵ at different averaging/integrating time τ . Both signals show a decrease in the Allan deviation till a certain τ , and eventually the Allan deviation increases again. The dip shows the time scale of the drift of this measured signal. Red (Blue) shows Allan deviation of ϵ without (with) the PID feedback.

integration time τ till system drift kicks in and the Allan deviation increases. The turning point of τ implies the time-scale of the drift. Without the feedback, the Allan deviation of ϵ drifts upwards at the integration time of $\tau = 2.3$ s. Once the RF is stabilized, it improves the stability for a longer time. The Allan deviation of the stabilized ϵ drifts upwards after $\tau = 50$ s. The priority of this lock is to stabilize the transverse frequencies of the trap. Therefore, a better measurement is the Allan deviation of the transverse frequencies (not shown here) with time, as demonstrated in Ref. [41]. It provides a direct measure of trap stability.

3.7 Characterization of cryogenic vacuum

In the ion trap experiments, low background pressure is demanding for primarily two reasons. First, the residual neutral molecular gas interacts with the ion chain with a $\sim r^{-4}$ potential, which increases the background gas collision rate with the ion chain. As a comparison to neutral-neutral collision rate, which is governed by Van-der-Waals, the potential is $\sim r^{-6}$. Secondly, the RF trap is a driven system where the collisions with the neutral gas can induce heating by displacing the ions diabatically with respect to the RF time scales, depending on the occurrence of the collision at an instantaneous RF phase [42–44]. As the result of the instantaneous and random amplification of the ion motion, the ion chain melts, and avalanche RF heating occurs. At this moment, the ions can be ejected out of the trap or left in highly excited orbits where laser cooling is inefficient.

Furthermore, the ion-chain lifetime depends strongly on the Mathieu parameter $q \sim 2\sqrt{2}\omega_{tr}/\Omega_{\text{RF}}$ of the trap, where the transverse frequencies are proportional

to the driving voltage amplitude $\omega_{tr} \propto V_{RF}$. The RF heating increases very rapidly with a power-law dependence on q with exponent greater than 4 as the exponent of 4 is due to Coulomb repulsion [45]. From classical scattering, the energy gained by an ion i at rest after an elastic collision with a background molecule that has an incoming energy E_m is given by:

$$\Delta E_i = \frac{4\xi}{(1+\xi)^2} \sin^2(\theta_{sc}/2) E_m \quad (3.3)$$

where $\xi = M_m/M_i$ is the mass-imbalance parameter of the molecule M_m and the ion and θ_{sc} is the scattering angle. In this calculation, we assume the residual background gas is mostly hydrogen molecules (H_2) as cryo-pumping H_2 in this apparatus works less efficiently after helium and $\xi = 0.011$ with $^{171}Yb^+$ ions. Therefore, by averaging over impact parameters, the mean increase of the ion energy per elastic collision is $\langle \Delta E_{Yb^+} \rangle \sim k_B \times 150mK$, with the assumption that the thermal energy of H_2 is $\langle \Delta E_{H_2} \rangle = 3/2 k_B \times 4.5K$. With this cryogenic apparatus, we can trap ion chains above 100 ions at $q = 0.35$ (Fig. 3.8 a). Conversely, in the room-temperature counterpart of this quantum simulation experiment¹⁸, the lifetime of a chain is on average 5 minutes for 50 ions [46]. The enhanced lifetime of ion chain in the cryogenic apparatus is due to the differential cryo-pumping to reduce the residual gas density compared to standard UHV system and the average energy transfer $\langle \Delta E_{Yb^+} \rangle$ due to the collision is about 60 times lower than in a room-temperature UHV experiment. We also notice that, based on the numerical simulations of the collision, the H_2 molecules $\langle \Delta E_{H_2} \rangle \sim k_b \times 10 K$ are not sufficient to displace the ions. Therefore, the

¹⁸Both setups trap the ion chain in a harmonic potential.

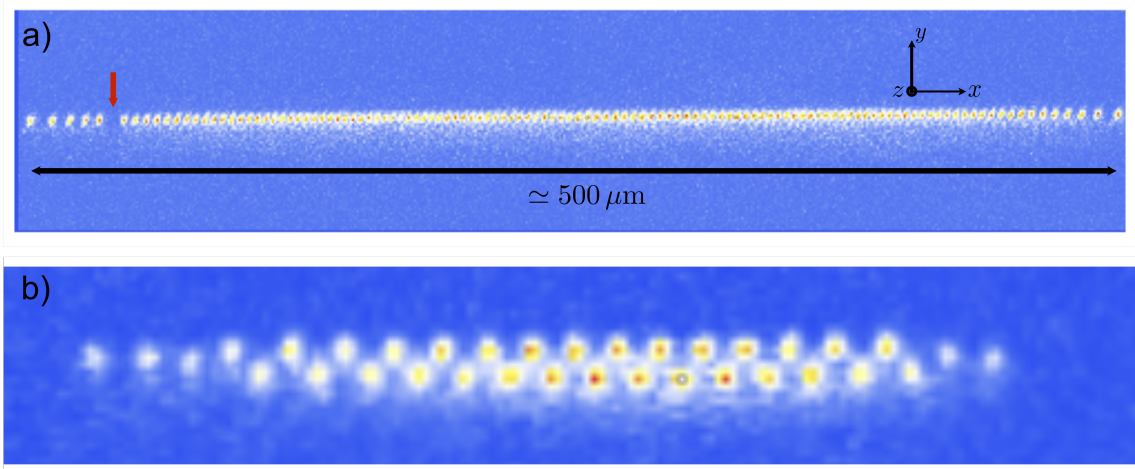


Figure 3.8: A chain of ions. a) A linear chain of 121 $^{171}\text{Yb}^+$ ions. The transverse trap ω_y or $\omega_z/2\pi = 1.5$ MHz with axial frequency $\omega_x/2\pi = 35$ kHz. The axial confinement is relaxed to fit all the ions in a linear configuration. The chain is imaged with a 0.13 NA objective. We took two images and combined them to fit the whole chain in an EMCCD camera. The red arrow indicates a gap, which can be a different Yb ion isotope or $^2F_{7/2}$ state of the $^{171}\text{Yb}^+$ that does not fluoresce. This dark ion remained in this position after more than 4 hours, indicating the chain never melted due to collisions with the background gas. b) A zigzag ion chain with $N = 35$ ions and trap frequencies $(\omega_x, \omega_y, \omega_z) = 2\pi \times (67, 613, 632)$ kHz.

catastrophic collision in the room temperature UHV is are most likely caused by collision with heavier residual background gases ($\text{N}_2, \text{CO}_2, \text{H}_2\text{O}$), which are frozen in the cryogenic system.

It is difficult to estimate the differential cryo-pumping between the room temperature region and the trap because the 40 K and 4 K cryogenic regions are not vacuum sealed. The MKS pressure gauge can only measure the pressure of the room temperature vacuum region, which is on the order of low 10^{-9} Torr when the apparatus is fully cooled down. Therefore, we use the zigzag ion crystal as a pressure gauge by measuring the collision rate between the background gas and the ion chain.

The interaction of ion-neutral molecule has potential $\sim r^{-4}$ due to the interaction between the charge e of the ion. The induced electric dipole moment of the

molecule with static polarizability α is given by:

$$U(r) = -\frac{\alpha}{2} \frac{e^2}{4\pi\epsilon r^4} = -\frac{C_4}{r^4} \quad (3.4)$$

Therefore, we can use the classical Langevin model [47] with no quantum correction as the average energy of the incoming H_2 molecules $\langle E_{\text{H}_2} \rangle$ is much larger than the p -wave centrifugal barrier¹⁹.

In the Langevin model, the collision rate γ is independent of the energy of the incoming particles. However, it is directly proportional to the density of the background gas, which is also proportional to the pressure P under ideal gas law:

$$\gamma = ne\sqrt{\frac{\alpha_{\text{H}_2}\pi}{\mu\epsilon_0}}, n = \frac{P}{k_b T} \quad (3.5)$$

We estimate the residual background pressure²⁰ inside the 4 K region by observing the elastic and inelastic collision events with a chain of zigzag ions (Fig. 3.8).

3.7.1 Inelastic collision

We observe the inelastic collision events by measuring the rate at which dark ions are produced. There are two possible inelastic processes with total probability P_{in} : a) Optically excited ions $^{171}\text{Yb}^+$ in the $^2P_{1/2}$ or $^2D_{3/2}$ states are subjected to such collisions which lead to population trapping in the metastable²¹ $^2F_{7/2}$ [49]. b)

An optically excited ion with enough energy undergoes molecule association to react

¹⁹This p -wave centrifugal height of this r^{-4} potential can be approximated as $E_4 = \hbar^2/2\mu R_4^2 \sim k_b \times 3\text{mK}$ with $R_4 = (2\mu C_4/\hbar^2)^{1/2}$ with the reduced mass μ [48].

²⁰The 4 K and 40 K stages are not vacuumed sealed for the placement of windows to allow optical access from outside. As a result, this compromises the vacuum quality. The line of sight from the ovens to the RF trap further exposing the trap to more background gas. A possible upgrade would be implementing ablation loading of the ions.

²¹Based on experience, the dark ion rate depends on 935 nm. 935 nm ensures that the state of the ion is pumped back to the cycling transition (Refer to Chapter 2.)

with H_2 chemically, forming ytterbium hydride (YbH^+) molecule [50]. Ions that undergo this process are called dark ions because they stop scattering Doppler cooling photons, and appear as a gap in the ion chain when it is imaged on an EMCCD camera. From the rate of dark ion occurrence, we extract a relative measurement of pressure $\gamma_{\text{in}} = P_{\text{in}}\gamma$. We also extend this study at a higher temperature and have observed that the dark ion occurrence rate increases by an order of magnitude. Finally, we compare the dark ion rate in the cryogenic system with the room temperature UHV system. The pressure gauge measurement in the UHV system is 1×10^{-11} Torr with $\gamma_{\text{in}}^{300\text{K}} = 2 \times 10^{-4} \text{s}^{-1}$ per ion (Fig. 3.9). Using these measurements from a UHV setup, the residual background pressure can be inferred as:

$$P_{4\text{K}} = P_{300\text{K}} \frac{\gamma_{\text{in}}^{4\text{K}}}{\gamma_{\text{in}}^{300\text{K}}} \frac{k_b T_{4\text{K}}}{k_b T_{300\text{K}}} \quad (3.6)$$

From this, we estimate the residual background pressure to be $P_{4\text{K}} < 10^{-13}$ Torr.

3.7.2 Elastic collision

Another measure of pressure with ions is observing the rate of reconfiguration events, γ_{el} due to elastic collisions of N ions in a zigzag configuration. This configuration is met when the two transverse frequencies are larger than the axial frequency, $\omega_{y,z}/\omega_x > N/\sqrt{\log N}$ [23]. There are two degenerate configurations, ‘zig’ or ‘zag’, which are separated by a small energy gap that depends on the splitting of the transverse modes $\Delta\omega = \omega_z - \omega_y$. When an elastic collision exceeds the energy $> \Delta\omega$, the ions have a finite probability p_{flip} to flip from ‘zig’ to ‘zag’ configuration and vice versa. For this measurement, we recorded the zigzag ion chain and the occurrence of such change in configuration $\gamma_{\text{el}} = p_{\text{flip}}\gamma$. We measured the elastic rate

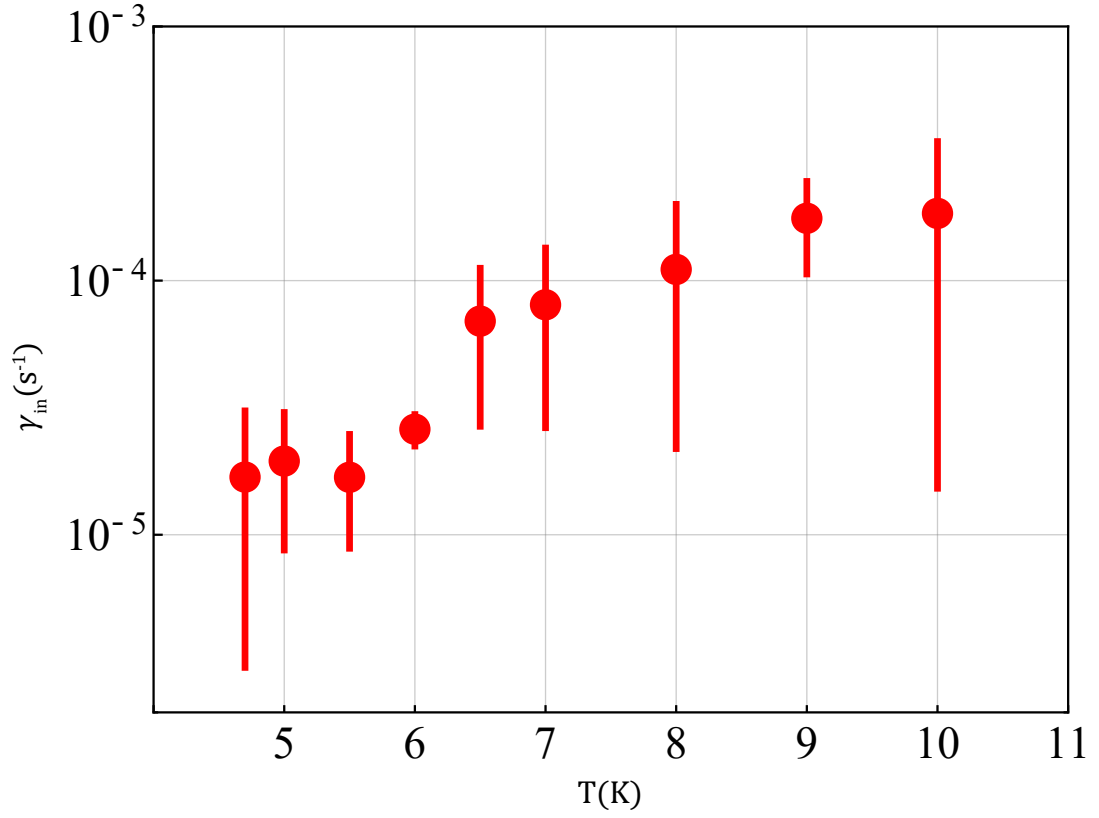


Figure 3.9: Inelastic collision measurements per ion γ_{in} at different temperatures with 33 ions for a time period varying from 3-12 hours. The inelastic rate is estimated from averaging the time intervals between dark events. The error bars show the time interval standard deviation of each data set. The huge error bars reflect the rare occurrence of the inelastic collision process during data taking.

at two different temperatures at 4.7 K and 7 K at the same transverse frequency splitting $\Delta\omega = 2\pi \times 2\text{kHz}$. However, to find the pressure from Eq. 3.5, we need to calculate p_{flip} which is a function of transverse mode splitting $\Delta\omega$ and the energy of the incoming particle. We performed a numerical simulation of a zigzag ion chain of 31 ions after a collision with H_2 molecule which has mean energy $\langle E_{\text{H}_2} \rangle = 3/2k_bT$ over 2×10^4 RF periods to calculate p_{flip} ²². From the measured γ_{el} and the calculated p_{flip} , the estimated pressure at the trap region is $P_{4\text{K}} = (1 \pm 1) \times 10^{-12}$ Torr and $P_{7\text{K}} = (2 \pm 1) \times 10^{-12}$ Torr (Fig. 3.10).

3.7.3 Other Methods

In addition to the methods shown above, the pressure of the system can be measured through the hopping rate of a single ion between one of the two wells in a double-well potential [51]. With static electrodes control on the potential, the potential barrier is adjusted such that the two minima of the well is much lower than the average energy transfer due to a collision event. Another method to estimate pressure is measuring the rate of re-ordering events in a linear ion chain [51]. Two different ion isotopes can be used in this measurement since the mass difference between two species is close. The isotope shift of the different isotopes makes observing the re-ordering event clearer because the laser applied will only be resonant to one of the isotopes.

²²The details of the calculation are in Ref. [11]. The probability p_{flip} was estimated by randomly sampling 10^5 initial conditions repeated 5 times to estimate the error.

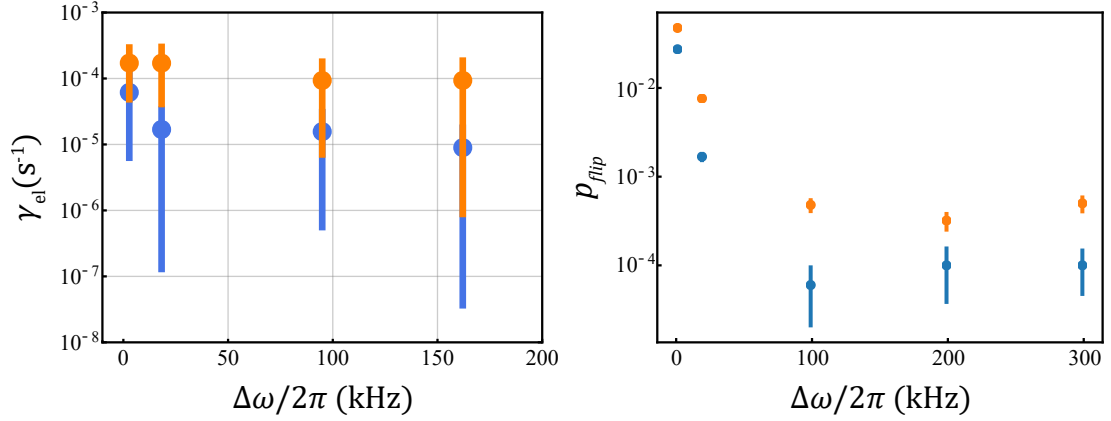


Figure 3.10: Elastic collision γ_{el} per ion as a function of the energy barrier $\Delta\omega$ between ‘zig’ and ‘zag’ configurations at different temperatures. The blue (orange) dots refer to $T = 4.5$ K ($T = 7$ K). a) The measured data with the number of ions varying from $N = 31$ to $N = 38$ for a time period varying up to 12 hours. The huge error bar describes the time interval standard deviation, which reflects the low occurrence of the event. b) Numerical results for p_{flip} with varying $\Delta\omega$. The error bars are estimated from the statistics of running the simulations 5 times.

3.8 Characterization of the vibration in the system

The spin-spin interactions of the quantum simulation are generated [52] through a stimulated two-photon Raman process with a 355 nm pulsed laser. This makes any ion chain displacement of the order of the Raman laser wavelength during the interaction time would cause an unwanted phase shift on the ions. Therefore, it is crucial to understand and minimize the vibration in this Gifford-McMahon closed-cycle cryostat. The vibration from the cold head with the whole apparatus’s mechanical stability is measured with interferometric setups (Fig. 3.11). The RF trap is removed from the 4 K stage to place three mirrors on the trap mount, along the Raman direction (y), the axial direction of the trap (x) and the vertical imaging direction (z). This setup tracks the trap movement with respect to the breadboard

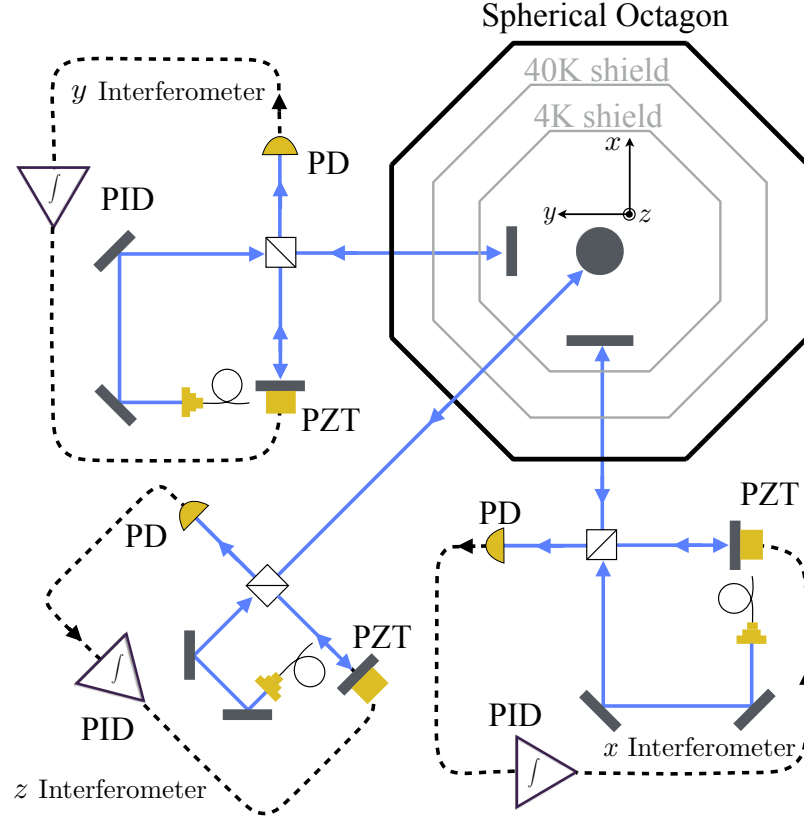


Figure 3.11: Michelson interferometers for vibration measurement along x, y, z directions of the apparatus. Three different laser lights from the fibers are sent to their respective interferometers which each of them has a piezo-mounted mirror (PZT). The PID locks the photodiode signal to a fringe with a feedback loop. The output voltage from the PID to the piezo compensates vibration and measure the amplitude and frequency of the vibrations.

and the table up to a few nanometers. In each Michelson interferometers, piezo-mounted mirrors are used to lock the interferometer to a fringe, keeping track the displacement of the trap (Fig. 3.11). The whole servo loop has 1.8 kHz bandwidth which we can compensate acoustic noise up to 300 Hz²³. Each piezo-mounted mirror is individually calibrated for its voltage-to-distance conversion. The output voltages to the piezos are the direct measurement of the displacement of the trap mount on

²³This limited frequency range is unable to capture higher frequencies that correspond to the $T2^*$ of the system (1-2 ms).

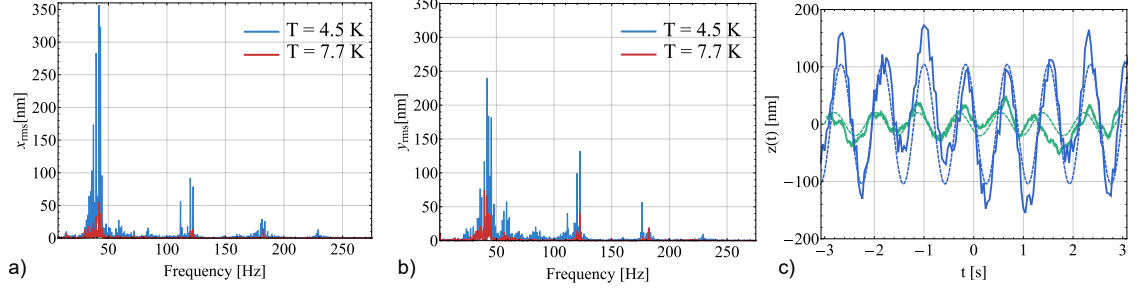


Figure 3.12: Vibrations along the three principal axes of the trap. a) and b) describe the in plane $x-y$ vibrations for the trap mount temperatures $T = 4.5$ K and $T = 7.7$ K. After raising the temperature of the 4 K region above the helium boiling point, the rms amplitudes along $x(y)$ are reduced by a factor of 5(6). The resolution bandwidth (RBW) is 0.1 Hz. c) z -direction vibration of the cryostat (solid lines) along with its fitted line of a sine with frequency 1.2 Hz (dashed lines). The blue (green) lines indicate the vibration before (after), improving the static support of the breadboard.

each axis.

In this measurement, the main contribution of vibration along the $x-y$ plane is 40 Hz, which is due to the normal mode of the cryostat 60 cm long level arm²⁴. We observe that these vibrations are worsened at helium condensation temperature, where the condensed helium increases the mechanical coupling of the vibrating cold head to the trap region. This vibration effect can be reduced by heating the 4 K stage and operating above the helium boiling point. As a result of increasing the 4 K stage to $T = 7.7$ K, the rms displacements along the $x-y$ plane are reduced (Fig. 3.12). The higher frequency modes (> 100 Hz) are on the same time scale as the quantum simulation experiments. Therefore, they should be further minimized. According to finite element analysis, the vibration modes at 120 and 282 Hz peaks are attributed to the mechanical structure inside the 4 K shield, which houses both

²⁴We also compare this value with another group that uses this cryostat. Both of us observe similar vibration at 40 Hz.

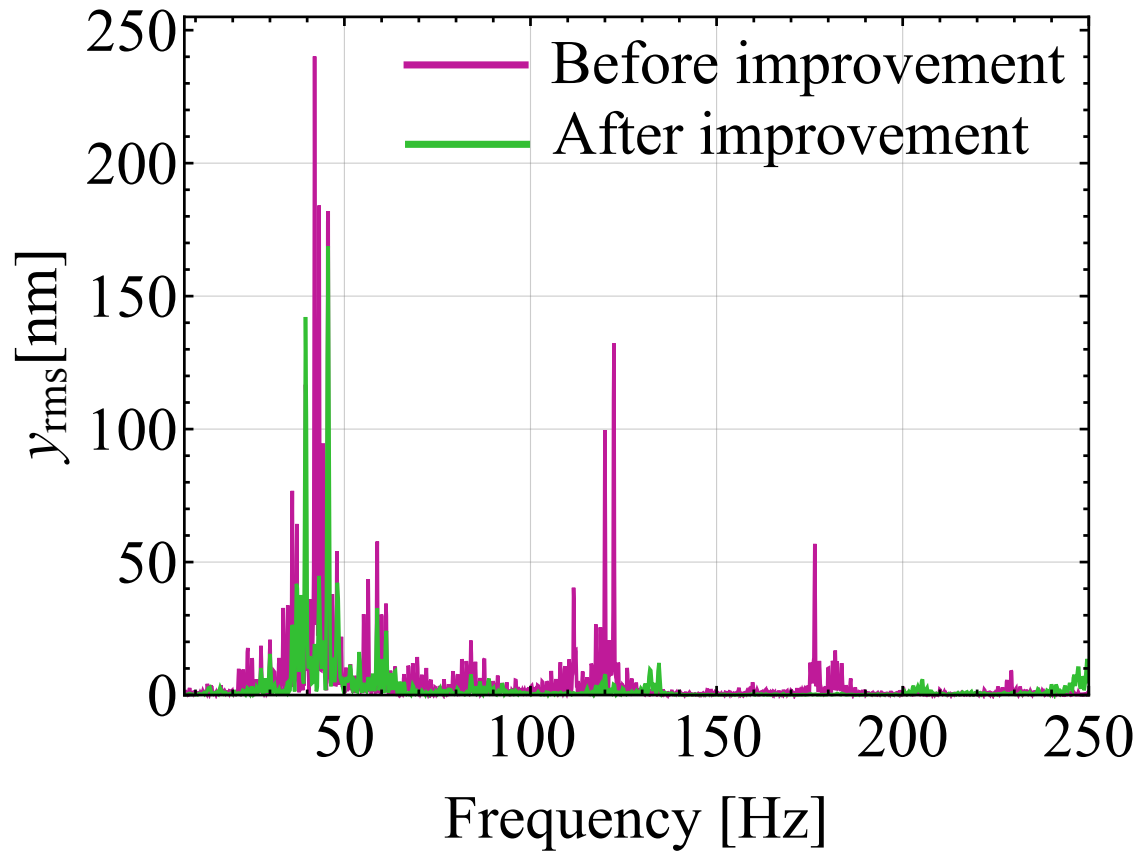


Figure 3.13: Vibration improvement after adding mechanical support on the resonator. After adding the mechanical support, the higher frequency peaks ($> 100\text{Hz}$) are suppressed and moved to higher frequencies.

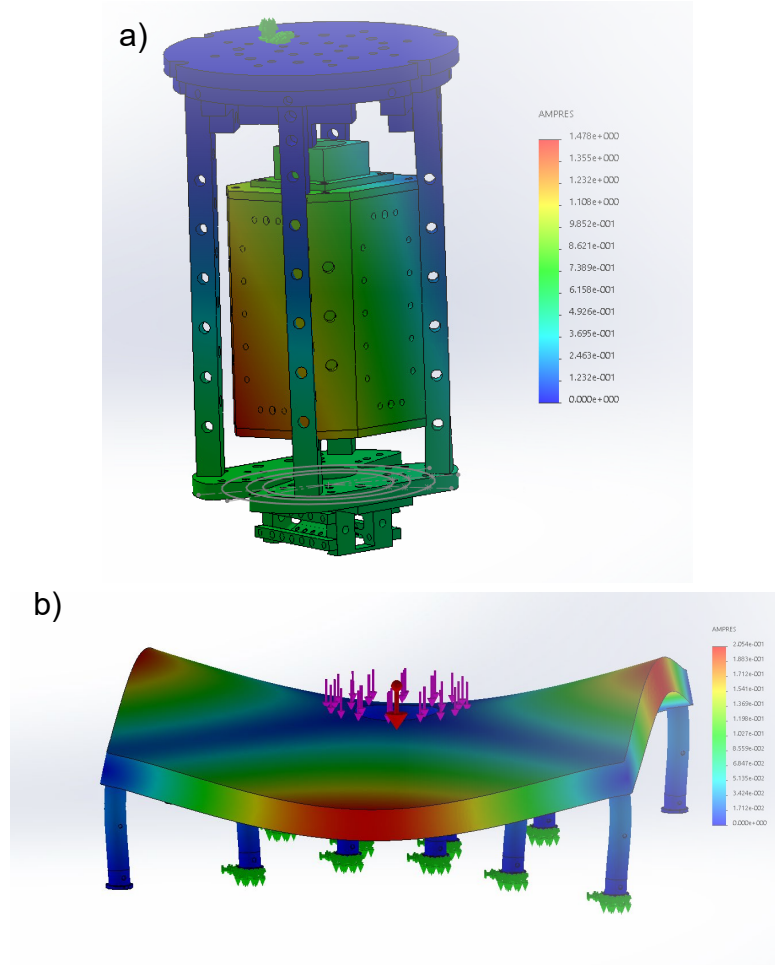


Figure 3.14: Finite element analysis of the mechanical structure of the system. a) The resonator is attached to one of the pillars without any additional support, as shown in Fig. 3.1. This frequency mode is 136 Hz. This simulation pin-points that the > 100 Hz can be improved by reinforcing the resonator. b) The breadboard that supports the apparatus. This breadboard is mounted onto the optics table with posts. The pink arrow assumes the weight of the cryostat. This frequency mode is 379.03 Hz.

the resonator and the trap. To reduce these modes, we strengthen the resonator support (Fig. 3.1b), and successfully suppress the higher frequency modes by more than an order of magnitude (Fig. 3.13).

Once all the vibration measurements have been taken, the mirrors are all removed and the RF trap is mounted back to the system. With the trap in the 4 K region, we also design and mount a mirror with its holder near the trap facing the Raman(y) direction. With this mirror, a Michelson interferometer can be set up to keep track of the unwanted phase shift. Subsequently, the tracked phase shift is feed-forward to the AOM phase or an EOM in the Raman path²⁵. Alternatively, we can implement a phase insensitive Raman scheme to drive the spin-spin interactions where the phase-noise on the spin due to the vibration is transferred to the motional phase [53]. Currently, we are investigating this phase insensitive scheme on the ions.

In addition to vibration measurements, the mechanical structures are analyzed using finite element analysis with Solidworks. From here, we understand the possible improvements can be made to the mechanical structure (Fig. 3.14). For example, the number of posts and their placements under the breadboard with the weight of the cryostat are studied to minimize the vibration amplitude of the structure.

3.9 Coherence lifetime of the system

This apparatus has vibrations (as described in the earlier section). We are interested in understanding the consequence of such vibrations in the experiment, especially for Raman operations with 355 nm pulsed lasers. We perform a Ramsey

²⁵The mirror is in the system now, but the interferometer is not set up yet.

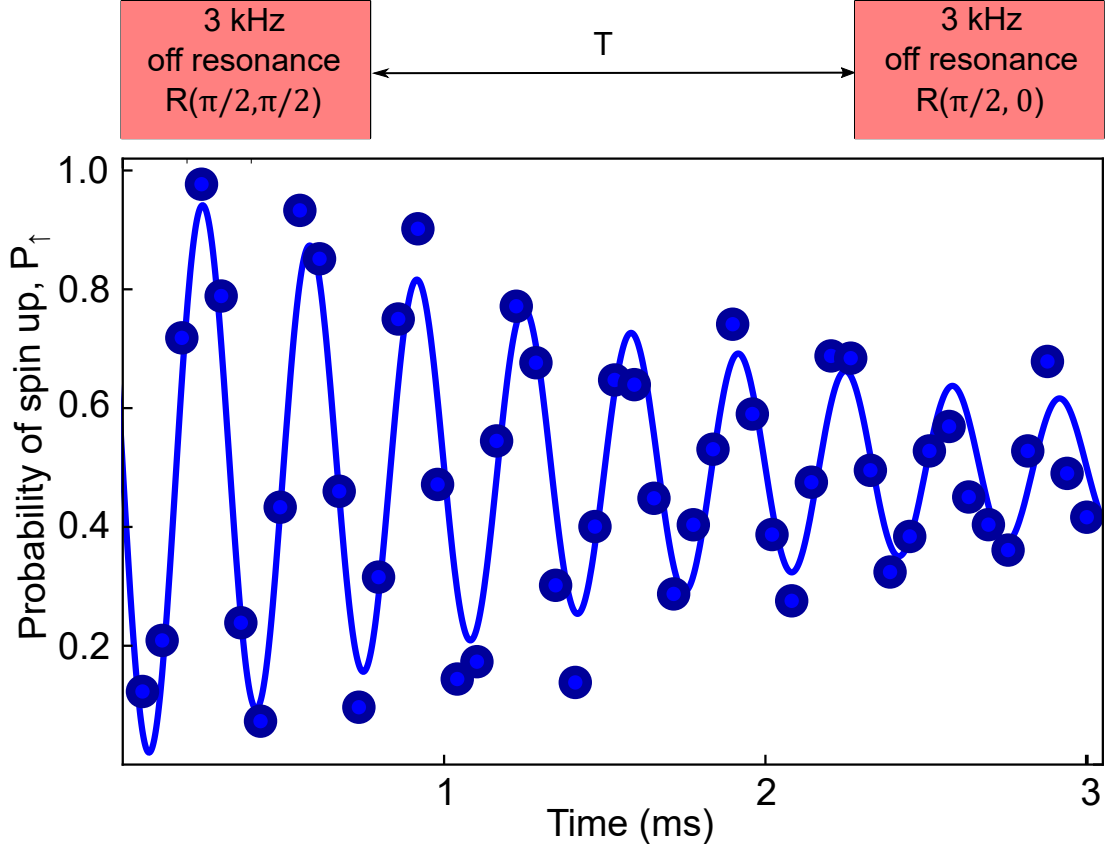


Figure 3.15: Raman coherence with Ramsey. Top describes the experimental sequence. Single qubit θ rotation $R(\theta, \phi)$ along an axis determined by ϕ . Bottom shows the result of such experimental sequence.

experiment to measure the coherence of the qubit along the $x - y$ plane of the Bloch sphere (also known as T_2^* of the qubit.). We first initialize the qubit to $|\downarrow_z\rangle$ and use Raman operations (Fig. 3.15) to perform a Ramsey test with two $\pi/2$, and the time between these two pulses is varied. The Raman $\pi/2$ pulses are 3 kHz off-resonant from the qubit splitting, where the on-resonant Rabi frequency is $\approx 350\text{kHz}$. With this sequence, we would expect the Ramsey has 3 kHz fringes. In an ideal condition, the contrast will stay coherent > 20 ms for this hyperfine qubit [4,5]. However, due to the decoherence, we observe a decay of about 2 ms (Fig. 3.15).

We also compare the result with a Ramsey experiment using microwave ro-

tation operations. Here, we observe a coherence of at least 20 ms. Therefore, we attribute this de-coherence from the laser due to the vibration since it imprints phase noise to the 355 nm laser. In addition, we observe improvement in Raman coherence time up to 2 ms after inserting the resonator supports, heating the 4 K stage, servicing the cold head, and cleaning the VIS. Each of these changes improves the performance of the cryostat, reducing the vibration²⁶.

3.10 Maintenance

3.10.1 VIS Maintenance

As alluded by the earlier section of this chapter, the base of the VIS region will accumulate water. During each warm-up, ice forming around the VIS will melt, resulting in a pool of water forming at the base of the VIS²⁷. The instrument is hoisted from the experimental breadboard and moved to the center of the lab. Instead of mounting the apparatus onto the service station, it is lowered and mounted to a breadboard on the floor. All the windows are covered with aluminum foils and lens tissues to protect the windows from dust. The vacuum part of the system is then connected to the turbo-pump, to maintain UHV pressure for the room-temperature region of the system. The screws securing the bellows to the bottom flange are loosened (this is separated from the vacuum region), and the top part of the apparatus (Fig. 3.16 b-c), including the cold head, is mounted onto the service station. Due to water accumulation in VIS, rust is formed in VIS and the copper cold finger is

²⁶We did not re-measured the vibration of the system after these changes individually. Instead, we observe the Raman Ramsey coherence.

²⁷This apparatus has been constantly operating since 2016. The first VIS maintenance was done in September 2020.

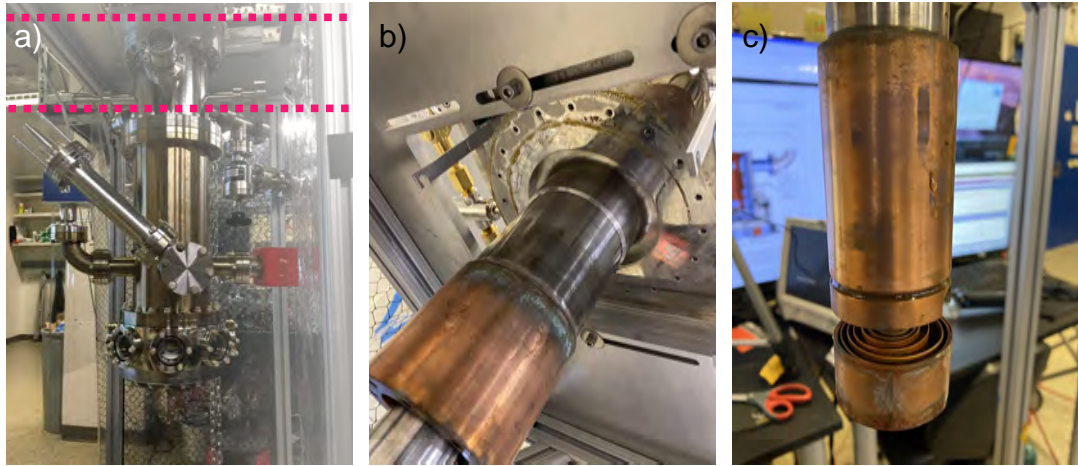


Figure 3.16: VIS maintenance. The apparatus is hoisted to the center of the lab for maintenance. a) The instrument is supported by the service station at the center of the lab. The flange connections (indicated by the pink lines) should not be opened if only VIS maintenance is done. These connections hold the apparatus under vacuum. The black valve (right side of a)) allows connection for the turbo-pump to keep the experimental part of the apparatus under vacuum. The 45° angled positioned flange and the cylinder provided a connection to a Residual Gas Analyzers (RGA), but now both the flanges and cylinder are removed in the current setup. During the VIS maintenance, the apparatus is lower down and mounted to a breadboard on the floor. On the other hand, the lower pink line connection is opened after venting this vacuum region for the apparatus maintenance. Removing the flanges of the upper pink line is complicated as the wirings to the experimental chamber need to be cut if the flange is detached. b) The bellow is removed for replacement, revealing the top plate, as shown in Fig. 3.2. c) Once the bellow is detached from both the top and bottom plates, the top part of the cryostat is raised along with its cold head and mounted to a service center, revealing the copper cold finger.

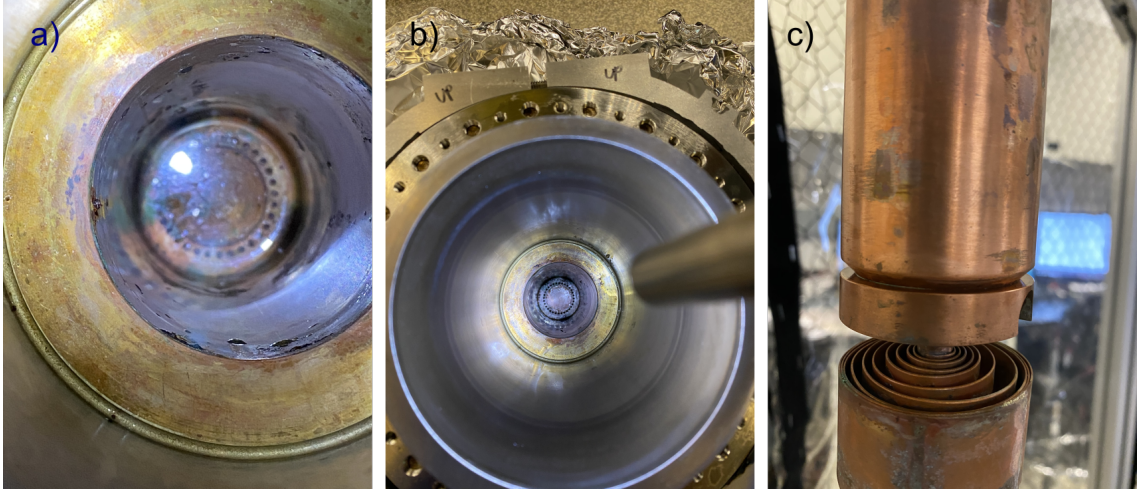


Figure 3.17: Water in VIS. a) The rusty base of VIS where a pool of water is formed. b) The VIS is cleaned, and the water is removed. The holes outside of the VIS allow connection to the bellow. The outer collar (with writings ‘up’) is custom made to have external rods attached, connecting to the lead-filled 80-20 pillars mounted on the optics table. c) The discolored copper on cold finger due to water. The end of the cold finger is made up of a coil of copper, and it is springy (not depicted in Fig. 3.1).

discolored (Fig. 3.17). The pool of water and rust are cleaned. Before sealing this VIS, we clean the surface of VIS with isopropyl alcohol and ensemble the bellow part. Once it is completed, the top part of the cryostat is then lowered to attach to the main chamber.

3.10.2 Cold head Maintenance

On July 2020, the trap exhibited 80 minutes oscillation²⁸ with peak to peak displacement $\sim 40\mu\text{m}$ on the $x - y$ plane (Fig. 3.18 - 3.19). The Rabi frequency of the ion with Raman lasers also fluctuated with this similar 80 minutes oscillation. This ruled out the drift of the imaging system and the lab temperature remained stable. We moved the objective of the imaging system to focus the blade. In this way,

²⁸This oscillation interval occurred in another research group, according to the engineer from Janis/Lake Shore.

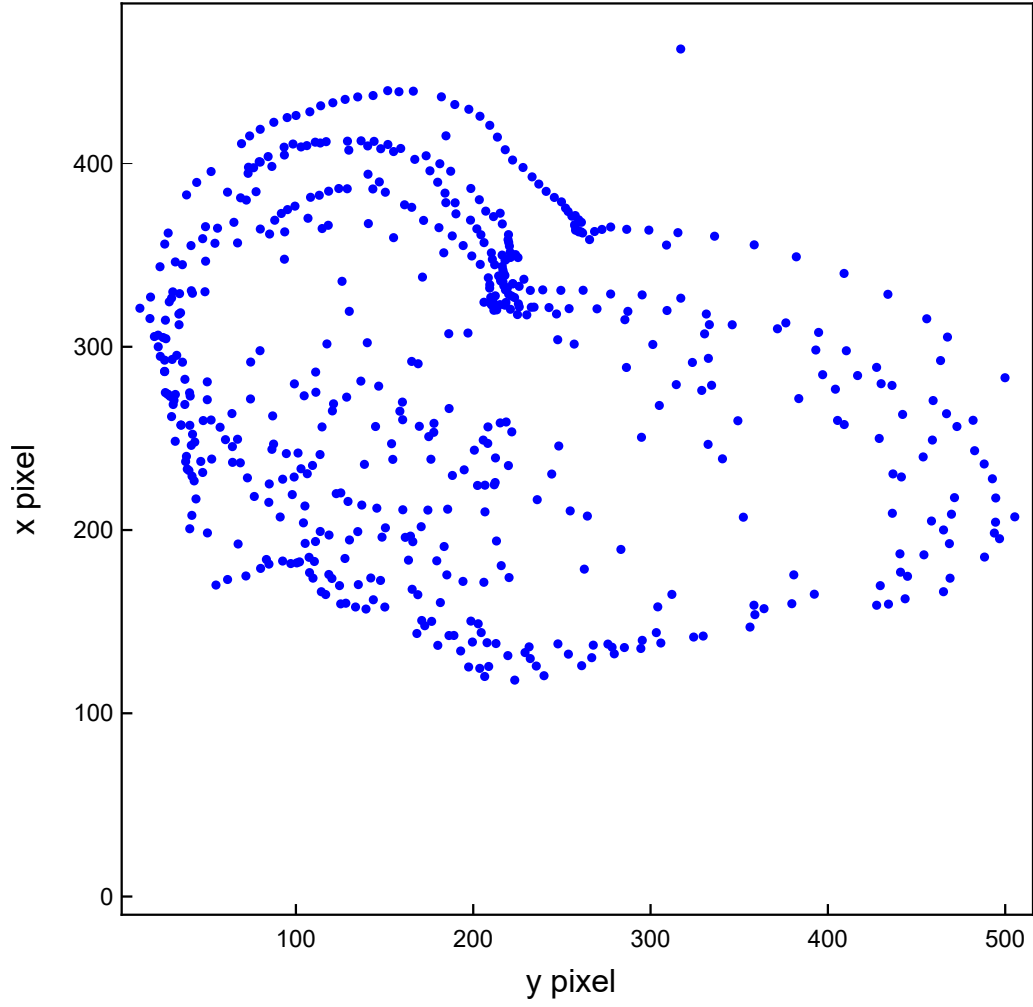


Figure 3.18: 4.6 hours drift measurement of a single ion, taken by the imaging camera. Each pixel is $0.161\mu\text{m}$. We called this the “broken heart” or “cursed heart”.

we observed the trap was moving with this 80 minutes oscillation too. Therefore, we concluded that the whole trap was experiencing slow drift. At the same time, the temperature probes at the 4 K and 40 K stages also experienced an 80 minutes temperature drift. As the solution, the cold head was replaced with a refurbished cold head from Sumitomo (Fig. 3.20) and the adsorber in the F-70L Sumitomo

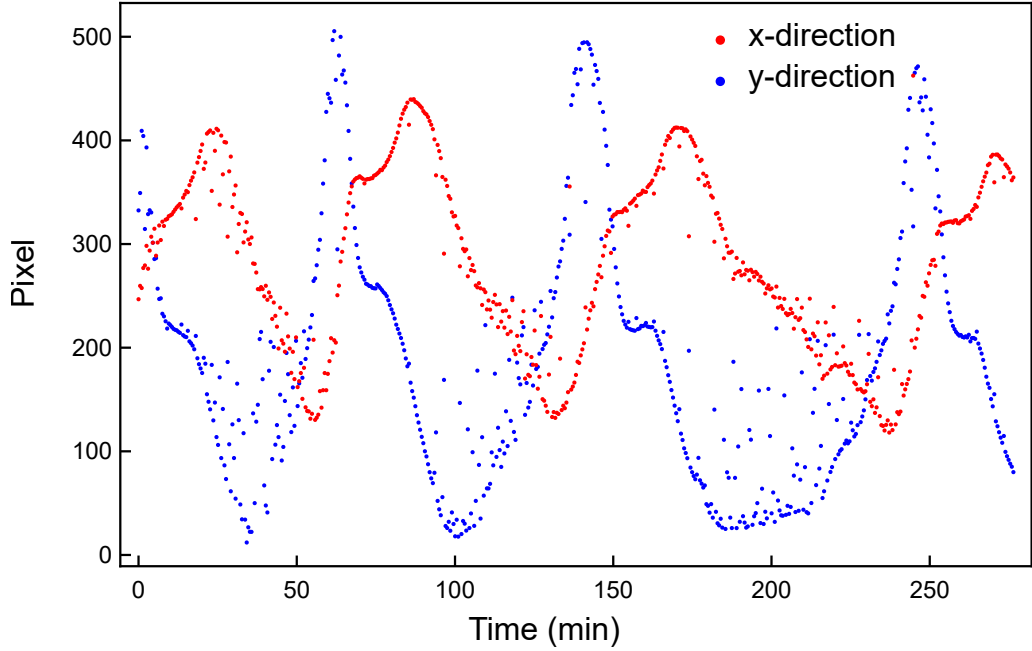


Figure 3.19: The x and y ion displacements with time. Throughout the 4.6 hours of measurement, we observe an oscillation with 80 minutes interval. The scaling from pixel to distance is $0.161\mu\text{m}/\text{pixel}$.

helium compressor²⁹. After the cold head servicing and VIS cleaning, we do not observe the 80 minutes interval drift.

3.10.3 Filter water and chiller

The F-70L Sumitomo compressor supplies high-pressure helium gas to the cold head³⁰(Fig. 3.21). It requires a continuous flow of cooling water³¹. For this purpose, we use a chiller (Tek-Temp NRD550/S1/R2K). This chiller regulates the temperature of the coolant (distilled water) flowing into the compressor and has a

²⁹This oil adsorber should be replaced after 20,000 hours of operation. The moving parts of the cold head should be replaced after 10,000 hours of operation. We were overdue with this maintenance, where the maintenance was done at 33632.1 hours of operation.

³⁰This is separated from the helium in VIS. The high-pressure helium gas is in the Sumitomo compressor.

³¹Cooling water flow rate of 6 to 9 L/min with 5°C to 25°C inlet temperature. When in doubt, please refer to Sumitomo F-70L manual.

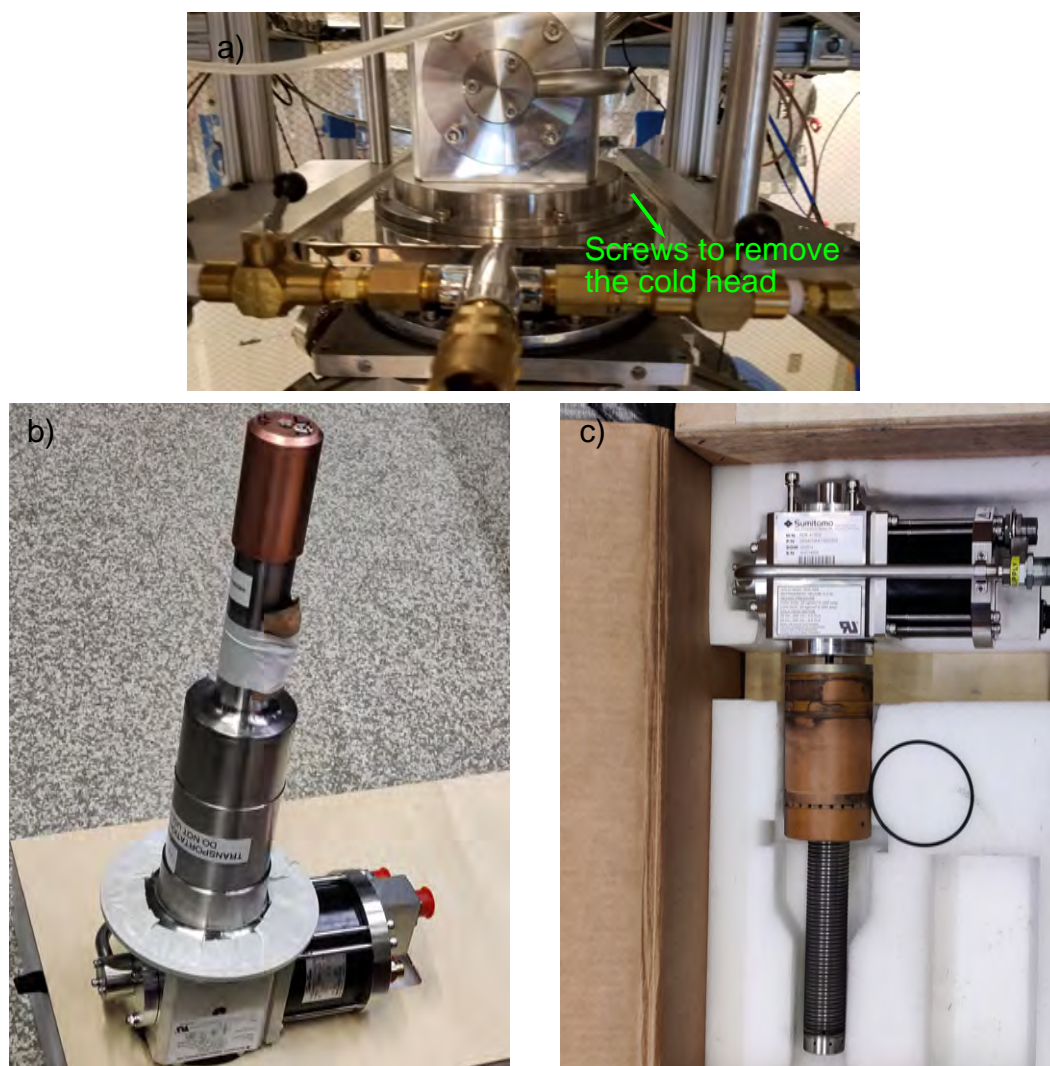


Figure 3.20: Cold head. a) The screws (green arrow) are loosened to remove the cold head from the top plate without removing the copper coil from Fig. 3.16. b) Refurbished cold head from Sumitomo. c) The old cold head.

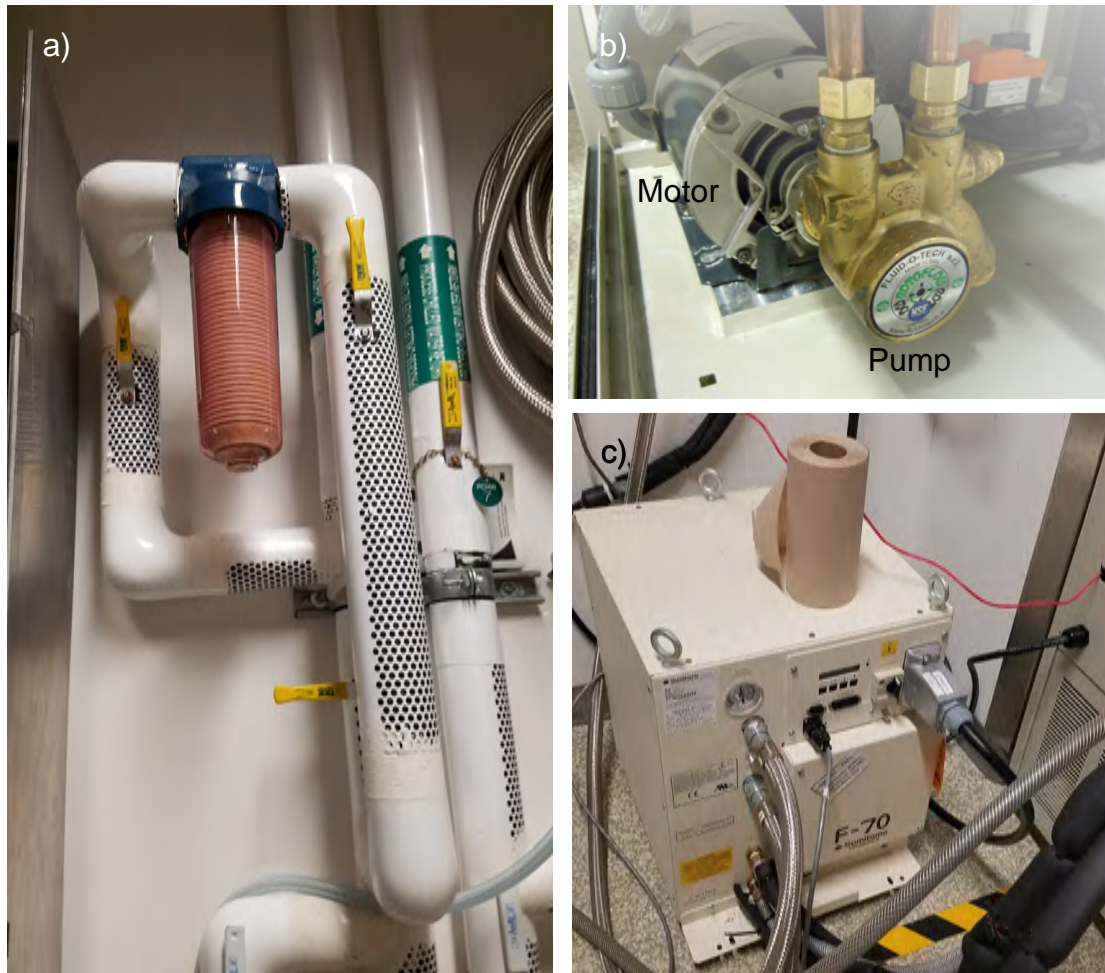


Figure 3.21: Chiller to compressor. a) The building chilled water is filtered before entering the chiller. b) The pump and motor that circulate the coolant into the compressor. c) An example of compressor connections.

separate chilled water line from the building to cool the chiller. The building chilled water passes through a filter (Fig. 3.21 a) before going into the chiller. This filter needs to be changed, ensuring effective cooling of the chiller³².

Another possible failure is from the chiller pump (Fig.3.21 b). There is a plastic mechanical ‘fuse’ between the motor and pump to protect the motor. Once this fuse is worn out, the chiller is unable to pump, resulting in the compressor shut down (a safety mechanism)³³. Currently, we do not have a mechanism to estimate the damage on the fuse as it is hidden between the motor and pump.

³²We did not change the filter for two years. We observed the temperature of the coolant as indicated by the front panel of the chiller creeping up, and eventually, the compressor stopped due to its safety mechanism. Since then, we have changed the filter at least once per year. It is advisable to have a scheduled maintenance before an experimental project.

³³It may sound terrifying that the system needs maintenance or shut down, but the system can be easily recovered after all the fixes are implemented.

Chapter 4: Quantum Simulations Toolbox

The ability to perform the coherent rotation of the spins is essential for quantum computing/simulation purposes. One of the techniques is applying a resonant electromagnetic field to Rabi flop between the qubit in a two-level system. Then, the time/power of the resonant electromagnetic field is varied to perform coherent rotation. In the lab setup, the coherent rotation is implemented with a resonant microwave field or a mode-locked 355 nm laser to the $^{171}\text{Yb}^+$ hyperfine qubit. The 12.64 GHz energy splitting of the hyperfine qubit can be generated conveniently with a microwave horn setup outside the apparatus with only global control on the ion chain¹. Individual control can be implemented with individual addressing mode-locked 355 nm via stimulated Raman transition for each ion in the chain. However, in the current setup, we have only global addressing Raman beams. Furthermore, we use two counter-propagating Raman beams to perform the Mølmer-Sørensen scheme [24] for entangling the trapped ions. However, with microwave, the entangling is too weak as the wavelength of the microwave (2.38 cm) is significantly larger than 355 nm.

¹Coherent qubit rotation and entangling gates with microwave are demonstrated in Ref. [54,55].

4.1 Two-level System

Here, we shall start with an atom-field interaction in a two-level system. Let's assume a monochromatic electric field with frequency ω and wavevector k from the laser addressing the transition of the ground state to the excited state $|g\rangle \leftrightarrow |e\rangle$. The electric field is:

$$E(t) = \hat{e} \frac{E_0}{2} [e^{i\omega t} + e^{-i\omega t}] \quad (4.1)$$

The atom-field Hamiltonian is $H_{AF} = -\vec{d} \cdot E(t)$, where the dipole operator $\vec{d} = -|e\rangle \langle g| + |g\rangle \langle e|$, where $\sigma_- = |g\rangle \langle e|$, $\sigma_+ = |e\rangle \langle g|$ and E_0 is the amplitude of the electric field. The ground state energy level is defined as zero energy and excited state is defined as ω_e . The atom Hamiltonian is $H_A = 0 |g\rangle \langle g| + \omega_e |e\rangle \langle e|$. The total atom-field Hamiltonian is $H = H_A + H_{AF}$.

Let's assume the wavefunction $|\Psi(t)\rangle$ and $|\Psi_I(t)\rangle = e^{iH_A t} |\Psi(t)\rangle$ in the interaction picture. $|\Psi_I(t)\rangle$ evolves in the time-dependent Schrödinger equation, $i \frac{\partial |\Psi_I(t)\rangle}{\partial t} = H_{AF} |\Psi_I(t)\rangle$. Therefore, in the interaction picture, H_{AF} is

$$\begin{aligned} H_{AF} &\Rightarrow e^{iH_A t} H_{AF} e^{-iH_A t} \\ &= \frac{\Omega_R}{2} (\sigma_+ e^{i\omega_e t} + \sigma_- e^{-i\omega_e t}) [e^{i\omega t} + e^{-i\omega t}] \\ &= \frac{\Omega_R}{2} (\sigma_+ e^{-i(\omega+\omega_e)t} + \sigma_- e^{i(\omega+\omega_e)t} + \sigma_+ e^{-i(\omega-\omega_e)t} + \sigma_- e^{i(\omega-\omega_e)t}) \\ &\quad \Downarrow (RWA) \\ &= \frac{\Omega_R}{2} (\sigma_+ e^{-i(\omega-\omega_e)t} + \sigma_- e^{i(\omega-\omega_e)t}) \end{aligned} \quad (4.2)$$

$$\Omega_R = -E_0 \langle g | \hat{e} \cdot \vec{d} | e \rangle$$

Rotating Wave Approximation (RWA) used to remove fast oscillation and the cross-terms in the interaction picture of H_{AF} . Therefore, in the Schrödinger, the atom-field

Hamiltonian is simplified to

$$H_{AF} = \frac{\Omega_R}{2}(\sigma_+ e^{-i\omega t} + \sigma_- e^{i\omega t}) \quad (4.3)$$

4.2 Three-level System

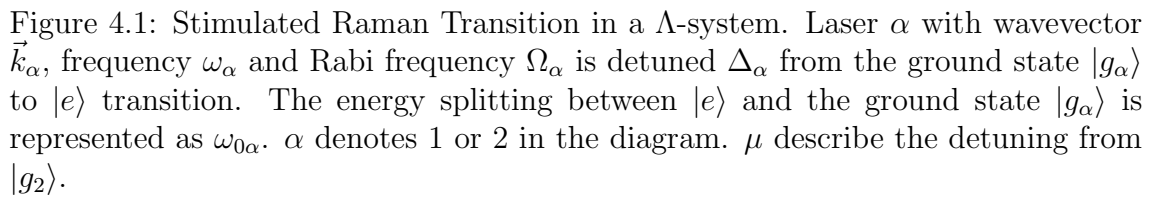
Once the qubit is initialized to $|\downarrow_z\rangle$, two 355 nm mode-locked beams are shined onto the atoms to undergo stimulated Raman transition. In $^{171}\text{Yb}^+$, the Raman beams are detuned 33 THz from the $^2\text{P}_{1/2}$ state and 66 THz from the $^2\text{P}_{3/2}$. This can be simplified into a three-level Λ system for the two-photon stimulated Raman transition (Fig. 4.1). The ground states $|g_1\rangle$ and $|g_2\rangle$ are coupled via the excited state $|e\rangle$ with two lasers with wavevector \vec{k}_1, \vec{k}_2 and frequencies ω_1, ω_2 respectively. Both lasers are detuned away from the excited state by $\Delta = \Delta_1 = \Delta_2$. Here, the spontaneous emission is neglected since $\Delta_{1(2)} \gg \Gamma$, where Γ is the decay rate of $|e\rangle$. The derivation here will be based on Ref. [56]. The atomic Hamiltonian (diagonal matrix) in the absence of the coupling fields is:

$$H_A = -\omega_{01} |g_1\rangle\langle g_1| - \omega_{02} |g_2\rangle\langle g_2| + 0 |e\rangle\langle e| \quad (4.4)$$

where $\hbar = 1$ and the excited state energy is defined as the zero energy. The atom-field Hamiltonian is $H_{AF} = -\vec{d} \cdot \vec{E}$.

$$\vec{d} = \sum_{g_1, g_2} \langle g_1 | \vec{d} | e \rangle \sigma_{1-} + \langle g_2 | \vec{d} | e \rangle \sigma_{2-} + \langle e | \vec{d} | g_1 \rangle \sigma_{1+} + \langle e | \vec{d} | g_2 \rangle \sigma_{2+} \quad (4.5)$$

where $|g_1\rangle\langle e| = \sigma_{1-}$, $|g_2\rangle\langle e| = \sigma_{2-}$, $|e\rangle\langle g_1| = \sigma_{1+}$ and $|e\rangle\langle g_2| = \sigma_{2+}$ and each of them has their respective dipole matrix element. The dipole operator contributes to an off-diagonal matrix, where it couples both ground states to the excited state but not



between both ground states. Here, we assume the electric field \vec{E} is monochromatic

:

$$E_1(\vec{r}, t) = \hat{\epsilon}_1 \frac{E_1}{2} [e^{i(\omega_1 t - k_1 \cdot r)} + e^{-i(\omega_1 t - k_1 \cdot r)}] \quad (4.6)$$

$$E_2(\vec{r}, t) = \hat{\epsilon}_2 \frac{E_2}{2} [e^{i((\omega_2 + \mu)t - k_2 \cdot r + \varphi)} + e^{-i((\omega_2 + \mu)t - k_2 \cdot r + \varphi)}] \quad (4.7)$$

$$\vec{E} = E_1(\vec{r}, t) + E_2(\vec{r}, t) \quad (4.8)$$

with unit polarization ϵ_α , amplitude E_α , laser frequency detuning $\mu = \delta\omega - \omega_{HF}$ and additional phase φ on $E_2(\vec{r}, t)$. Here, H_{AF} can be extended from Eq. 4.3.

$$H_{AF} = \begin{pmatrix} 0 & 0 & \frac{\Omega_1}{2} e^{-ik_1 r} e^{i\omega_1 t} \\ 0 & 0 & \frac{\Omega_2}{2} e^{-ik_2 r} e^{i(\omega_2 + \mu)t} e^{i\varphi} \\ \frac{\Omega_1}{2} e^{ik_1 r} e^{-i\omega_1 t} & \frac{\Omega_2}{2} e^{ik_2 r} e^{-i(\omega_2 + \mu)t} e^{-i\varphi} & 0 \end{pmatrix} \quad (4.9)$$

The Rabi frequencies is defined as:

$$\Omega_\alpha := -\langle g_\alpha | \hat{\epsilon}_\alpha \cdot \vec{d} | e \rangle E_\alpha ; \alpha = 1, 2 \quad (4.10)$$

where it describes the coupling strength from $|g_\alpha\rangle$ to $|e\rangle$. The total Hamiltonian is thus $H = H_A + H_{AF}$.

4.2.1 Time-Dependent Schrödinger Equation

In order to understand the time evolution of this system, we need to solve the time-dependent Schrödinger equation, $i \frac{\partial |\psi(t)\rangle}{\partial t} = H |\psi(t)\rangle$. Thus, the state vector can be defined as:

$$|\psi(t)\rangle = c_1(t) |g_1\rangle + c_2(t) |g_2\rangle + c_e(t) |g_e\rangle \quad (4.11)$$

The time-dependent Schrödinger equation is the following:

$$\begin{pmatrix} \dot{c}_1(t) \\ \dot{c}_2(t) \\ \dot{c}_e(t) \end{pmatrix} = -i \begin{pmatrix} -\omega_{01}c_1(t) + c_e(t)e^{i(-k_1 \cdot r + \omega_1 t)} \\ -\omega_{02}c_2(t) + c_e(t)e^{i(-k_2 \cdot r + [\omega_2 + \mu]t)}e^{i\varphi} \\ c_1(t)\frac{\omega_1}{2}e^{i(k_1 \cdot r - \omega_1 t)} + c_2(t)\frac{\omega_2}{2}e^{i(k_2 \cdot r - [\omega_2 + \mu]t)}e^{-i\varphi} \end{pmatrix} \quad (4.12)$$

Eq. 4.12 is a set of equation of motion with oscillation terms from the electric fields.

We can choose a frame such that these oscillations disappear. Therefore, we choose a rotating-frame where the state vector is:

$$|\psi(t)\rangle = \tilde{c}_1(t) |g_1\rangle + \tilde{c}_2(t) |g_2\rangle + \tilde{c}_e(t) |g_e\rangle \quad (4.13)$$

where slow-varying coefficients denoted as:

$$\tilde{c}_\alpha(t) = c_\alpha(t)e^{-i\omega_\alpha t} \quad (4.14)$$

The new set of equations is as follows:

$$\begin{pmatrix} \dot{\tilde{c}}_1(t) \\ \dot{\tilde{c}}_2(t) \\ \dot{\tilde{c}}_e(t) \end{pmatrix} = -i \begin{pmatrix} -\Delta_1\tilde{c}_1(t) + \frac{\Omega_1}{2}e^{-ik_1 \cdot r}\tilde{c}_e(t) \\ -\Delta_2\tilde{c}_2(t) + \frac{\Omega_2}{2}e^{-ik_2 \cdot r}e^{i(\mu t + \varphi)}\tilde{c}_e(t) \\ \frac{\Omega_1}{2}e^{ik_1 \cdot r}\tilde{c}_1(t) + \frac{\Omega_2}{2}e^{ik_2 \cdot r}e^{-i(\mu t + \varphi)}\tilde{c}_2(t) \end{pmatrix} \quad (4.15)$$

with a new effective Hamiltonian.

$$\tilde{H}_{eff} = \begin{pmatrix} -\Delta_1 & 0 & \frac{\Omega_1}{2}e^{-ik_1 \cdot r} \\ 0 & -\Delta_2 & \frac{\Omega_2}{2}e^{-ik_2 \cdot r}e^{i(\mu t + \varphi)} \\ \frac{\Omega_1}{2}e^{ik_1 \cdot r} & \frac{\Omega_2}{2}e^{ik_2 \cdot r}e^{-i(\mu t + \varphi)} & 0 \end{pmatrix} \quad (4.16)$$

4.2.2 Adiabatic Elimination - Two-level Dynamics

We boost the rotating frame² by $-\Delta$ where $\Delta = \frac{\Delta_1 + \Delta_2}{2}$ and follow the steps as shown from Eq. 4.13-4.16. Here, we define the state vector as $|\Psi\rangle = \phi_{g1} |g_1\rangle + \phi_{g2} |g_2\rangle + \phi_e |e\rangle$. The equation of motion of this rotated frame is:

$$\begin{pmatrix} \dot{\phi}_{g1} \\ \dot{\phi}_{g2} \\ \dot{\phi}_e \end{pmatrix} = -i \begin{pmatrix} (\Delta_1 - \Delta)\phi_{g1} + \frac{\Omega_1}{2}e^{-ik_1 \cdot r}\phi_e \\ (\Delta_2 - \Delta)\phi_{g2} + \frac{\Omega_2}{2}e^{-ik_2 \cdot r}e^{i(\mu t + \varphi)}\phi_e \\ \frac{\Omega_1}{2}e^{ik_1 \cdot r}\phi_{g1} + \frac{\Omega_2}{2}e^{ik_2 \cdot r}e^{-i(\mu t + \varphi)}\phi_{g2} - \Delta\phi_e \end{pmatrix} \quad (4.17)$$

Here, $|\Delta_2 - \Delta_1| \ll |\Delta|$, which ϕ_e has a fast time dependence, thus we can adiabatically eliminate ϕ_e as it will achieve an equilibrium state instantaneously where $\dot{\phi}_e = 0$. Therefore, the solution of ϕ_e is in terms of ϕ_{g1} and ϕ_{g2} where

$$\phi_e = \frac{\Omega_1}{2\Delta}e^{ik_1 \cdot r}\phi_{g1} + \frac{\Omega_2}{2\Delta}e^{ik_2 \cdot r}e^{-i(\mu t + \varphi)}\phi_{g2} \quad (4.18)$$

Now, substitute Eq. 4.18 into Eq. 4.17 and two-level system is obtained.

$$\begin{pmatrix} \dot{\phi}_{g1} \\ \dot{\phi}_{g2} \end{pmatrix} = -i \begin{pmatrix} (\Delta_1 + \omega_{AC1})\phi_{g1} + \frac{\Omega_R}{2}e^{i(k_2 - k_1) \cdot r}e^{i(\mu t + \varphi)}\phi_{g2} \\ (\Delta_2 + \omega_{AC2})e^{-i(\mu t + \varphi)}\phi_{g2} + \frac{\Omega_R}{2}e^{-i(k_2 - k_1) \cdot r}\phi_{g1} \end{pmatrix} \quad (4.19)$$

This gives an effective two-level system

$$H_{2-level} = \begin{pmatrix} \Delta_1 + \omega_{AC1} & \frac{\Omega_R}{2}e^{i\Delta k \cdot r}e^{i(\mu t + \varphi)} \\ \frac{\Omega_R}{2}e^{-i\Delta k \cdot r}e^{-i(\mu t + \varphi)} & \Delta_2 + \omega_{AC2} \end{pmatrix} \quad (4.20)$$

where $\Delta k = k_2 - k_1$, with Raman Rabi frequency

$$\Omega_R := \frac{\Omega_1 \Omega_2}{2\Delta} \quad (4.21)$$

²As mentioned in Ref. [56], choosing the appropriate frame is important for adiabatic elimination.

and AC Stark shift from each beam

$$\Omega_{AC\alpha} := \frac{\Omega_\alpha^2}{4\Delta} \quad (4.22)$$

For simplicity and compactness of notations, $H_{2-level} = (\Delta_1 + \omega_{AC1}) |g_1\rangle\langle g_1| + (\Delta_2 + \omega_{AC2}) |g_2\rangle\langle g_2| + \frac{\Omega_R}{2} e^{i\Delta k \cdot r} e^{i(\mu t + \varphi)} \sigma_- + \frac{\Omega_R}{2} e^{-i\Delta k \cdot r} e^{-i(\mu t + \varphi)} \sigma_+$, where $\sigma_- = |g_1\rangle\langle g_2|$ and $\sigma_+ = |g_2\rangle\langle g_1|$.

4.2.3 Carrier Transition

Based on Eq. 4.20, the interactions (off-diagonal) Hamiltonian H_I is

$$H_I = \frac{\Omega_R}{2} e^{i\Delta k \cdot r} e^{i(\mu t + \varphi)} \sigma_- + \frac{\Omega_R}{2} e^{-i\Delta k \cdot r} e^{-i(\mu t + \varphi)} \sigma_+ \quad (4.23)$$

For carrier transition in co-propagating³ Raman with $\mu = 0$ and $\Delta k = 0$, the carrier effective atom-field interaction Hamiltonian is:

$$\begin{aligned} H_{carr} &= \frac{\Omega_R}{2} [e^{i\varphi} \sigma_- + e^{-i\varphi} \sigma_+] \\ &= \frac{\Omega_R}{4} [(\sigma_x + i\sigma_y) e^{i\varphi} + (\sigma_x - i\sigma_y) e^{-i\varphi}] \\ &= \frac{\Omega_R}{2} [\sigma_x (\frac{e^{i\varphi} + e^{-i\varphi}}{2}) + i\sigma_y (\frac{e^{i\varphi} - e^{-i\varphi}}{2})] \\ &= \frac{\Omega_R}{2} [\sigma_x \cos \varphi + i\sigma_y \sin \varphi] \end{aligned} \quad (4.24)$$

where φ sets the axis of rotation of the single qubit operation.

4.2.4 Sideband Transitions

In the sideband transition, the two Raman beams are non-copropagating⁴,

where $\Delta k \neq 0$. As a result, $\Delta k \cdot r = \eta(\hat{a}e^{-i\omega_{tr}t} + \hat{a}^+e^{i\omega_{tr}t})$, where the Lamb-Dicke

³For simplicity, a co-propagating Raman scheme is considered here. Ref. [57] provides the derivation for a non co-propagating Raman scheme, where $\Delta k \neq 0$.

⁴When the two Raman beams are in the counter-propagating configuration, $\Delta k = 2k = 4\pi/\lambda$ with λ as the wavelength of the laser.

parameter $\eta = \Delta k r_0$, a^+ and a are the creation and annihilation operators. The characteristic length scale of the motional mode $r_0 = \sqrt{1/(2m\omega_{tr})}$, where ω_{tr} is the motional modes of the quantum harmonic oscillator. Let's substitute η into Eq. 4.23, with the assumption that the atoms are in the resolved sideband limit and $\eta \ll 1$. Therefore, the exponential term of the η can be Taylor expanded, to obtain the sideband transitions.

$$\begin{aligned}
H_{sideband} &= \frac{\Omega_R}{2} [e^{i\eta(\hat{a}e^{-i\omega_{tr}t} + \hat{a}^+e^{i\omega_{tr}t})} e^{i(\mu t + \varphi)} \sigma_- + e^{-i\eta(\hat{a}e^{-i\omega_{tr}t} + \hat{a}^+e^{i\omega_{tr}t})} e^{-i(\mu t + \varphi)} \sigma_+] \\
&\approx \frac{\Omega_R}{2} [(1 + i\eta(\hat{a}e^{-i\omega_{tr}t} + \hat{a}^+e^{i\omega_{tr}t}) e^{i(\mu t + \varphi)}) \sigma_- \\
&\quad + (1 - i\eta(\hat{a}e^{-i\omega_{tr}t} + \hat{a}^+e^{i\omega_{tr}t}) e^{-i(\mu t + \varphi)}) \sigma_+]
\end{aligned} \tag{4.25}$$

For the blue sideband transition (Fig. 4.1), $\mu = \omega_{tr}$:

$$\begin{aligned}
H_{Blue} &\approx \frac{\Omega_R}{2} [(1 + i\eta(\hat{a}e^{-i\omega_{tr}t} + \hat{a}^+e^{i\omega_{tr}t}) e^{i((\omega_{tr})t + \varphi)}) \sigma_- \\
&\quad + (1 - i\eta(\hat{a}e^{-i\omega_{tr}t} + \hat{a}^+e^{i\omega_{tr}t}) e^{-i((\omega_{tr})t + \varphi)}) \sigma_+] \\
&\approx i \frac{\eta \Omega_R}{2} [\hat{a} \sigma_- e^{i\varphi} - \hat{a}^+ \sigma_+ e^{-i\varphi}]
\end{aligned} \tag{4.26}$$

where RWA is applied to obtain the second part of the equation. $\mu = \omega_{tr}$ describes when the transition is on resonant of the blue sideband transistion. A π -blue sideband transition will increase the motional mode by a quanta of energy. It transforms $|\downarrow_z, n\rangle \leftrightarrow |\uparrow_z, n+1\rangle$.

For the red sideband transition, $\mu = -\omega_{tr}$:

$$H_{Red} \approx i \frac{\eta \Omega_R}{2} [\hat{a}^+ \sigma_- e^{-i\varphi} - \hat{a} \sigma_+ e^{i\varphi}] \tag{4.27}$$

$\mu = -\omega_{tr}$ describes when the transition is resonant with the red sideband transition. A π -red sideband transition will decrease the motional mode by a quanta of energy.

It transforms $|\downarrow_z, n\rangle \leftrightarrow |\uparrow_z, n-1\rangle$. With these toolboxes presented here, we can now generate the Ising interaction, which will be explained in the next section.

4.3 Generating Long-Range Transverse Field Ising Model

The quantum simulation experiments presented here are long-range Transverse Field Ising Model (TFIM) [3].

$$H = \sum_{i<j} J_{ij} \sigma_i^x \sigma_j^x + B \sum_i \sigma_i^\zeta \quad (4.28)$$

with Ising interaction J_{ij} , transverse magnetic field B and Pauli matrix on i th spin in ζ -direction of the Bloch sphere σ_i^ζ , where $\zeta = x, y, z$. $J_{ij} \approx J_0/|i-j|^\alpha$ is the power-law decaying Ising coupling between spins i and j with the tunable exponent α . This effective Hamiltonian is generated using Mølmer-Sørensen scheme [24, 25], where the motional modes are excited off-resonantly. We are interested in this class of models in quantum magnetism where quantum phase transition is present [58].

4.3.1 Ising Interaction

We generate the spin-spin interaction with a pair of non-copropagating 355nm Raman beams. The beatnote wavevector Δk from the Raman beams is along the transverse motional modes of the ion chain to apply spin-dependent dipole forces. For the Mølmer-Sørensen scheme implemented in this thesis, two laser beatnotes which are detuned symmetrically from the m th motional modes δ_m with frequencies $\omega_{HF} \pm (\omega_{tr} + \delta_m)$. Using the Eq. 4.25 for both detuned red and blue sideband

transitions⁵, the effective Hamiltonian is simplified to [52]:

$$H_{MS} = \sum_{i,m} \frac{\eta_{im}\Omega_i}{2} (a_m e^{-i\omega_m t} + a_m^+ e^{i\omega_m t}) \cos(\mu t + \phi_m) \sigma_{\phi_s}^i \quad (4.29)$$

where the Lamb-Dicke parameteres is $\eta_{im} = b_{im}\Delta k \sqrt{1/(2m\omega_m)}$ with the normal mode transformation matrix b_{im} of the i th ion with m th normal mode where $\sum_{im} |b_{im}|^2 = 1$ and Rabi frequency of i th ion is Ω_i . Since in this derivation, the spin and motion phases are separated. We define $\sigma_{\phi_s} = e^{i\phi_s}\sigma_- + e^{-i\phi_s}\sigma_+$ and motional phases ϕ_m . Let $\phi_m \equiv \frac{(\varphi_R - \varphi_B)}{2}$ and $\phi_s \equiv \frac{(\varphi_R + \varphi_B + \pi)}{2}$, with φ_R and φ_B as the phases on the red and blue bichromatic tones. We set $\varphi_R = 0$, $\varphi_B = \pi \Rightarrow \phi_m = \pi/2$, $\phi_s = \pi$, which $\sigma_{\phi_s} = -\sigma_x$.

$$H_{MS} = - \sum_{i,m} \frac{\eta_{im}\Omega_i}{2} (a_m e^{-i\omega_m t} + a_m^+ e^{i\omega_m t}) \sin(\mu t) \sigma_x^i \quad (4.30)$$

This effective Hamiltonian H_{MS} is time-dependent. Therefore, the time evolution $U(t)$ can be approximated with Magnus expansion.

$$U(t) = T[e^{-i \int_0^t dt_1 H_{MS}(t_1)}] = e^{\overline{H}} \quad (4.31)$$

$$\overline{H} = \overline{H}^{(1)} + \overline{H}^{(2)} + \overline{H}^{(3)} + \dots \quad (4.32)$$

$$\overline{H}^{(1)} = -i \int_0^t H(t_1) dt_1 \quad (4.33)$$

$$\overline{H}^{(2)} = -\frac{1}{2} \int_0^t dt_1 \int_0^{t_1} dt_2 [H(t_1), H(t_2)] \quad (4.34)$$

$$\overline{H}^{(3)} = -\frac{i}{6} \int_0^t dt_1 \int_0^{t_1} dt_2 \int_0^{t_2} dt_3 ([H(t_1), H(t_2)], H(t_3)) + ([H(t_3), H(t_2)], H(t_1)) \quad (4.35)$$

⁵Unlike the individual cases from Eq. 4.27 and 4.26, it considers both co-rotating and counter-rotating components and then applies RWA later.

with T as the time operator.

$$\overline{H}^{(1)} = \sum_{im} [\alpha_{i,m}(t) a_m^+ - \alpha_{i,m}^*(t) a_m] \sigma_x^i \quad (4.36)$$

$$\Downarrow \quad (4.37)$$

$$\alpha_{i,m}(t) = \frac{i\eta_{im}\Omega_i}{\mu^2 - \omega_m^2} [\mu - e^{i\omega_m t} (\mu \cos(\mu t) - i\omega_m \sin(\mu t))] \quad (4.38)$$

For $\overline{H}^{(2)}$, the only non-commuting term in $[H(t_1), H(t_2)]$ are $[a_m, a_n^+] = \delta_{mn}$. Therefore, the remaining terms are

$$[\sigma_x^i a_m e^{-i\omega_m t_1}, \sigma_x^j a_n^+ e^{i\omega_n t_2}] = \delta_{mn} \sigma_x^i \sigma_x^j e^{-i\omega_m t_1} e^{i\omega_n t_2} \quad (4.38)$$

$$[\sigma_x^i a_m^+ e^{i\omega_m t_1}, \sigma_x^j a_n e^{-i\omega_n t_2}] = -\delta_{mn} \sigma_x^i \sigma_x^j e^{i\omega_m t_1} e^{-i\omega_n t_2}$$

$$\begin{aligned} \overline{H}^{(2)} = & \frac{i}{2} \sum_{i < j, m} \frac{\eta_{i,m} \eta_{j,m} \Omega_i \Omega_m}{\mu^2 - \omega_m^2} \left[\frac{\mu \sin[(\mu - \omega_m)t]}{\mu - \omega_m} \right. \\ & \left. - \frac{\mu \sin[(\mu + \omega_m)t]}{\mu + \omega_m} + \frac{\omega_m \sin(2\mu t)}{2\mu} - \omega_m t \right] \sigma_x^i \sigma_x^j \end{aligned} \quad (4.39)$$

The higher order of the Magnus expansion is $H^{(j>2)} = 0$. With the Magnus expansion, the time evolution $U(t)$ can be split into two parts:

$$U(t) = \exp\left[\left(\sum_i \phi_i(t) \sigma_x^i + i \sum_{i < j} \chi_{ij}(t) \sigma_x^i \sigma_x^j\right)\right] \quad (4.40)$$

The first term describes the spin-motion coupling.

$$\phi_i(t) = \sum_m [\alpha_{i,m}(t) a_m^+ - \alpha_{i,m}^*(t) a_m] \quad (4.41)$$

In fact, $\phi_i(t)$ is a displacement operation $\mathcal{D} = \exp(\alpha(t) a^+ - \alpha^*(t) a)$.

The second term describes the spin-spin coupling

$$\begin{aligned} \chi_{ij}(t) = & \frac{1}{2} \sum_{i < j, m} \frac{\eta_{i,m} \eta_{j,m} \Omega_i \Omega_m}{\mu^2 - \omega_m^2} \left[\frac{\mu \sin[(\mu - \omega_m)t]}{\mu - \omega_m} \right. \\ & \left. - \frac{\mu \sin[(\mu + \omega_m)t]}{\mu + \omega_m} + \frac{\omega_m \sin(2\mu t)}{2\mu} - \omega_m t \right] \end{aligned} \quad (4.42)$$

There are two regimes where they contribute to the spin-spin coupling, with the assumption that the evolution times to be longer than the periodic oscillation of the ion ($\omega_m t \gg 1$).

The first regime is the “fast” region where the μ is detuned close to ω_m . This is achieved by ensuring all $\alpha_{i,m}(t) = 0$ at all times which requires $2N + 1$ control parameters [59], where N is the number of ions for a set of motional modes. This imposes a complex control problem as the solutions are pre-calculated to obtain the highest entanglement fidelity. However, the number of control parameters can be reduced by choosing the appropriate detuning δ from ω_m for entanglement operations [59–61] .

The second regime is the “slow” regime where μ is detuned far from ω_m relative to the sideband Rabi frequency ($|\mu - \omega_m| \gg \eta_{im}\Omega_i$). In this regime, the spin-motion coupling becomes negligible as $\alpha_{i,m}(t) \ll 1$. As a result of this regime, the last term of Eq. 4.42 grows linearly with time and will dominate the time evolution and the other terms are neglected, $\chi_{ij}(t) = \frac{1}{2} \sum_{i < j, m} \frac{\eta_{i,m}\eta_{j,m}\Omega_i\Omega_j}{\mu^2 - \omega_m^2} \omega_m t$.

$$H_{Ising} = \frac{1}{2} \sum_{i < j, m} \frac{\eta_{i,m}\eta_{j,m}\Omega_i\Omega_j}{\mu^2 - \omega_m^2} \omega_m \sigma_x^i \sigma_x^j \quad (4.43)$$

\Downarrow

$$= \sum_{i < j, m} J_{ij} \sigma_x^i \sigma_x^j \quad (4.44)$$

Thus, the effective Hamiltonian is the Ising Hamiltonian. This can also be written as:

$$J_{i,j} = \Omega^2 \nu_R \sum_m \frac{b_{i,m} b_{j,m}}{\mu^2 - \omega_m^2} \approx \frac{J_0}{|i - j|^\alpha} \quad (4.45)$$

where $\nu_R = \hbar \Delta k^2 / (2m)$ is the recoil frequency. $J_{i,j} \approx J_0 / |i - j|^\alpha$ is the power-law

decaying Ising coupling between spins i and j with tunable exponent α , $J_0 > 0$.

In the experiment, we implement quantum simulation in the slow regime. The red and blue beatnotes are detuned away from all the ω_m with ω_{COM} to be the closest from the detuning. However, there is a practical limit on how far $\delta = |\mu - \omega_{COM}|$ can go because spin-spin interaction strength also decreases with δ . In the experiment, we choose $\delta = 3\eta\Omega$ to obtain a reasonable spin-spin interaction while minimizing the spin-motion entanglement [62]. The $\eta\Omega$ here is calibrated with a single ion where $\eta\Omega = \sqrt{\Omega_{\text{red}}\Omega_{\text{blue}}}$ and $\Omega_{\text{red (blue)}}$ is the red (blue) sideband Rabi frequency. Although the second scheme has phonon error, this scheme is implemented in the context of analog quantum simulation, which does not require as high fidelity entangling gates as in digital quantum simulation.

4.3.2 Ising Interaction with Transverse B-fields

The B -fields along x and y directions can be generated using Eq. 4.24 by having a on-resonant third AOM tone when the Mølmer-Sørensen interaction is on. As for the effective B_z field, during the Mølmer-Sørensen interaction, the red and blue sidebands are detuned asymmetrically ($\omega_{\text{red}} = \omega_{HF} - \mu - 2B$, $\omega_{\text{blue}} = \omega_{HF} + \mu - 2B$). This changes the frame of reference of the qubit and with the appropriate rotating frame, it gives rise to the effective Hamiltonian is $H = \sum_{i < j, m} J_{ij} \sigma_x^i \cdot \sigma_x^j + B_z \sum_i \sigma_z^i$.

4.3.3 Cross Terms of Magnus Expansion

With the B -field on, the Magnus Expansion series from (Eq. 4.31) does not converge due to cross terms when the quantum quench of the H_{MS} (Eq. 4.30) and

carrier transition (Eq. 4.24) is applied.

$$\begin{aligned}
H_{MS} &= - \sum_{i,m} \frac{\eta_{im} \Omega_i}{2} (a_m e^{-i\omega_m t} + a_m^\dagger e^{i\omega_m t}) \sin(\mu t) \sigma_x^i \\
H_{Carr} &= \frac{\Omega_C}{2} \sigma_\zeta^i \\
H_{Total} &= H_{MS} + H_{Carr}
\end{aligned} \tag{4.46}$$

From Eq. 4.31, $\bar{H}^{(1)}$.

$$\bar{H}^{(1)} = \sum_{im} [\alpha_{i,m}(t) a_m^\dagger - \alpha_{i,m}^*(t) a_m] \sigma_x^i + \sum_i \frac{\Omega_C}{2} \sigma_\zeta^i t \tag{4.47}$$

The first term is from Eq. 4.36 and the second term in $\bar{H}^{(1)}$ is the B -field for the simulation. $\bar{H}^{(2)}$ remains unchanged for B_x -field because B_x commutes with H_{MS} . For $\zeta \neq x$, $\bar{H}^{(2)}$ has two additional time-dependent terms ($[H_{MS}(t_1), H_{Carr}(t_2)]$ and $[H_{Carr}(t_1), H_{MS}(t_2)]$) that contribute to the cross terms. Let's focus on the cross terms on the i th ion with the m th motional mode:

$$\begin{aligned}
\bar{H}_{Cross}^{(2)} &= -i \frac{\eta \Omega_i \Omega_C t}{2(\mu^2 - \omega_m^2)} [\mu(a_m + a_m^\dagger) + \frac{(-\mu + \omega_m)}{2} (a_m e^{-i(\mu+\omega_m)t}) \\
&\quad - \frac{(\mu + \omega_m)}{2} (a_m e^{i(\mu-\omega_m)t}) - \frac{(\mu + \omega_m)}{2} (a_m^\dagger e^{-i(\mu-\omega_m)t}) \\
&\quad + \frac{(-\mu + \omega_m)}{2} (a_m^\dagger e^{i(\mu+\omega_m)t})] \sigma_x \sigma_\zeta
\end{aligned} \tag{4.48}$$

$\Downarrow (RWA)$

$$\begin{aligned}
&= -i \frac{\eta \Omega_i \Omega_C t}{2(\mu^2 - \omega_m^2)} [\mu(a_m + a_m^\dagger) - \frac{(\mu + \omega_m)}{2} (a_m e^{i(\mu-\omega_m)t}) \\
&\quad - \frac{(\mu + \omega_m)}{2} (a_m^\dagger e^{-i(\mu-\omega_m)t})] \sigma_x \sigma_\zeta
\end{aligned}$$

All the terms in $\bar{H}_{Cross}^{(2)}$ grow linearly with time. With the experimental parameters, $\mu + \omega_m \sim 2\mu$ as $\mu = \omega_m + \delta$, where δ is the detuning. δ is on the order of 30 kHz

and $\mu \approx 4.5$ MHz. With these assumptions, the $\overline{H}_{Cross}^{(2)}$ is approximately:

$$\begin{aligned} \overline{H}_{Cross}^{(2)} = & -i \frac{\eta \Omega_i \Omega_C t}{4(\mu - \omega_m)} [(a_m + a_m^+) - (a_m e^{i(\mu - \omega_m)t}) \\ & - (a_m^+ e^{-i(\mu - \omega_m)t})] \sigma_x \sigma_\zeta \end{aligned} \quad (4.49)$$

Now, let's recall the cyclic relation of Pauli matrices to understand the cross terms.

$$\sigma_x = \begin{pmatrix} 0 & 1 \\ 1 & 0 \end{pmatrix} \quad (4.50)$$

$$\sigma_y = \begin{pmatrix} 0 & -i \\ i & 0 \end{pmatrix} \quad (4.51)$$

$$\sigma_z = \begin{pmatrix} 1 & 0 \\ 0 & -1 \end{pmatrix} \quad (4.52)$$

$$I = \begin{pmatrix} 1 & 0 \\ 0 & 1 \end{pmatrix} \quad (4.53)$$

$$[\sigma_x, \sigma_y] = 2i\sigma_z \quad [\sigma_y, \sigma_z] = 2i\sigma_x \quad [\sigma_z, \sigma_x] = 2i\sigma_y \quad (4.54)$$

When $\sigma_\zeta = \sigma_{y,z}$, $\overline{H}_{Cross}^{(2)}$ will yield σ_z and $-\sigma_y$ for $\zeta = y, z$ respectively. This contributes to additional spin-dependent phonon errors in the quantum simulation when both H_{MS} and H_{Carr} are applied simultaneously. The magnitude of this cross term is on the order $\frac{\eta \Omega \Omega_C}{4(\mu - \omega_m)}$. This Magnus expansion does not converge in which here we only investigate till the second-order term in the Magnus. The higher-order spin-dependent phonon terms are studied in Ref. [63, 64].

4.4 Details about the experiment on Raman

In Chapter 2, we show the results of motional modes along with the transverse directions of the trap because the Δk of the Raman beams overlaps with both principle axes of the trap (β and α). Therefore, the J_{ij} interactions in Eq. 4.43 can be generalized to:

$$J_{ij} = J_{ij}^{\alpha} + J_{ij}^{\beta} \quad (4.55)$$

In this trap, we can rotate the principal axes of the trap θ (Fig. 4.2). However, when one of the principle axes is aligned to the Raman Δk , the motional modes of the trap along these axes degenerate, resulting in inefficient Doppler cooling. In principle, another Doppler cooling laser can mitigate the issue but we are currently constrained by the space because we need another laser along the imaging path (z -direction). Therefore, during the experiment, we set that the frequency separation of both principle axes $\Delta\omega_{\alpha\beta}/2\pi = 121$ kHz, which gives us $\theta \approx 40^\circ$.

4.4.1 Estimation of the angle between a principal axis to Raman

The principal axes are orthogonal with each other. The Raman configuration in the lab overlaps with both principle axes of the trap (Fig. 4.2). The angle θ between the principal axes and the Raman Δk can be estimated by measuring the single-ion-on-resonant sideband Rabi frequency of the two transverse COM modes with the same RF power to the Raman AOMs. We then calculate the ratio of both

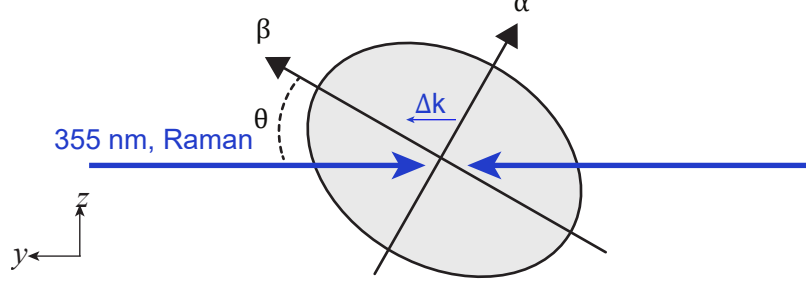


Figure 4.2: Raman orientation with respect to the principle axes of the trap. θ describes the angle between axis β to the Raman vector.

sideband Rabi frequencies $r = \frac{\eta_\beta \Omega_R}{\eta_\alpha \Omega_R}$. r can be expressed as the following:

$$r = \frac{\eta_\beta}{\eta_\alpha} \quad \eta_{\beta,\alpha} = \Delta k_{\beta,\alpha} x_{\beta,\alpha} = \Delta k_{\beta,\alpha} \sqrt{\frac{\hbar}{m\omega_{\beta,\alpha}}}$$

$$r = \frac{\Delta k_\beta}{\Delta k_\alpha} \sqrt{\frac{\omega_\alpha}{\omega_\beta}} \quad (4.56)$$

where m is the mass of $^{171}\text{Yb}^+$ and $\omega_{\beta,\alpha}$ is the COM motional mode along the principal axes β and α . This gives us the first equation to find θ . The second equation is $\Delta k^2 = \Delta k_\alpha^2 + \Delta k_\beta^2$. With these two equations, we can solve for Δk_α and Δk_β :

$$\Delta k_\alpha = \frac{\Delta k}{\sqrt{r^2 \frac{\omega_\beta}{\omega_\alpha} + 1}}$$

$$\Delta k_\beta = \frac{\Delta k}{\sqrt{r^2 \frac{\omega_\beta}{\omega_\alpha} + 1}} r \sqrt{\frac{\omega_\beta}{\omega_\alpha}} \quad (4.57)$$

Then, $\theta = \arctan \frac{\Delta k_\beta}{\Delta k_\alpha}$, with the experimental measured r .

Chapter 5: Ground-state Cooling

In the trapped ion platform, quantum information is encoded in the atomic state of the ion chain, in which the collective motion of the ion chain is used for entangling operations as described in the previous chapter. Therefore, it is crucial to develop a cooling mechanism that prepares near motional ground-state for high fidelity quantum operations [65]. This cooling process needs to be faster than the motional modes heating rate of the ion trap for efficient ground-state cooling. The few examples of sub-Doppler cooling are Sisyphus cooling [66], resolved sideband cooling (RSC) [67], electromagnetically induced transparency (EIT) cooling [68]. In the experiment, the initial cooling was done by Doppler cooling then followed by sub-Doppler cooling methods to cool the ions to the Lamb-Dicke regime. The two main sub-Doppler cooling techniques presented here are RSC and EIT cooling.

5.1 Resolved sideband cooling

Resolved sideband cooling (RSC) is a useful cooling method to cool atoms to their motional ground state. The atoms are typically first Doppler cooled to localize the atom and reach the Lamb-Dicke regime for effective RSC. The condition of the Lamb-Dicke regime is given as:

$$\eta^2(2n + 1) \ll 1 \tag{5.1}$$

where η is the Lamb-Dicke parameter and n as the motional quantum number of the atom's harmonic oscillator.

Let's assume a two-level system with energy splitting ω_0 between the $|\downarrow_z\rangle$ and $|\uparrow_z\rangle$ and harmonic motional mode of ω_m . The laser beam is tuned to address the red sideband transition with frequency $\omega_0 - \omega_m$. As derived in Eq. 4.27, a π red sideband transition will remove one motional quanta while flipping the spin state,

$$|\downarrow_z, n\rangle \rightarrow |\uparrow_z, n-1\rangle \quad (5.2)$$

Then, a carrier π pulse or optical pumping is applied to the atom

$$|\uparrow_z, n-1\rangle \rightarrow |\downarrow_z, n-1\rangle \quad (5.3)$$

The above sequences are applied again till the atom is in its motional ground state. In the lab, we apply Raman red sideband transition and follow by optical pumping (Fig. 5.1). This process is repeated for 30-40 cycles to achieve an average COM phonon number, $0.04 < \bar{n}_{COM} < 0.08$. For optimal RSC, the pulse duration of the red sideband transition is lengthened as the red sideband Rabi frequency decreases with phonon numbers. This cooling technique is a powerful tool to achieve ground-state cooling in trapped ions. However, RSC with only global control imposes practical challenges, especially in large trapped-ion crystals. As more the number of RSC pulses are applied, the cooling time scales linearly with time. For example, the heating rate of an already resolved-sideband-cooled motional mode increases the phonon number for this motional mode when other modes are resolved-sideband-cooled. This may result in worse initial temperature after Doppler cooling. However, there is a quadratic speed up in time with parallel sideband cooling with individual

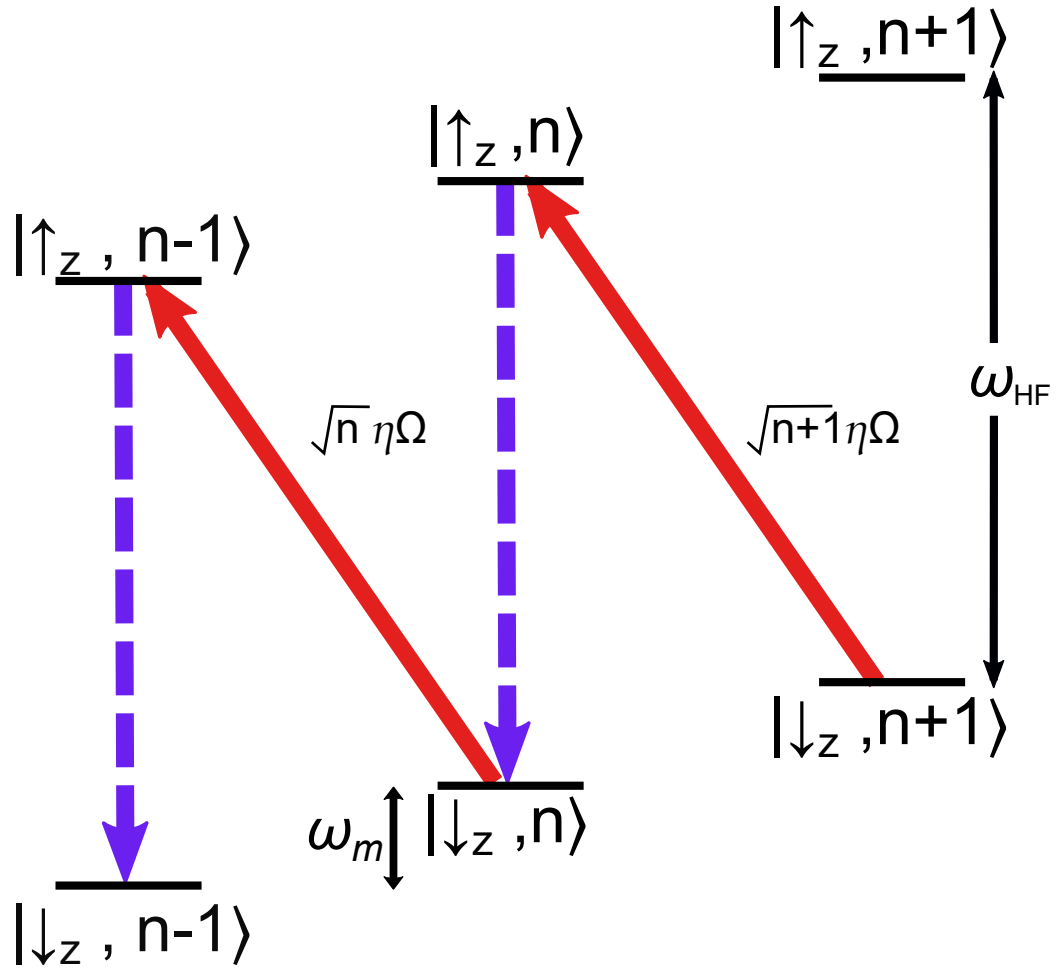


Figure 5.1: Raman sideband cooling. The spin is optical pumped to $|\downarrow_z, n\rangle$ state. A red sideband π $|\downarrow_z, n\rangle \rightarrow |\uparrow_z, n-1\rangle$ and optical pumping $|\uparrow_z, n-1\rangle \rightarrow |\downarrow_z, n-1\rangle$. This process is repeated and goes down to the harmonic oscillator ladder till the $n = 0$.

qubit addressing for RSC [69]. This provides an alternative scheme in RSC for the system with individual-qubit addressing, which the apparatus in this thesis currently does not.

5.2 Electromagnetically induced transparency (EIT) cooling

Another sub-Doppler cooling mechanism is EIT cooling, where it allows simultaneous ground-state cooling over a bandwidth of motional spectrum with only global control. The fundamental mechanism of EIT exploits quantum interference in a three-level Λ system to create a tunable spectroscopic profile for efficient cooling of ion chain within the desired bandwidth of motional modes. EIT [70] is an extension of “coherent population trapping” [71, 72] where the absorption of a transition is suppressed due to destructive interference from two transitions to the excited state in the Λ system [73, 74]. Here, we use EIT to suppress the carrier transition $|\downarrow_z, n\rangle \leftrightarrow |\uparrow_z, n\rangle$ and minimize the blue sideband transition $|\downarrow_z, n\rangle \leftrightarrow |\uparrow_z, n+1\rangle$ while maximize the red sideband transition $|\downarrow_z, n\rangle \leftrightarrow |\uparrow_z, n-1\rangle$ to achieve ground-state cooling¹. In $^{171}\text{Yb}^+$, EIT cooling works in a tripod-level configuration which can be reduced to an effective Λ system. Before we delve into EIT cooling in $^{171}\text{Yb}^+$, let’s start with EIT cooling in a three-level system.

5.2.1 Three-level system for EIT cooling

First, we will neglect the motional states and only consider a three-level system with ground state $|g\rangle$, excited state $|e\rangle$ and meta-stable or stable state $|r\rangle$ (Fig. 5.2 a). $|e\rangle$ are coupled to both $|g\rangle$ and $|r\rangle$ states via dipole transitions that can be

¹This is the punchline of EIT cooling mechanism.

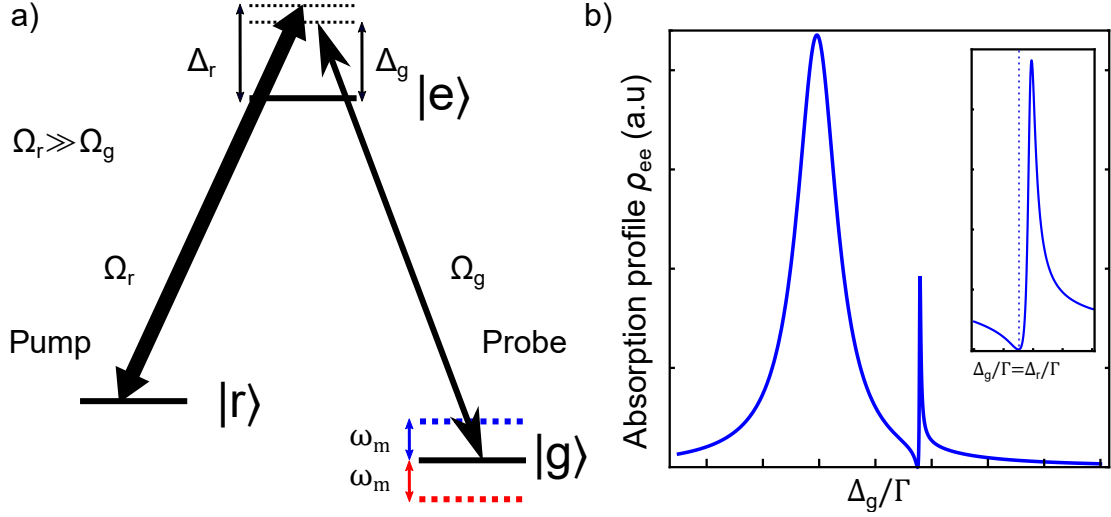


Figure 5.2: EIT cooling of the three-level system. a) The pump (probe) beam is detuned away from the excited state by Δ_r (Δ_g). The intensity of the pump beam is stronger than the probe beam ($\Omega_r \gg \Omega_g$). The blue (red) state is one quanta of the motional mode ω_m above (below) from $|g\rangle$. b) Absorption spectrum of the excited state ρ_{ee} as a function of Δ_g which is normalized with respect to the linewidth Γ of state $|e\rangle$. $\rho_{ee} = 0$ at $\Delta_g = \Delta_r$ as indicated by the blue dashed line in the inset.

generated with laser fields. A strong (pump) beam, with Rabi frequency Ω_r and detuning Δ_r , excites the transition $|r\rangle \rightarrow |e\rangle$ and a weak (probe) beam, with Rabi frequency Ω_g and detuning Δ_g , excites the transition $|g\rangle \rightarrow |e\rangle$. This application of lasers results a Fano-like profile where the zero absorption case happens when both detunings of the lasers are the same $\Delta_r = \Delta_g$ (Fig. 5.2). We modify atom-field Hamiltonian from Eq. 4.9 to describe the three-level system of EIT. For simplicity, the wavevector and phase dependences are removed from Eq. 4.9 in this derivation². The atomic Hamiltonian and the atom-field Hamiltonian ($H_{EIT} = H_A + H_{AF}$) is

²Ref. [75] provides a full derivation of EIT.

denoted as:

$$H_{EIT} = \begin{pmatrix} -\omega_g & 0 & \frac{\Omega_g}{2} e^{i\omega_g t} \\ 0 & -\omega_r & \frac{\Omega_r}{2} e^{i\omega_r t} \\ \frac{\Omega_g}{2} e^{-i\omega_g t} & \frac{\Omega_r}{2} e^{-i\omega_r t} & 0 \end{pmatrix} \quad (5.4)$$

where $-\omega_g$ and $-\omega_r$ are the eigenvalues of the Hamiltonian in the absence of the coupling fields. Next, we apply unitary transformation $U(t)$ on $|\psi(t)\rangle$ to remove all time-dependence from H_{EIT} and obey the time-dependent Schrödinger equation $i\frac{\partial|\psi(t)\rangle}{\partial t} = H_{EIT}|\psi(t)\rangle$. The new basis is written as $|\tilde{\psi}(t)\rangle$ with $U(t)$ as:

$$U(t) = \begin{pmatrix} e^{-i\omega_g t} & 0 & 0 \\ 0 & e^{-i\omega_r t} & 0 \\ 0 & 0 & 1 \end{pmatrix} \quad (5.5)$$

Substitute both in the the time-dependent Schrödinger equation

$$\begin{aligned} H_{EIT}|\tilde{\psi}(t)\rangle &= i\frac{\partial|\tilde{\psi}(t)\rangle}{\partial t} \\ &= (i\frac{\partial\tilde{U}}{\partial t}\tilde{U}^\dagger + \tilde{U}H_{EIT}\tilde{U}^\dagger)|\tilde{\psi}(t)\rangle \end{aligned} \quad (5.6)$$

Therefore the time-independent EIT Hamiltonian is

$$\begin{aligned} H_{EIT} &= i\frac{\partial\tilde{U}}{\partial t}\tilde{U}^\dagger + \tilde{U}H_{EIT}\tilde{U}^\dagger \\ &= \begin{pmatrix} \Delta_g & 0 & \frac{\Omega_g}{2} \\ 0 & \Delta_r & \frac{\Omega_r}{2} \\ \frac{\Omega_g}{2} & \frac{\Omega_r}{2} & 0 \end{pmatrix} \end{aligned} \quad (5.7)$$

In order to find the population of each state, we need to solve the Master's equation

$$\frac{\partial\rho}{\partial t} = -i[H_{EIT}, \tilde{\rho}] + \mathbf{L}\tilde{\rho} \quad (5.8)$$

where

$$\tilde{\rho} = \left| \psi(\tilde{t}) \right\rangle \left\langle \psi(\tilde{t}) \right| \quad (5.9)$$

$$\mathbf{L}\tilde{\rho} = \sum_{j=g,r} (b_j \tilde{\rho} b_j^\dagger - [b_j^\dagger b_j, \tilde{\rho}]) \quad (5.10)$$

$\tilde{\rho}$ the density matrix and $\mathbf{L} = \Gamma_j |j\rangle\langle e|$ is the Lindblad operator to account the effect of spontaneous emission to $|g\rangle$ and $|r\rangle$ which are denoted as Γ_g and Γ_r respectively with Γ as the linewidth of $|e\rangle$ (Fig. 5.2 b). For steady-state solution, we take $\frac{\partial \rho}{\partial t} = 0$. The solution of excited state density matrix ρ_{ee} can be written as [67]:

$$\rho_{ee} = \frac{4(\Delta_g - \Delta_r)^2 \Gamma \Omega_r^2 \Omega_g^2}{\zeta} \quad (5.11)$$

$$\begin{aligned} \zeta = & ((\Delta_g - \Delta_r)^2 (8\Gamma \Omega_r^2 \Omega_g^2 + 4\Gamma^2 (\Gamma_g \Omega_r^2 + \Gamma_r \Omega_g^2) + 16(\Delta_r^2 \Omega_g^2 \Gamma_r + \Delta_g^2 \Omega_r^2 \Gamma_g)) \\ & + 8(\Delta_g - \Delta_r)(\Delta_r \Omega_g^4 \Gamma_r - \Delta_g \Omega_r^4 \Gamma_g) + (\Omega_g^2 + \Omega_r^2)^2 (\Omega_g^2 \Gamma_r + \Omega_r^2 \Gamma_g)) \end{aligned} \quad (5.12)$$

Another way to understand EIT is via dressed state [68, 76]. The pump beam applied to the Λ system causes AC stark shift of atomic levels, which leads to the creation of dressed states (Fig. 5.3³).

$$|+\rangle = \sin \theta |r\rangle + \cos \theta |e\rangle \quad (5.13)$$

$$|-\rangle = \cos \theta |r\rangle - \sin \theta |e\rangle \quad (5.14)$$

where θ is in the form

$$\tan \theta = \frac{\sqrt{\Delta_r^2 + \Omega^2} - \Delta_r}{\Omega_r} \quad (5.15)$$

The AC Stark effect shifts the energies of dressed states by:

$$\delta = \frac{1}{2} (\sqrt{\Omega_r^2 + \Delta_r^2} - |\Delta_r|) \quad (5.16)$$

³This figure is based on Ref. [76]

The probe beam couples the dressed state to $|g\rangle$. The application of both beams creates the Fano-like absorption spectrum (Fig. 5.3).

By setting $\Delta_r = \Delta_g = \Delta$, the energy eigenvalues of H_{EIT} are given by (Fig. 5.3 b):

$$E_D = \Delta \quad (5.17)$$

$$E_{\pm} = \Delta \pm |\delta| \quad (5.18)$$

During EIT cooling, the stationary atoms are trapped in the dark state $|D\rangle$, which comprises of mostly $|g\rangle$, irrespective of its initial state [73]. However, if the atoms are trapped in a harmonic oscillator with frequency ω_m and $\delta = \omega_m$, the motional modes of the atom can drive the population out from the $|D, n\rangle$ to the bright state $|+, n-1\rangle$ (Fig. 5.3c). Then, the population $|+, n-1\rangle$ spontaneously decays to $|D, n-1\rangle$. In the trapped-ion experiment, δ can be set to cool the COM transverse motional mode ω_{COM} most efficiently, and the other lower motional modes within a certain bandwidth can be cooled simultaneously. However, EIT cooling, unlike RSC, cannot deterministically prepare ions to their motional ground state as blue sideband excitation is still present. The steady-state average phonon number $\bar{n}(\Delta_g)$ of EIT cooling as a function of Δ_g [67] is given by:

$$\bar{n}(\Delta_g) = \frac{\rho_{ee}(\Delta_g) + \rho_{ee}(\Delta_g - \omega_m)}{\rho_{ee}(\Delta_g + \omega_m) - \rho_{ee}(\Delta_g - \omega_m)} \quad (5.19)$$

When the AC Stark shift $\delta = \omega_m$ and $\Delta_g = \Delta_r$

$$\bar{n} = \left(\frac{\Gamma}{4\Delta_r}\right)^2 \quad (5.20)$$

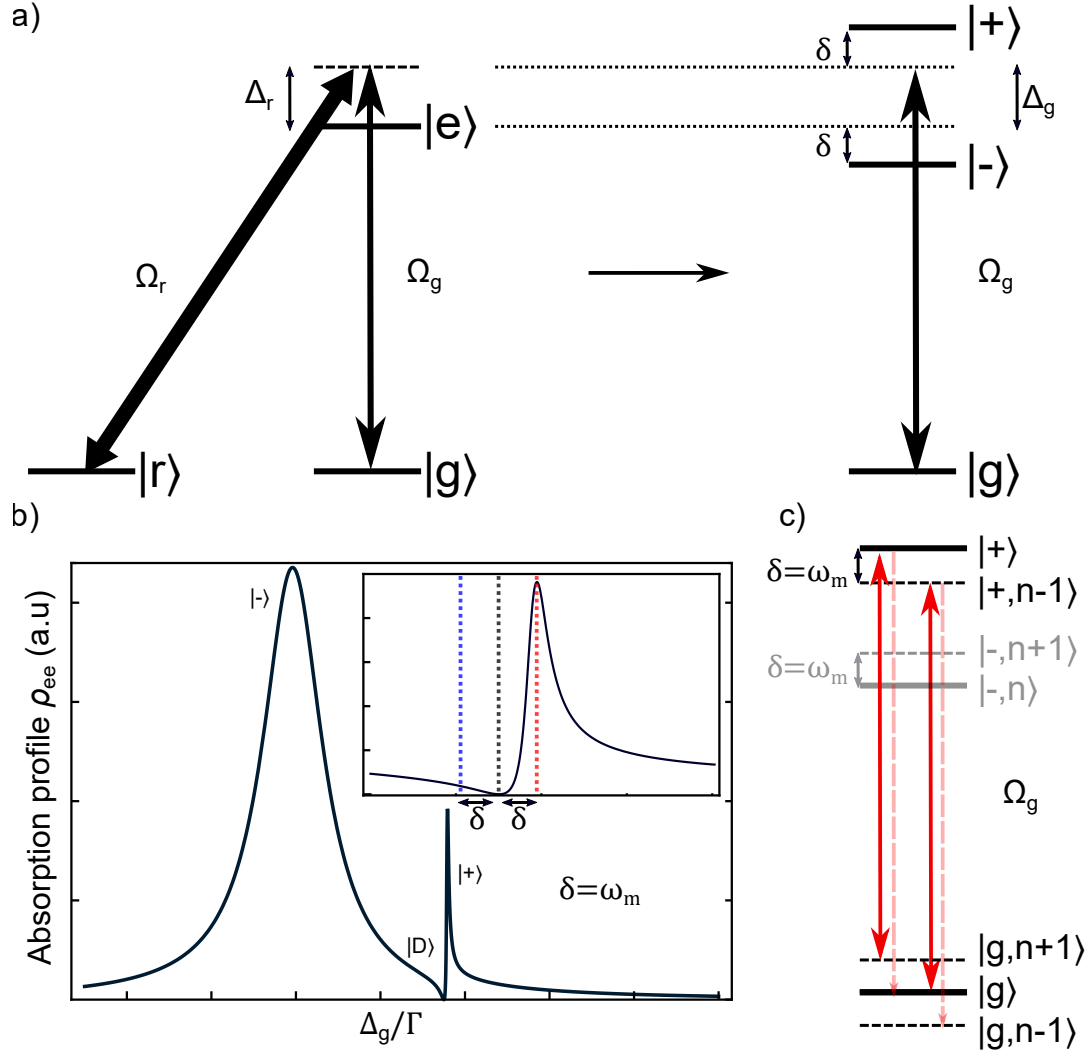


Figure 5.3: EIT cooling with Dressed State. a) Left: The Λ system in EIT cooling. The pump beam creates dressed states $|+\rangle$ and $|-\rangle$. Right: This shows the transformed dressed states ($|+\rangle$ and $|-\rangle$). The energies of the dressed state are AC Stark shifted by δ . The probe beam couples $|g\rangle$ to the dressed states. b) Absorption spectrum of ρ_{ee} . The maximum Lorentzian feature in ρ_{ee} at E_- indicates state $|-\rangle$. The dark state $|D\rangle$ (with E_D) is when $\rho_{ee} = 0$ while the bright state $|+\rangle$ (with E_+) is the maximum of Fano profile. Inset: Magnified image of the Fano profile. δ is tuned to be ω_m . The red dashed line indicates the red sideband transition, which is maximized for optimal EIT cooling mechanism with minimal blue sideband excitation (blue dashed line), while suppressing the carrier transition (black dashed line). c) The motion of the atom drive the sideband transition. EIT cooling works efficiently with $\delta = \omega_m$.

5.2.2 EIT Cooling in a Tripod System

The extension of EIT cooling beyond the three-level system has generated both studies in theoretical [77–79] and experimental [12, 80, 81] studies. This extension features EIT cooling with atom which its atomic structure has four or more atomic ground state, like $^{171}\text{Yb}^+$. Here, we demonstrate EIT cooling with a four-level tripod structure in $^{171}\text{Yb}^+$ [12]. The EIT cooling in $^{171}\text{Yb}^+$ featured here uses the transition between $^2S_{1/2} |F = 1\rangle \leftrightarrow ^2P_{1/2} |F' = 0\rangle \equiv |e\rangle$ (Fig. 5.4a) where linewidth of the excited state ($|e\rangle$) $\Gamma = 19.7$ MHz. The Zeeman states $|\pm 1\rangle \equiv |F = 1, m_F = \pm 1\rangle$ are Zeeman shifted by $\Delta_B = \pm 7.7$ MHz with respect to $|0\rangle \equiv |F = 1, m_F = 0\rangle$ by a constant magnetic field $B_{zee} = 5.5$ G along the y -axis. This EIT scheme involves a simultaneous and global application of two 369.5 nm lasers with all components of polarization (Fig. 5.4). The weak probe beam with π polarization is along the axial direction of the ion chain. The pump beam from the perpendicular direction of the ion chain has both σ^+ and σ^- polarizations where the ratio of both polarizations is controlled by a birefringent waveplate. With the methods shown in Eq. 5.5-5.7, the time-dependent part of the Hamiltonian of this tripod system can be eliminated and written as:

$$H = \begin{pmatrix} \Delta_{-1} & 0 & 0 & \frac{\Omega_{-1}}{2} \\ 0 & \Delta_0 & 0 & \frac{\Omega_0}{2} \\ 0 & 0 & \Delta_1 & \frac{\Omega_1}{2} \\ \frac{\Omega_{-1}}{2} & \frac{\Omega_0}{2} & \frac{\Omega_1}{2} & 0 \end{pmatrix} \quad (5.21)$$

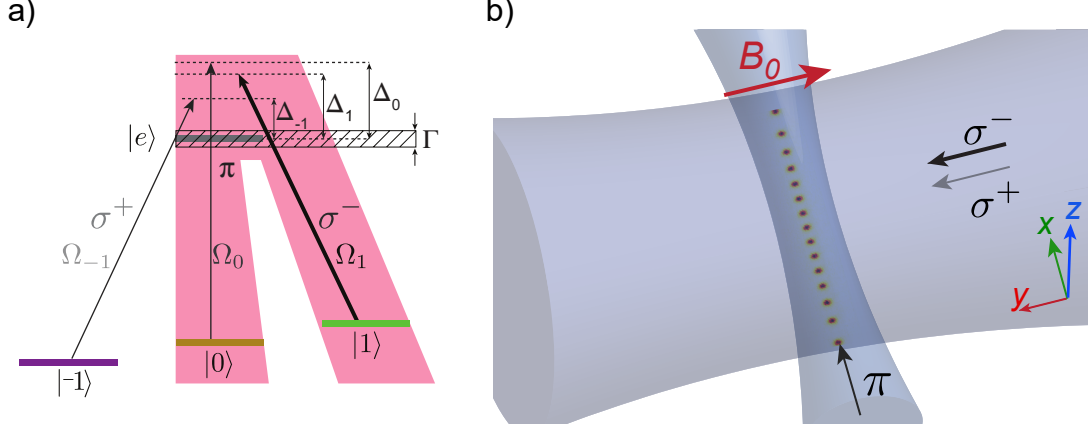


Figure 5.4: EIT cooling in $^{171}\text{Yb}^+$. a) Bare states of a four-level tripod structure in $^{171}\text{Yb}^+$ in EIT cooling. All the coupling lasers are shown with their respective detuning, Rabi frequencies and polarizations. The pink shading illustrates the effective EIT Λ system with π beam as the probe beam and σ^- beam as the pump beam. b) EIT cooling laser configuration in the lab. The σ^\pm pump propagating perpendicularly to the ion chain (y) and the π is along the chain axis (x).

where each ground state $|k\rangle$ couples to the excited state $|e\rangle$ via a dipole transition with its respective polarization, Rabi frequency Ω_k , detuning Δ_k from the $|e\rangle$. Here, we set $\Delta_0 = \Delta_1 = \Delta$ and $\Delta_{-1} = \Delta - 2\Delta_B$.

5.2.2.1 Simplification from four-level tripod system to effective Λ system

From the eigensystem of the four-level tripod, the dark state $|D\rangle$ comprises of both $|0\rangle$ and $|1\rangle$ with energy $E_D = \Delta$. The two additional bright eigenstates $|B_\pm\rangle$ consists of mostly $|e\rangle$ (Fig. 5.5a). Their corresponding energy eigenvalues are close to the two bright states energy eigenvalues in the Λ system (Eq. 5.18), $E_{B\pm} \approx \frac{1}{2}(\Delta \pm \sqrt{\Delta^2 + \Omega_0^2 + \Omega_1^2})$. The last remaining eigenstate $|\tilde{B}\rangle$, is another bright state where the majority of its state is $|-1\rangle$ with a relatively small percentage of the $|e\rangle$, $|0\rangle$ and $|1\rangle$. $|\tilde{B}\rangle$ can be approximated as being decoupled from both $|0\rangle$ and

$|1\rangle$ states. Therefore, the four-level tripod system can be simplified to an effective Λ system consisting just $|e\rangle$, $|0\rangle$ and $|1\rangle$ states (pink shading of Fig. 5.4a)⁴. In this simplification picture, σ^+ beam serves as a re-pumper to remove population from the $|-1\rangle$ state.

In this effective Λ system, the excited state population ρ_{ee} is given from Eq. 5.11-5.12:

$$\rho_{ee} = \frac{4\Delta^2\Gamma\Omega_1^2\Omega_0^2}{\zeta} \quad (5.22)$$

$$\begin{aligned} \zeta = & 8\Delta^2\Omega_1^2\Omega_0^2\Gamma + 2\Delta^2\Gamma^3\Omega^2 - 4\Delta_0\Delta\Omega_1^4\Gamma + \frac{1}{2}\Omega^6\Gamma \\ & + 8\Delta^2\Gamma(\Delta_1^2\Omega_0^2 + \Delta_0^2\Omega_1^2) + 4\Delta_1\Delta\Omega_0^2\Gamma \end{aligned} \quad (5.23)$$

with $\Delta = \Delta_0 - \Delta_1$. Here, $\Gamma_r = \Gamma_g$ from Eq. 5.12 is $\Gamma_0 = \Gamma_1 = \frac{1}{2}\Gamma$ because we have σ^+ acts a re-pumper and the spontaneous decay to both $|0\rangle$ and $|1\rangle$ state equally. With the assumption that $\Delta_1 \approx \Delta_0$ and $\Omega_0 \ll (\Omega_1, \Delta_1)$, the excited state is simplified to:

$$\rho_{ee}(\Delta) \approx \frac{\Delta^2\Omega_0^2}{\Delta^2\Gamma^2 + 4(\Omega_1^2/4 - \Delta\Delta_0)^2} \quad (5.24)$$

For sanity check, the minimum of ρ_{ee} is at $\Delta = 0$, which corresponds to the dark state, and the nearest maximum appears at $\Delta = \frac{1}{2}(\sqrt{\Delta_1^2 + \Omega_1^2} + \Delta_1)$, which is the bright state. The cooling bandwidth is estimated by finding at which detuning Δ_0 where the cooling stops. This condition happens when the blue sideband absorption spectrum is higher than the red sideband absorption spectrum, $\rho_{ee} \leq \rho_{ee}(\Delta) -$

⁴This effective Λ system provides an intuitive picture with the above Δ_i and Ω_i parameters. Solving the four-level tripod eigensystem and Master's equation will give a more comprehensive solution, which can be done in Mathematica, Matlab, Python, etc.

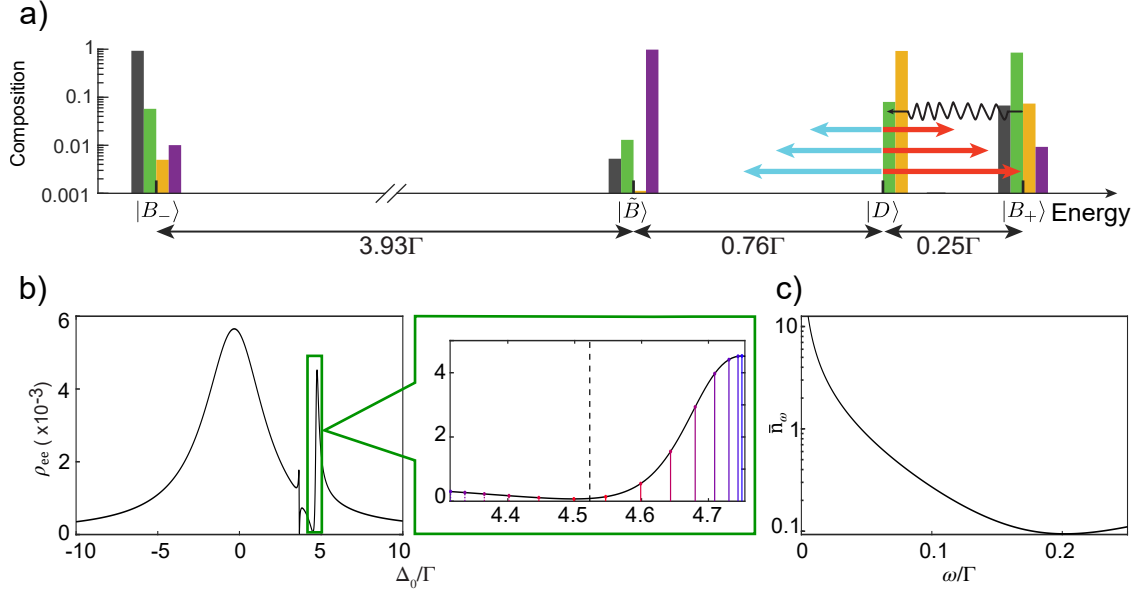


Figure 5.5: Numerical calculation of the four-level tripod system of $^{171}\text{Yb}^+$ for EIT cooling with Rabi frequencies $\Omega_{-1} = 0.7\Gamma$, $\Omega_0 = 0.35\Gamma$, $\Omega_1 = 2.0\Gamma$ and detunings $\Delta_{-1} = 3.69\Gamma$, $\Delta_0 = \Delta_1 = 4.47\Gamma$. a) The eigenstate decomposition in the dressed-state in terms of the bare states, indicated by the color bars ($|e\rangle$: gray, $|-1\rangle$: purple, $|0\rangle$: orange, $|1\rangle$: green). The red (blue) arrow indicates red (blue) sideband transitions. The black wavy arrow represents spontaneous decay. b) Absorption spectrum of the excited state ρ_{ee} as a function of the probe laser detuning Δ_0 , calculated by numerically solving the steady-state Master's equation. The green box shows the magnified view focusing on the Fano profile for EIT cooling. The gray dashed line shows the experimental probe frequency during EIT cooling. A few examples of experimental transverse modes are marked with colored lines increasing from red to blue. c) The calculated steady-state average phonon number \bar{n}_{ω_m} .

$\rho_{ee}(-\Delta)$. This the cooling bandwidth is given by:

$$\begin{aligned}
 W_C &\approx \frac{1}{2}[2(1 + \sqrt{2})\Delta_1 + \sqrt{\Delta_1^2 + \Omega_1^2} - \sqrt{(3 + 2\sqrt{2}\Delta_1^2 + \Omega_1^2)}] \\
 &\approx \frac{1 + \sqrt{2}}{3/2 + \sqrt{2}\Delta_1} \frac{\Omega_1^2}{\Delta_1}
 \end{aligned} \tag{5.25}$$

5.2.2.2 Four-level tripod numerical result

Similar to the explanation of the previous section, the steady-state population is trapped in the dark state when EIT cooling beams are applied to the stationary

atom. With the motional modes of the atoms, the population can be driven out from the $|D\rangle$. In this tripod system, we set $E_{B_+} - E_D = \omega_m$ to drive the state from $|D, n\rangle \rightarrow |B_+, n-1\rangle$. Then, the population in $|B_+, n-1\rangle$ decays to $|D, n-1\rangle$. This cycle continues until it reaches to steady-state average phonon of the m th motional mode ω_m [67, 79]:

$$\bar{n}_{\omega_m} = \frac{\rho_{ee}(\Delta_0) + \rho_{ee}(\Delta_0 - \omega_m)}{\rho_{ee}(\Delta_0 + \omega_m) - \rho_{ee}(\Delta_0 - \omega_m)} \quad (5.26)$$

where $\rho_{ee}(\Delta_0)$ and $\rho_{ee}(\Delta_0 \pm \omega_m)$ are the numerical steady-state population of the excited state $|e\rangle$ at the carrier and sidebands respectively (Fig. 5.4). With this calculation, we can tune the experimental parameters (Ω_i and Δ_i) to achieve the lowest cooling limit with a wide motional modes bandwidth.

From the four-level tripod configuration, we calculate the absorption spectrum with the steady-state solution of the master equation with the four-level EIT Hamiltonian (Eq. 5.8-5.9)

$$\frac{\partial \rho}{\partial t} = -i[H, \rho] + \mathbf{L}\rho \quad (5.27)$$

$$\mathbf{L}\rho = \sum_{j=-1}^1 (b_j \rho b_j^\dagger - [b_j^\dagger b_j, \rho]) \quad (5.28)$$

$$b_j = \sqrt{\Gamma/3} |j\rangle\langle e| \quad (5.29)$$

The numerical study is depicted in Fig. 5.6.

5.2.2.3 Four-level tripod experimental result

In this work, we employ the cryogenic trapped-ion setup discussed in this thesis [11]. The ions are confined in a linear RF trap with two transverse COM frequencies $\omega_\alpha = 2\pi \times 4.45$ MHz and $\omega_\beta = 2\pi \times 4.30$ MHz with axial frequency

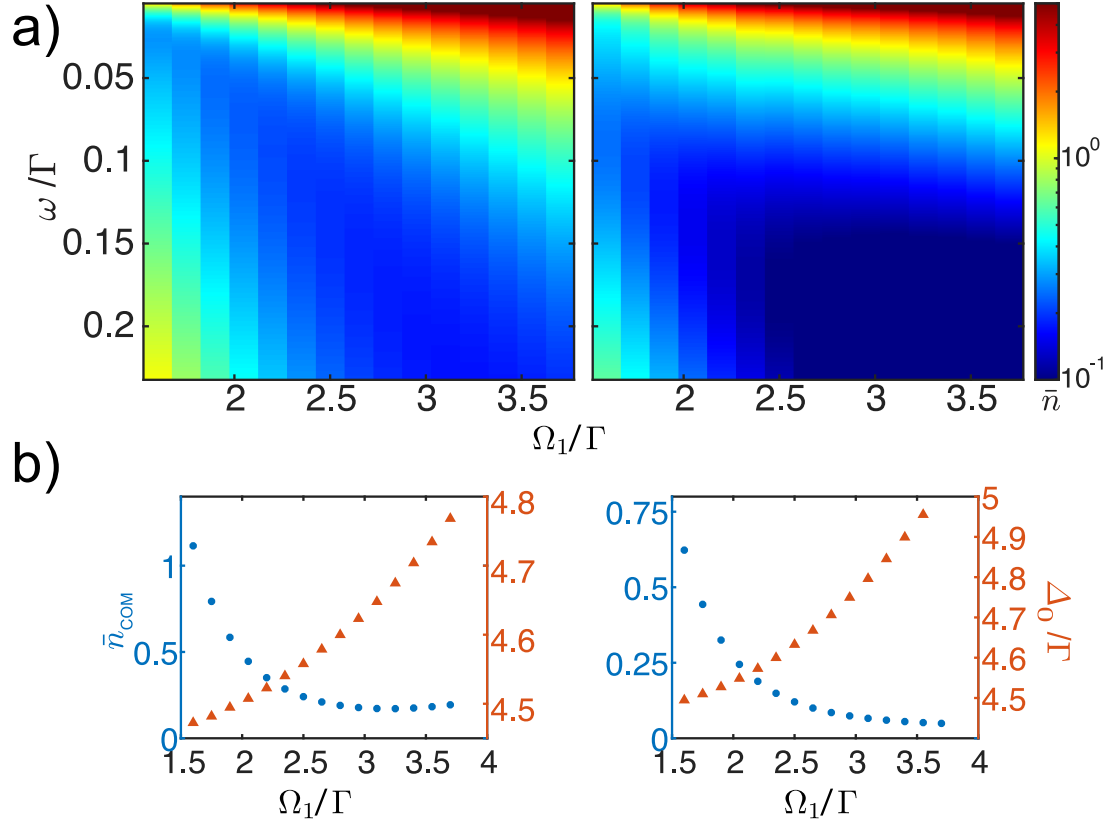


Figure 5.6: Numerical result of average phonon number with EIT cooling. a) The heat map plot shows the average phonon number (color map) as a function of mode frequency and Rabi frequency of the pump beam. The detuning of the pump beam is set to $\Delta_1 = 4.47\Gamma$. Left: the detuning of the σ^+ beam is set to $\Delta_{-1} = 3.69\Gamma$ and the Rabi frequency is $\Omega_{-1} = 0.35\Omega_1$. Right: the detuning of the σ^+ beam is set to $\Delta_{-1} = -4.47\Gamma$ and the Rabi frequency is $\Omega_{-1} = \Omega_1$. b) The optimal detuning Δ_0 and the corresponding average phonon number for the COM motional mode.

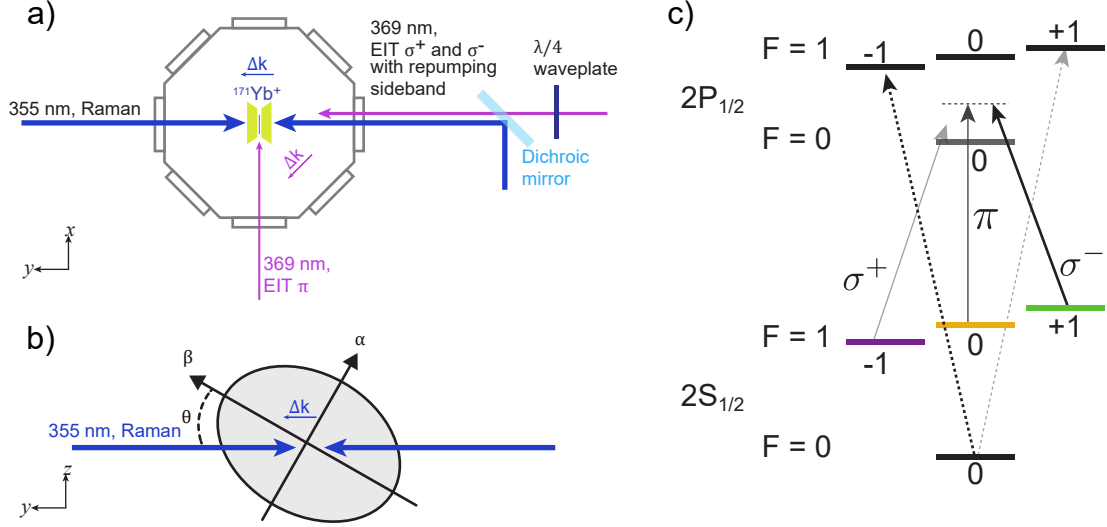


Figure 5.7: EIT laser configuration in the experiment. a) The σ^\pm beams combine with one of Raman beams with a dichroic mirror. The EIT wavevector difference couple to both principal axes of the trap. Therefore, EIT cooling can cool both sets of transverse modes. b) The counter-propagating Raman beams have wavevector difference perpendicular to the ion chain axis, which also couple to both principal axes of the trap. The Raman beams are tilted by θ with respect to principal axes β , which enables sideband spectroscopy on the transverse modes. Axis α is perpendicular to axis β . In this experiment, $\theta = 40^\circ$. c) The level diagram of $^{171}\text{Yb}^+$ with states in $2S_{1/2}$ and $2P_{1/2}$. The second order of 7.34 GHz EOM is used to modulate the pump beam (dashed arrow lines) for removing the population from the $2S_{1/2} |F=0\rangle$ state. The light gray line indicates a weaker σ^+ re-pumped beam than σ^- .

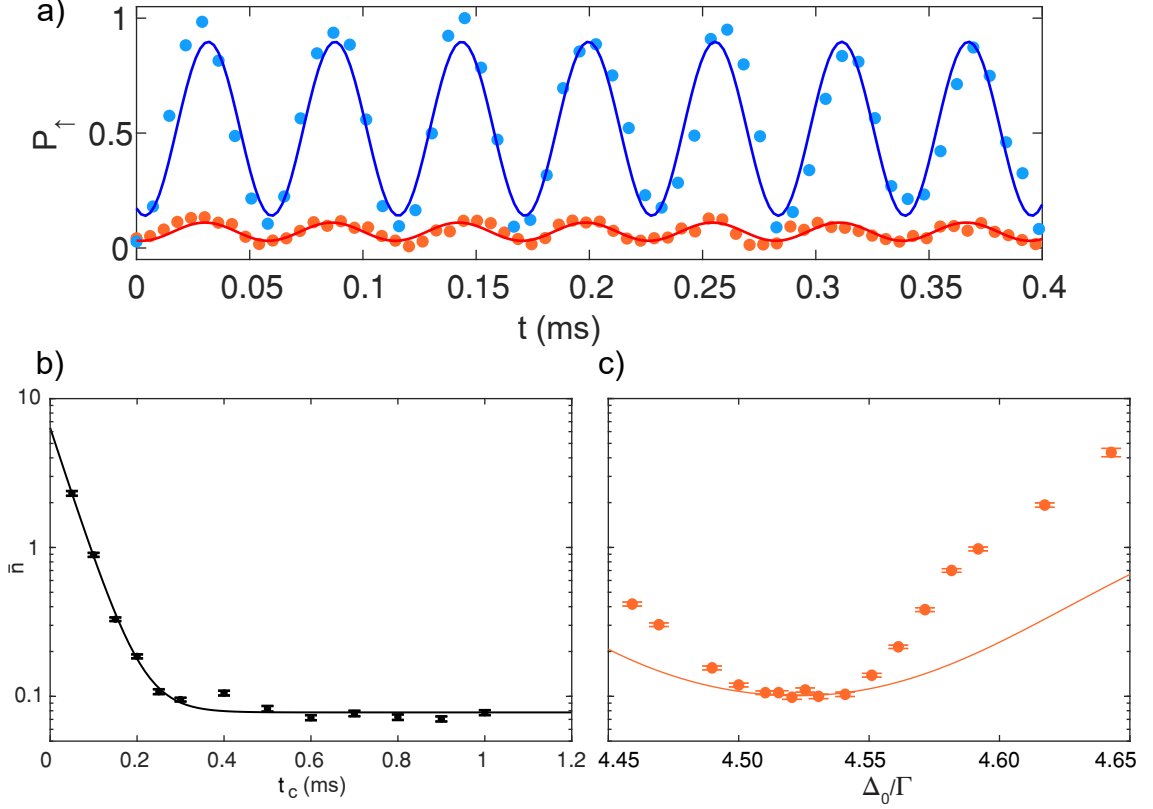


Figure 5.8: EIT cooling performance of a single ion. a) Bright state population P_{\uparrow} of the red (blue) sideband Rabi flopping between the qubit states, (depicted as red (blue) experimental dots and fitted line from the data). $R_{\omega_m}(t)$ is obtained by comparing the ratio red and blue Rabi flopping population at time t to extract \bar{n}_{COM} . b) Measured \bar{n}_{COM} (black dots) as a function of EIT cooling time t_c for the COM transverse mode at $2\pi \times 4.45$ MHz. The data is fitted to an exponential decay with an offset to extract the $1/e$ cooling time. c) Measured \bar{n}_{COM} (orange dots) as a function of Δ_0 . The orange line indicates the numerical solved Master's equation. Both plots use the same experimental parameters: $\Omega_1 = 2.0\Gamma$, $\Omega_0 = 0.76\Gamma$, $\Omega_{-1} = 0.8\Gamma$, $\Delta_1 = 4.5\Gamma$, $\Delta_0 = 4.54\Gamma$ and $\Delta_{-1} = 3.69\Gamma$. There is a good qualitative agreement between the numerics and experiment and good quantitative agreement near the EIT dark resonance where we operate in the experiment.

$\omega_{ax} = 2\pi \times (0.29 - 0.39)$ MHz, depending on the number of ions. Both transverse modes are cooled as the wavevector difference of the EIT beams overlaps with the principal axes of the trap (Fig. 5.7). We also added a 14.7 GHz sideband on the σ^\pm beam to pump all the population out from the $|\downarrow_z\rangle$ state. We start the experiment with Doppler cooling \rightarrow ground-state cooling \rightarrow optical pumping (initialize qubit to \downarrow_z). Then, we measure the vibration population of the transverse modes using a pair of counter-propagating 355 nm Raman laser to perform sideband spectroscopy. We compare the ratio of the red and blue sidebands $R_{\omega_m} = \frac{P_{\uparrow}^{red}(t)}{P_{\uparrow}^{blue}(t)}$ (Fig. 5.8a) to extract $\bar{n}_{\omega_m} = \frac{R_{\omega_m}}{1-R_{\omega_m}}$ [67].

We start the EIT cooling with a single $^{171}\text{Yb}^+$ ion with the optimized Rabi frequencies and detunings of both the pump and probe beam. To further optimize the EIT cooling, we vary Δ_0 of the probe beam and measure the phonon number in the COM mode for each configuration. The measured optimal thermal phonon number agrees with the numerical result but deviates as Δ_0 are tuned away from the optimal thermal phonon number. We attribute this to imperfect σ^\pm polarizations due to the dichroic mirror. We also measure the steady-state phonon number with various cooling times t_C to extract a $1/e$ cooling of 48 μs . We achieve $\bar{n}_{\omega_{COM}} = 0.08$ with a cooling rate of 8.4×10^4 quanta/s (Fig. 5.8).

Next, we perform EIT cooling on longer ion chains with length $N = 5, 15, 23, 40$ (Fig. 5.9 a-d) using the same experimental parameters in the single ion case. \bar{n}_{ω_m} is obtained by comparing the corresponding red and blue sidebands peaks of an ω_m . We apply a fixed EIT cooling time of $t_c = 300\mu s$ for all system size and observe a stronger suppression of the red sideband than the blue sideband. This indicates

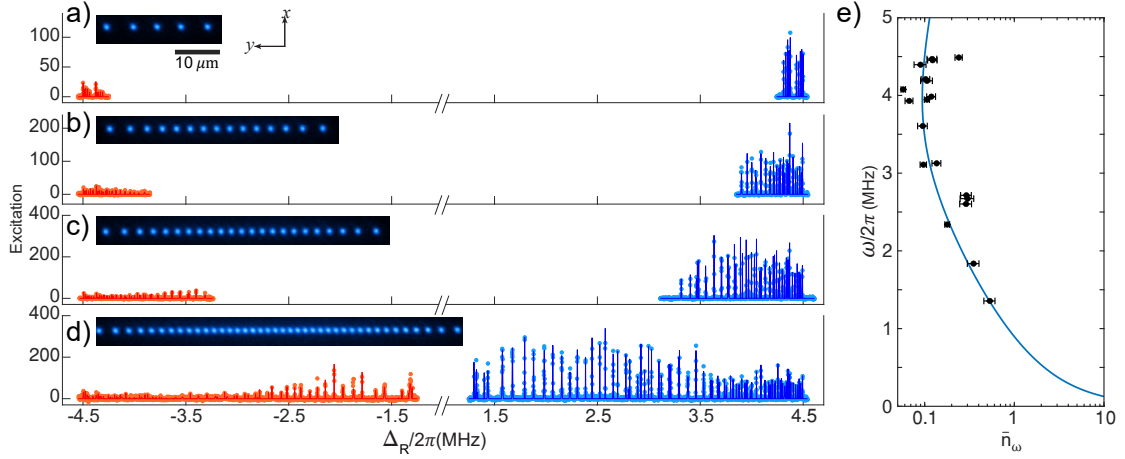


Figure 5.9: Long ion chain EIT cooling performance. a-d) The red and blue motional sideband spectra of ion chains with length $N = 5, 15, 23,$ and 40 ions as shown as in the inset. The horizontal axis is the detuning from the carrier transition Δ_R . The COM motional modes do not change, and two more transverse frequency with each additional ion. The asymmetry of the red and blue sideband excitation indicates a large cooling bandwidth of ≈ 3 MHz. The experimental data (dots) are Gaussian fitted (solid color lines) to identify the peaks. e) The extracted steady-state phonon number of selected transverse modes across the 40-ion chain. The dots represent experimental data with the solid blue line as the numerical prediction with the same experimental parameters.

an efficient EIT cooling of transverse motional modes. We observe \bar{n}_{ω_m} as low as 0.04 ± 0.01 for specific modes and $\bar{n}_{\omega_m} < 0.54$ within the 3 MHz bandwidth (Fig. 5.9 e). Thus, we have achieved an efficient and wide bandwidth EIT cooling of the transverse motional modes with fixed EIT cooling time, independent of the number of ions. As a comparison to show that EIT cooling is working, we took the red and blue sidebands of the 31 ions where the ions are only Doppler cooled (Fig. 5.10).

Finally, we investigate the cooling performance of EIT cooling with RSC of selected modes in a chain of 36 ions using motion-sensitive carrier Rabi flopping. As we scale up the system size, the transverse mode spectrum becomes dense, and driving sideband Rabi oscillation becomes challenging. An alternative method for cooling

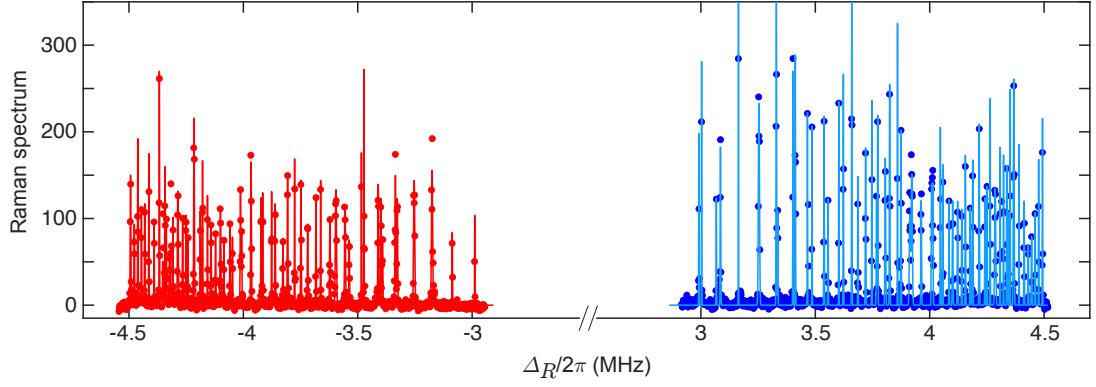


Figure 5.10: The red (in red) and blue (in blue) Raman sideband spectra of 31-ions chain after 2 ms of Doppler cooling. The dots indicate experimental data and solid lines are Gaussian fits to guide the eye. The motional modes for the chain have a bandwidth of 1.5 MHz. The peak heights of the red sidebands after Doppler cooling can be contrasted with that of Fig. 5.9 (a-d) after EIT cooling, to illustrate that EIT cooling works better than Doppler cooling over a large bandwidth.

performance is to use counter-propagating Raman beams to drive the motion of the ions. It gives a global measurement total average phonon number of the motional modes. The direct effect of the phonon number is through the Debye-Waller effect on the carrier Rabi frequency on the i ion that suppresses the interaction. Assuming each motional mode m is in the thermal state with average phonon number \bar{n}_m , the carrier Rabi frequency on the i ion is:

$$\bar{\Omega}_i = \Omega_i \exp \left[- \sum_m \eta_{im}^2 (\bar{n}_m + 1/2) \right] \quad (5.30)$$

where each mode is within the Lamb-Dicke regime $\eta_{im}^2 (\bar{n}_m + 1/2) \ll 1$ [67]. The Rabi flopping of the i th ion with the initial state $|\downarrow_z^{(i)}\rangle$ is given by:

$$P_{\uparrow}^{(i)}(t) = \frac{1 - C_i(t) \cos(\bar{\Omega}_i t - \phi)}{2} \quad (5.31)$$

where the phase $\phi \ll 1$. The contrast of the $P_{\uparrow}^{(i)}(t)$

$$C_i(t) = \Pi_m \frac{1}{\sqrt{1 + (\eta_{im}^2 \bar{n}_m \bar{\Omega}_i t)^2}} \approx 1 - \frac{1}{2} (\bar{\Omega}_i t)^2 \sum_m \eta_{im}^4 \bar{n}_m^2 \quad (5.32)$$

where the approximation assumes sufficiently early evolution times. Here, the $C_i(t)$ suppresses both the Rabi frequency and contrast of the Rabi flopping. Unlike the sideband spectroscopy, this method does not extract the individual \bar{n}_{ω_m} . However, with the measured Rabi evolution of each ion, we can extract global information about the thermal motion of the ions. We fit the observed Rabi flopping of each ion in the chain to Eq. 5.31 to the following function:

$$P_{\uparrow}^{(i)}(t) = \frac{1 - [1 - A(B_i t)^2] \cos B_i t}{2} + P_0 \quad (5.33)$$

where $A = \frac{1}{2} \sum_m \eta_{im}^4 \bar{n}_m^2$ and B_i as the Rabi frequencies for each ion. P_0 is an offset term to account for detection errors.

With these global observables, we gauge three different cooling schemes. Method 1 is the control that implements only RSC centered on the two COM modes, which cool the COM and the neighboring modes. Method 2 applies four additional modes that are further away from the COM to cover the full motional spectrum of the 36 ions, ensuring all the modes are ground-state cooled. Method 3 combines broadband EIT cooling with Method 1. Overall, both Methods 2 and 3 have shown improvement on the Rabi flopping than Method 1. However, Method 2 costs twice as much time as Method 3 to achieve similar performances⁵. The data here assumes that laser intensity noise is not the main factor in decreasing the Rabi oscillation contrast. The main objective here is to observe the relative improvement of the above cooling schemes under similar experimental conditions. The comprehensive treatment will use co-propagating Raman beams to isolate the motion contribution

⁵Here, the laser power of RSC is limited. The RSC time can be reduced with higher laser power. However, when the laser power is unlimited, the carrier transition of the qubit would be driven, resulting in inefficient RSC.

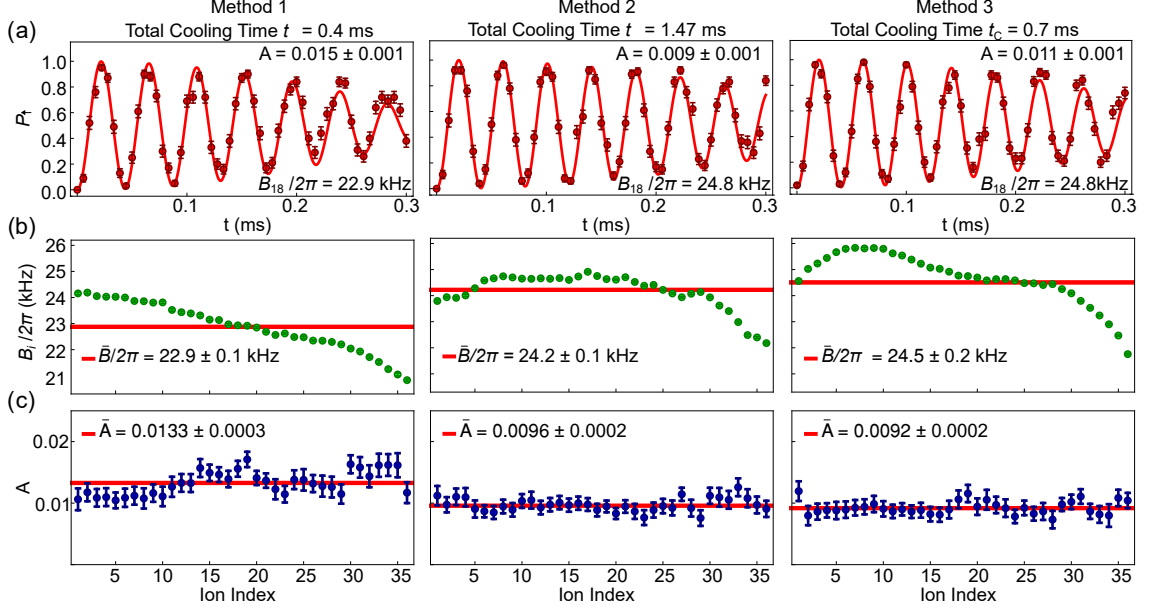


Figure 5.11: The performance of three different cooling schemes with a 36 ion chain characterized with a motion-sensitive carrier Rabi oscillations. The transverse modes here are spread between 2-4.45 MHz. The Doppler cooling time is neglected. a) The Rabi flopping of the 18th ion. The red lines show the fitted result with Eq. 5.33. The measured best-fit parameter the Rabi frequencies B_i b) and A . c) with Eq. The red horizontal lines represent the average of B and A across the ion chain. Each column shows the result from three different ground-state cooling schemes. Left: 40 cycles of RSC on each of the COM motional modes at 4.4 MHz and 4.35 MHz with a total cooling time $t = 0.4$ ms. Middle: Another four additional 40 cycles RSC for each of the frequencies at 3.57 MHz, 3.25 MHz, 2.43 MHz, and 2.07 MHz with $t = 1.47$ ms. Right: Combination of 0.3 ms EIT cooling time with Method 1 RSC cooling with a total cooling time of 0.7 ms. The asymmetry of the Rabi frequency (b) is likely from the uneven micromotion across the chain with length of $\approx 76 \mu\text{m}$.

from the laser noise to obtain the decay due to laser intensity noise.

5.2.2.4 EIT calibration and qualitative discrepancy in numerical and experimental data

The EIT cooling parameters are first calibrated before data taking. The detuning Δ_i with $i = -1, 0, 1$ can be easily set with the RF frequency generated by the DDS to the AOMs. The Rabi frequencies Ω_i are calibrated with Ramsey spectroscopy. We first calibrate the microwave driving frequency with the energy splittings between $^2S_{1/2} |F = 0\rangle (|\downarrow_z\rangle)$ and $^2S_{1/2} |F' = 1\rangle$, which consists of $|i\rangle$ with $i = -1, 0, 1$. We roughly find the hyperfine ($|\downarrow_z\rangle \leftrightarrow |0\rangle$) and Zeeman transitions ($|\downarrow_z\rangle \leftrightarrow |\pm 1\rangle$) by scanning the microwave frequency with their respective fixed time as the Rabi frequencies of these transitions are different⁶. To fine-tune the microwave driving frequency, we do a Ramsey scan ($\pi/2 \rightarrow$ scan the wait time $\rightarrow \pi/2$) and change the microwave drive and then $\pi/2$ time till we achieve a flat line. For each EIT beam calibration, we apply a calibrated microwave $\pi/2$ pulse to prepare the ion in the superposition state of the $|\downarrow_z\rangle$ and the respective $^2S_{1/2} |F' = 1\rangle$ states. Next, we shine each of the EIT beams separately on the atom and scan the individual EIT beam pulse time. Finally, we apply another $\pi/2$ microwave pulse before measuring. From this, we can obtain the AC stark shift for each polarization for each EIT beam from the Ramsey oscillation (Fig. 5.12), which is approximately given by:

$$\delta_{AC}^{(i)} = \frac{\Omega_i^2}{(4\Delta_i)} \quad (5.34)$$

⁶This depends on the orientation of the microwave with respect to the B -field. The microwave horn placement is approximately diagonal with respect to the B -field here.

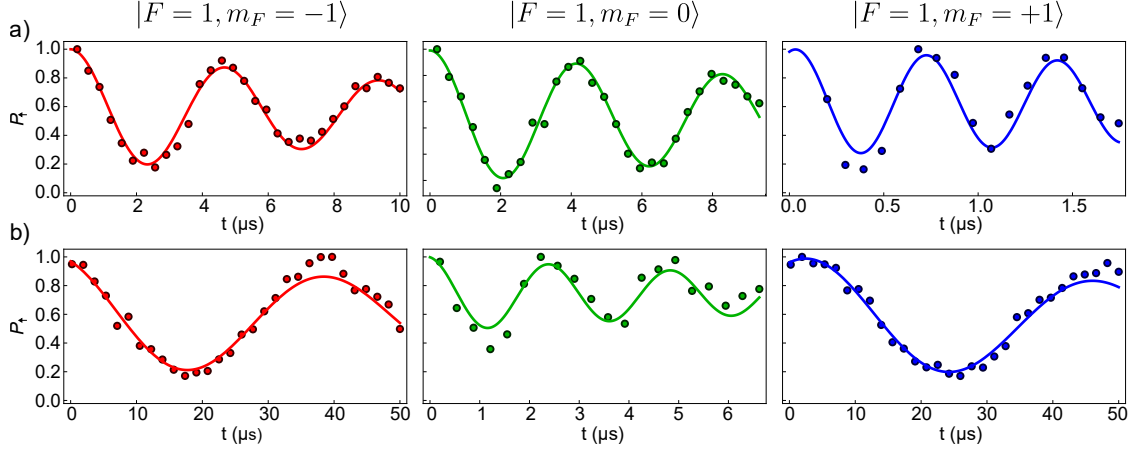


Figure 5.12: Ramsey measurement for calibrating EIT cooling beams. Left: Ramsey measurement between $^2S_{1/2} |F=0, m_F=0\rangle \leftrightarrow ^2S_{1/2} |F=1, m_F=-1\rangle$. Middle: Ramsey measurement between $^2S_{1/2} |F=0, m_F=0\rangle \leftrightarrow ^2S_{1/2} |F=1, m_F=0\rangle$. Right: Ramsey measurement between $^2S_{1/2} |F=0, m_F=0\rangle \leftrightarrow ^2S_{1/2} |F=1, m_F=1\rangle$. a) Ramsey fringes of EIT pump beam. b) Ramsey fringes of EIT probe beam.

From this measured AC stark shift, we extract the Rabi frequencies of all the EIT beams with all the polarization components:

$$\begin{aligned} \text{Pump beam (pm)} : (\Omega_1^{pm}, \Omega_0^{pm}, \Omega_{-1}^{pm}) &= (2.0\Gamma, 0.8\Gamma, 0.8\Gamma) \\ \text{Prob beam (pm)} : (\Omega_1^{pr}, \Omega_0^{pr}, \Omega_{-1}^{pr}) &= (0.17\Gamma, 0.76\Gamma, 0.18\Gamma) \end{aligned}$$

The EIT cooling parameters need $\Omega_1 = \Omega_1^{pm}, \Omega_0 = \Omega_0^{pr}, \Omega_{-1} = \Omega_{-1}^{pm}$. The rest are imperfect polarizations.

We test EIT cooling on the highest COM mode ω_α with a single ion with all the parameters calibrated. Then, we proceed for longer ion chain using the same parameters. In the experiment, we start with 2 ms Doppler cooling which reduces the $\omega_{\alpha_{COM}}$ to $\bar{n} \approx 5$, then follow by EIT cooling for 300 μs and finally measure the \bar{n} .

We attribute the discrepancy between the experimental data with the numer-

ical result in Fig. 5.8 to the imperfect polarization of the laser beams. First, this effect can lead to biases in the AC Stark shift calibration of the Rabi frequencies used in the numerical calculation. In addition, this can give rise to spurious bright resonance which its absorption profile can cause heating. We investigate the effect of the impure π component of the pump beam and σ^+ component of the probe beam. We notice that impure beam polarization has the same EIT dark resonance as the ideal polarization scheme, which suppresses the carrier scattering at the optimal EIT cooling condition. However, once the probe beam moves away from the EIT dark resonance, the carrier suppression in the impure polarization scheme has diminished as the bright resonance of the impure scheme is very close to its dark resonance. This carrier scattering results in inefficient EIT cooling or ‘EIT heating’.

Furthermore, the theoretical model does not consider all of the states in the $^2S_{1/2} \leftrightarrow ^2P_{1/2}$ transition. In the experiment, we also have EOM to modulate the σ^\pm beam with an EOM to remove the population from the $|\downarrow_z\rangle$ state. Lastly, the numerical model does not consider the interaction between ions when cooling a long ion chain. This may complicate the cooling process [82].

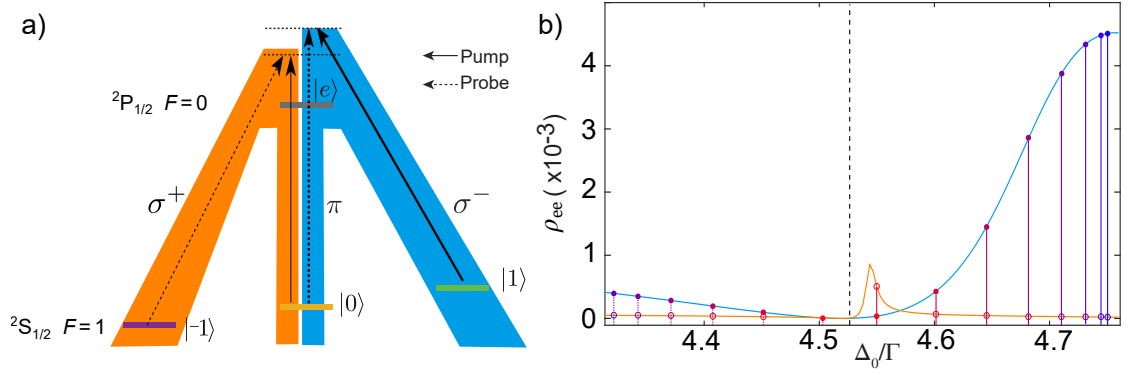


Figure 5.13: Coupling from polarization impurity. a) Blue shows the main EIT cooling scheme driven by the major σ^- component of the pump beam and the major π component of the probe beam. However, the experiment beams are imperfect. Here, we include the small π component of the pump beam and the small σ^+ component of the probe beam (orange). (b) The EIT absorption profile around the cooling window is calculated by only considering the blue or orange configuration separately from the experiment calibration. The black dashed line marks the probe frequency during cooling. The red to blue lines denote several examples of transverse mode frequencies with their value increasing as the color continuously changes from red to blue. Dashed (solid) lines indicate blue (red) sidebands. The dots (circles) indicate the value of ρ_{ee} at the corresponding sideband frequencies for the major (minor) configuration.

Chapter 6: Analog Quantum Simulation

In Chapter 4, we have provided a toolbox for quantum simulations. Although such a quantum simulator is not a universal quantum computer [83, 84], it can be tailored to study particular quantum models such as TFIM. In this lab, we have explored this quantum simulator for optimization [85] and many-body physics [13, 86]. This thesis focuses on the quantum simulation experiment – “Domain-Wall Confinement and Dynamics in a Quantum Simulator” [13]. Here, we study the effect of confinement with its implications on information spreading in many-body system and excitation energy of domain-wall bound states from non-equilibrium quench dynamics.

6.1 Information propagation

The propagation velocity of quantum information can be measured by observing how fast different parts of the system becomes correlated [87, 88]. Thus, it is interesting to study quantum many-body systems to understand how quantum information propagation is influenced when different interactions are engineered in the system for quantum computing [89], quantum simulation [90], and quantum metrology [91] purposes. Systems with power-law interactions, where the interaction strength falls off according to $r^{-\alpha}$ with distance r and $\alpha > 0$, are studied for

their rich physics. One prominent examples of such an interaction is the short-range interaction where $\alpha > 3$. In the short-range model, the velocity spreading is bounded such that it exhibits a linear light cone correlation spreading [92]. This is called the Lieb-Robinson bound, which furthers the understanding of local interacting quantum many-body system [93]. This similar study has been extended to understand quantum information and entanglement spreading in the long-range model [94]¹.

In the experiment, we perform a quantum quench and observe the implications of confinement in the spreading of correlations. As explained in Chapter 4, we apply a quantum quench and measure individual spins, which enables us to calculate the magnetization and many-body correlations. We use the two-body correlator to calculate the connected correlations:

$$C_{ij}^{\zeta}(t) = \langle \sigma_i^{\zeta}(t) \sigma_j^{\zeta}(t) \rangle - \langle \sigma_i^{\zeta}(t) \rangle \langle \sigma_j^{\zeta}(t) \rangle. \quad (6.1)$$

where $C_{ij}^{\zeta}(t)$ measures the correlation between spins i and j along the axis $\zeta = x, y, z$. The first term in Eq. 6.1 is a two-body correlator, and the second term is a normalization offset to ensure that an uncorrelated measurement equals zero. Therefore, $C_{i,j}^x(t) = 0$ for uncorrelated spins, $C_{i,j}^x(t) = 1$ for correlated spins and $C_{i,j}^x(t) = -1$ for anti-correlated spins.

6.2 Confinement model

Confinement is a ubiquitous mechanism. Particles subject to confinement experience an attractive potential that increases without bound as they separate.

¹This reference is one of the examples in this field.

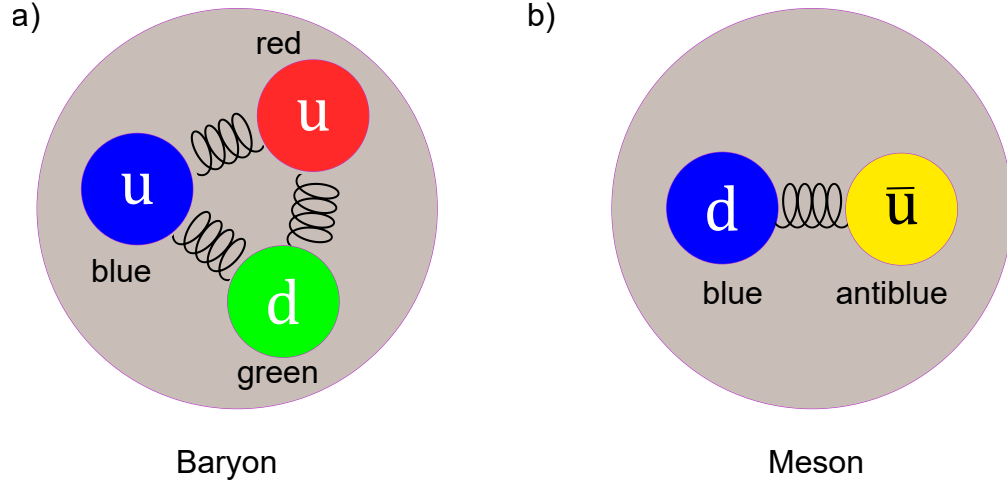


Figure 6.1: Hadronic particles. A hadron can be categorized into two categories a) baryon (made up of an odd number of quarks with ≥ 3 quarks) or a b) meson (made up of a quark and antiquark). Gluons (spring lines) bind the quark together, forming hadronic particles. Gluons carry color charge of the strong interaction, and they interact with themselves and the quarks. For physical particles to exist, the combination of quarks needs to have a net color-neutral charge. This property is called color confinement. For example, the three quarks in the baryon particle a), each have three different colors (red, blue, and green) charge to form a color-neutral charge. It also can be in the form of superpositions where each term consist of three colors. Meson b), on the other hand, has a quark with one of the primary colors and antiquark with anticolor of the quark's color to obtain net zero color charge. The superposition for the color charge can be in the form of color with its anticolor for each term. The quantum simulation experiment here explores the concept of confinement that is analogous to meson.

One prominent example of confinement is color confinement in quantum chromodynamics (QCD), where quarks are confined into hadronic particles by the strong interaction that increases with the particles' separation [95, 96]. The concept of confinement is well-established, but a quantitative understanding of the connection between theoretical prediction and experimental observation remains an active area of research [95, 96]. The study of confinement can be extended to the context of condensed matter and statistical physics, where it can occur in a low-energy quantum many-body system, which can provide insight into confinement from the microscope perspective. In previous works, the static and equilibrium of such confined system have been well studied both theoretically and experimentally. However, as shown in recent theoretical studies, the effect of confinement can also have dramatic consequences for non-equilibrium dynamics in a quantum many-body system, such as suppression of information spreading and slow thermalization [97–104].

6.2.1 Analogy of confinement in with the Ising model

This analogous effect of confinement occurs in the 1D nearest-neighbor short-range Ising model with both transverse and longitudinal B -fields, in which the out-of-equilibrium dynamics can be used to quantify confinement [97]. In this theoretical study, the Hamiltonian is given by:

$$H = -J \sum_{-\infty}^{\infty} [\sigma_i^x \sigma_{i+1}^x + B_z \sigma_i^z + B_x \sigma_i^x] \quad (6.2)$$

For $B_x = 0$, the domain-walls (regions with spins that are anti-aligned with each other) propagates freely (Left: Dashed line of Fig. 6.2). However, when $B_x \neq 0$, Eq. 6.2 induces a linear confining potential that prevents the domain walls from

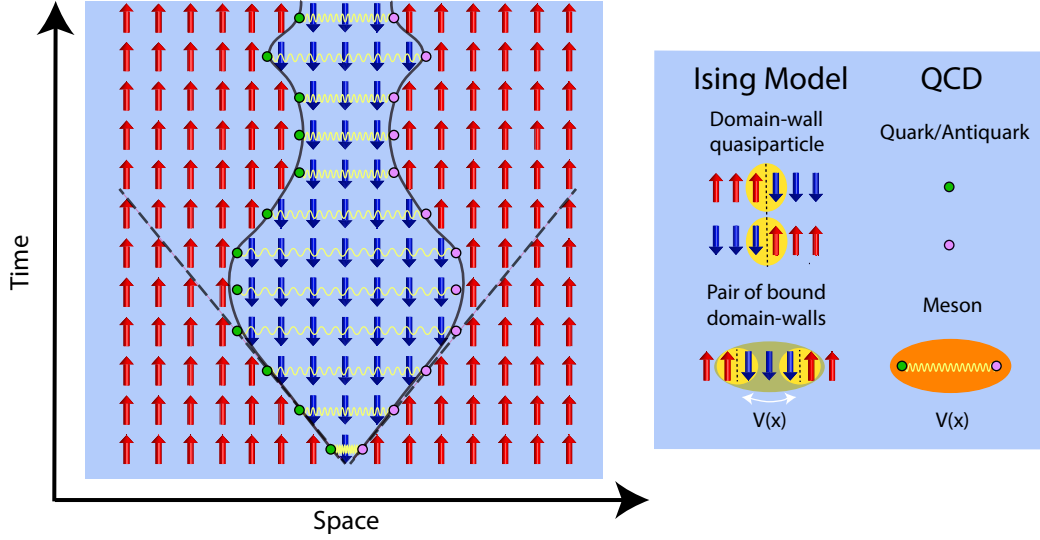


Figure 6.2: Domain-wall confinement analogy to color confinement in QCD. Left: An illustration of individual spin dynamics under the effects of confinement after a quantum quench. Spins up (down) are represented by red (blue) arrows where a domain-wall is the region between the spin up and down. The linear dashed line shows the domain-wall propagation after the quantum quench with nearest-neighbor TFIM. However, when there is an additional longitudinal field in the quench (Eq. 6.2), this additional field confines the pairs of domain-wall as shown in the black lines. Right: A domain wall (green circle) is represented as a quark, and the anti-aligned domain wall as antiquark (pink circle). In the presence of the confining field due to the longitudinal B -field, these two paired domain walls are bounded, creating a quasiparticle. This is analogous to the QCD's color confinement, where the two quarks are bounded to generate a meson.

propagating. The pair of bound domain walls creates a quasiparticle, similar to a meson in QCD. Such a confining potential that increases as the distance between the two domain walls lengthens is the main criteria for confinement in the many-body quantum system. The effect of confinement is measured by calculating the connected correlation along the interaction direction (x) $C_{i,j}^x(t)$. As shown in Ref [97], with $B_z = 0.25$, the correlation spreading is confined even for a small $B_x = 0.025$. Furthermore, the masses of the pairs of bound domain walls (quasiparticles) are exhibited by the oscillating dynamics of an observable.

6.2.2 Long-range TFIM for Confinement

The theoretical study of confinement in the many-body system is extended to the long-range TFIM without the longitudinal field² [101]. Liu et al. [101] find that the long-range interaction in the TFIM introduces an effective attractive force between a pair of domain-wall that confines them into a bound state (Left of Fig. 6.4) which is similar to Kormos' findings [97]. This long-range confinement Hamiltonian is given by:

$$H_{LR} = -(\sum_{i<j} J_{ij} \sigma_i^x \sigma_j^x + B_z \sum_i \sigma_i^z) \quad (6.3)$$

where $J_{ij} \approx J_0/|i,j|^\alpha$ is the power-law decaying Ising coupling between spins i and j with a tunable exponent α and $J_0 > 0$. The confining potential in this long-range model also increases with domain-wall separation (Fig. 6.3). Therefore, this model exhibits the effect of confinement, such that the dynamics of the connected-correlation $C_{i,j}^x(t)$ is confined as studied in Ref [97]. This is not expected to occur

²This theoretical study is experimentally possible and easier to implement with the current experimental setup.

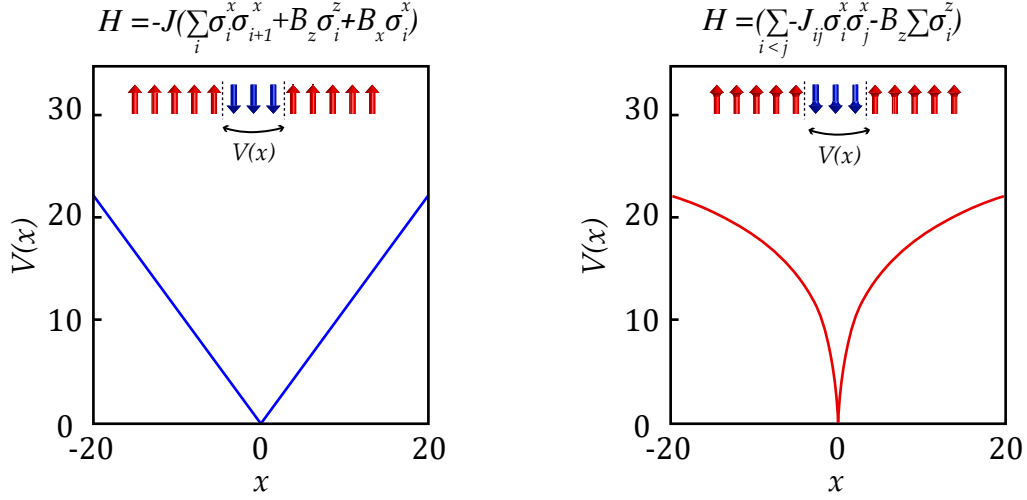


Figure 6.3: Confining potentials in the short-range and long-range TFIM are drawn for visualization. Left: The longitudinal field induces a linear confining potential with separation of the pairs of domain-walls. Right: The long-range interaction creates a confining potential that increases with the separation between paired domain-walls. This potential fulfills the criteria for confinement.

in a system with the Hamiltonian consisting of the long-range TFIM without the transverse field, in which the correlations spread faster than the Lieb-Robinson bound, as demonstrated experimentally in [90].

The low-energy excitations of this confinement Hamiltonian (Eq. 6.3) consists of states containing zero or two domain walls. By restricting the Hilbert space to include only these states, Liu et.al. build a ‘two-kink’ model or ‘two-domain-wall’ model for a ferromagnetic long-range TFIM that mimics the lower energy behavior of the system. The Hilbert space of this model consists of two outer domains as down-aligned spins and the center domains of length l as up-aligned spins. These domains are separated by two domain walls: one between spin positions $j - 1$ and j and another between position $j + l - 1$ and $j + l$. These domain-wall states have

the form:

$$|j, l\rangle = |\downarrow_1 \dots \downarrow_{j-1} \uparrow_j \dots \uparrow_{j+l-1} \downarrow_{j+l} \dots \downarrow\rangle \quad (6.4)$$

For a translation-invariant system, the above basis is transformed to a set of quasi-momentum basis state $|k, l\rangle = 1/L \sum_{j=1}^L \exp(-ikj - ikl/2) |j, 1\rangle$, which transform the Hamiltonian [101] as:

$$H = \sum_{k,l} V(l) |k, l\rangle \langle k, l| - 2B \cos(\frac{k}{2}) |k, l\rangle \langle k, l+1| - 2B \cos(\frac{k}{2}) |k, l\rangle \langle k, l-1| \quad (6.5)$$

The off-diagonal terms describe the effective kinetic energy of the domain walls with quasimomentum k from the transverse B -field. The interaction term J_{ij} introduces the potential term $V(l)$

$$V(l) = - \sum_{i < j}^L J_{ij} s_i(S) s_j(S) \quad (6.6)$$

where $s_i(S) = \pm 1$ is the value of the spin at site i corresponding to the configuration S with a two-domain-wall separation length l . This Hamiltonian is then diagonalized to extract the low-energy spectrum, which describes the bound-state due to the potential $V(l)$. Such confining potential depends on J_{ij} , which is approximated as the power-law r^α . For $\alpha < 2$, this potential is unbounded with the two-domain-wall separation, and all pairs of domain walls will be confined into quasiparticles.

6.3 Experimental results of Confinement

In the theoretical model, it assumes a closed-boundary condition, but the trapped-ion spin system is finite with an open-boundary condition. Therefore, to minimize deviation from the theoretical model, we consider only states with short, up-aligned domains with $l \ll L$ centered in the spin chain. We also minimize the

boundary effect [105] in the experiment because the center-to-center spin interaction strength is much stronger than the center-to-edge interaction strength. With these constraints, the experimental result matches well with the exact diagonalization (with $L \leq 21$) and the two-domain-wall model. For the two-domain wall model numerics, we take the experimental J_{ij} matrix to calculate the energy gaps for each experiment. First, from the J_{ij} matrix, we extract a vector of interaction parameters J_{kj} by fixing the site k to be the center ion for each ion chain length. We virtually place the ions on a ring to impose a periodic boundary condition for the Ising interaction to be translational invariant ($J_{lm} = J_{k,k+m-l}$). From here, we obtain Eq. 6.5 to be diagonalized to extract the energy spectrum and energy gaps with the experimental parameters.

Furthermore, the featured quantum simulators natively realize an antiferromagnetic TFIM. Since all measured observables $O(t)$ of the evolution are real and symmetric under time-reversal, the measured observables of Hamiltonian H and $-H$ are the same. Therefore, the expectation values from $J_{ij} > 0$ and $B > 0$ are identical to $J_{ij} < 0$ and $B < 0$. For this reason, we simulate the dynamics of a ferromagnetic system given by:

$$H = \sum_{i < j} J_{ij} \sigma_i^x \sigma_j^x + B_z \sum_i \sigma_i^z \quad (6.7)$$

This experiment has two parts. In this first part, we focus on the implications of confinement in correlation spreading and the measurement of bound-state energies. By measuring how correlations spread after quenching the confinement Hamiltonian, we show that confinement can dramatically suppress information propaga-

tion and thermalization in such many-body system. Then, we move on to determine the bound-state energies quantitatively by observing oscillation frequencies of the spin(s). Finally, we go beyond the confinement regime (deconfinement regime) to study the number of domain walls generated by the quantum quench for a wide range of transverse B_z strengths.

This experiment employs two quantum simulators which we refer as System 1 [52] and System 2 [11]. Both systems can generate the same quantum simulation Hamiltonian, but they differ in their environments. System 1 is room temperature apparatus. The main limitation of this apparatus is the rate of collision between the residual background gas in the UHV and the ion chain in which limits the size of the ion chain. However, this apparatus has individual addressing capabilities, which allows arbitrary spins flip. This is crucial in this work in investigating low-energy domain-wall bound states in smaller system sizes. System 2 is a linear blade RF trap (described in Chapter 2) in a cryogenic environment (featured in Chapter 3) with only global qubit control. The main reason of the cryogenic environment is to minimize the residual background gas collision with the ion chain and allow longer storage lifetimes of a large ion chain as compared to System 1. For this purpose, System 2 supports a large ion chain to measure the lowest bound-state energy and the confinement and deconfinement regimes.

6.3.1 Information Propagation due to the Effects of Confinement

To study the effect of confinement in such a many-body system, we apply a quantum quench to bring the system out of equilibrium (Right of Fig. 6.4). We

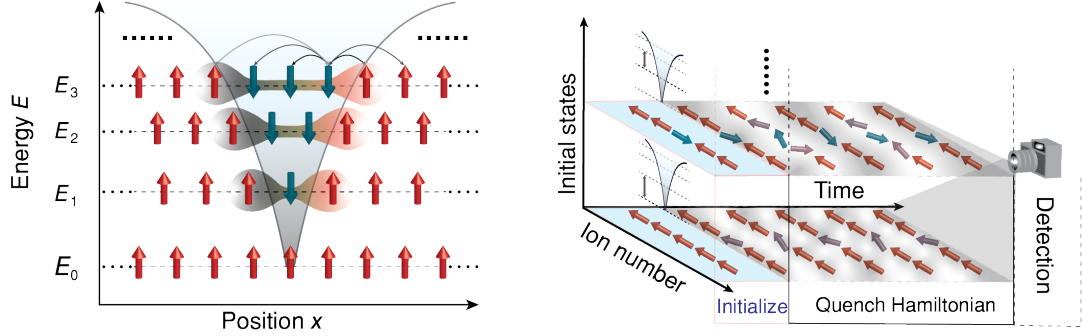


Figure 6.4: Effective confining potential and experiment sequence. Left: Under the confinement Hamiltonian, the pairs of domain walls in the Ising spin chains experience an effective confining potential that increases with distance analogously to the strong nuclear force in QCD. As a result, the pairs of bound domain-walls are bounded, creating meson-like quasiparticles (labeled E_1 to E_3), that dramatically changed the dynamics of the system. The grey arrows indicate long-range interactions between spins, where the opacity reflects interaction strengths that weaken with distance (interaction arrows are not shown for all spins). The shaded regions indicate interacting domain-wall quasiparticles. The dotted lines represent the extension of this model to larger systems. Right: The experiment begins by initializing a chain of trapped-ion spins in a product state which includes initial states with zero domain walls and two domain walls. The initialization of states is determined by the greatest overlap with the respective bound-state of the confinement Hamiltonian. Then, the initial state is evolved under the Hamiltonian for some time. We finally measure various observables, such as individual spin magnetization along any desired axis with a camera for site-resolved measurement. The grey double-ended arrows represent energy differences between two adjacent energy levels corresponding to a particular initial state.

initialize the spins into a product state, polarized wither along the x or z directions of the Bloch sphere. Using individual addressing laser beams, we prepare domain walls with various initial configurations (Fig. 6.5 c,f,i). After state initialization, we apply a sudden quench of the confinement Hamiltonian Eq. 6.7 with $B/J_0 \approx 0.75$. This B/J_0 is chosen such that this quench can drive the system out of equilibrium with a reasonable noise floor while remaining in the confinement regime. Following the time evolution of the system, we measure the state of spins with a 369.5 nm detection for spin-dependent fluorescence. From this, we can calculate the time-evolution of individual magnetization $\langle \sigma_i^{x,z} \rangle$ or the connected correlations $C_{i,j}^x(t)$.

To understand the consequences of confinement on information spreading, we measured the absolute value of connected correlation $C_{i,j}^x(t)$ along x (the Ising direction) (Fig. 6.5). When the initial state consists of small number of domain walls, the correlation spreads slower than the nearest-neighbor interacting system (white dashed lines in Fig. 6.5 with velocity $v_0 = 4B_z$). The correlation spreading is suppressed with localized correlation throughout the evolution [98, 100]. This implies that confinement due to long-range interactions confines the domain walls and localizes them at their initial conditions.

On the other hand, we observe a faster-than-linear spreading of connected correlations for many domain-walls initial states, in which the initial state is polarized along the z direction, despite quenching under the same Hamiltonian (Fig. 6.5). This initial state is a linear superposition of all possible spin configuration states that contain large domain walls. Unlike the previous initial states with small domain walls, this initial state has an energy density relatively far from the bottom of

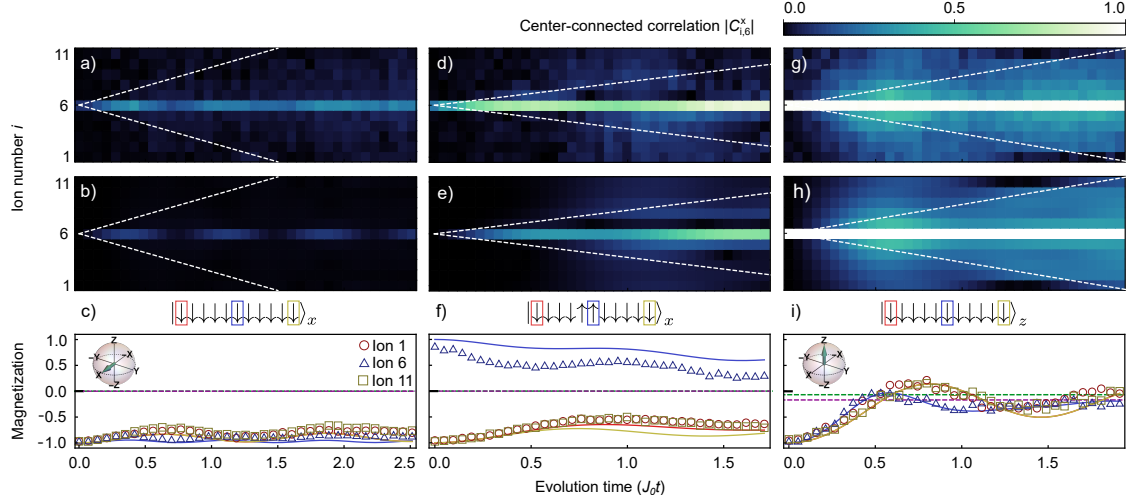


Figure 6.5: Confinement dynamics at $B/J_0 \approx 0.75$, $L = 11$. The initial states for each row are shown at the top of the last row. Top and middle rows: The absolute value of center-connected correlations $|C_{i,6}^x(t)|$ with white dashed lines representing the correlation propagation bounds (light cones) in the limit $\alpha \rightarrow \infty$ (nearest-neighbor interactions). Top row shows the experimental $|C_{i,6}^x(t)|$ averaged over 2000 experiments. Middle row shows $|C_{i,6}^x(t)|$ calculated by solving the Schrödinger equation. The bottom row shows the measured individual-spin magnetizations along their initialization axes, $\langle \sigma_i^{x,z}(t) \rangle$, averaged over 2000 experiments (400 experiments for i)). The color symbols represent magnetization data and solid colored curves represent theoretical magnetizations calculated by solving the Schrödinger equation. Purple (green) dashed lines represent thermal expectation values calculated from a canonical (microcanonical) ensemble averaged over the three displayed spins (see Supplementary Information). The spin diagrams above c), f) and i) depict the initial states prepared along the axes of the Bloch sphere shown by the inset diagrams. c and f are prepared along x (sharing the same inset) and i) is prepared along z. The boxed spins represent selected magnetization dynamics. a)-c), show a low-energy initial state containing zero domain walls. Individual magnetizations are $\langle \sigma_i^x(t) \rangle$. d)-f), show a low-energy initial state containing two domain walls, with a center domain of two spins. Individual magnetizations are $\langle \sigma_i^x(t) \rangle$. We attribute the discrepancy between the experimental magnetization data and numerics to imperfect state initialization. g)-i), show a high-energy initial state containing many domain walls. Individual magnetizations are $\langle \sigma_i^z(t) \rangle$. All magnetization error bars, ± 1 s.d., are smaller than their plot symbols and are not shown. a)-c), d)-f) and g)-i) share their respective x axes.

the many-body spectrum. Based on both results, the effect of confinement is only significant for low-energy excitation of the system.

Next, we measure the relaxation of magnetization for the above initial states to understand the effect of confinement on thermalization of local observables (third row of Fig. 6.5) [106]. For low-energy states (Fig. 6.5 c, f), the local magnetizations retain long memories relative to their initial states. For high-energy states (all x -polarized spins), on the other hand, each spin magnetization quickly relax to their thermal expectation values (Fig. 6.5 i). This result agrees with the observation where correlations spread quickly and distribute across the entire system. Therefore, from the correlation spreading and thermalization, we emphasize the confinement affects low-energy states, which is distinct from many-body localization with quenched disorder [107–109].

6.3.2 Bound-state Energies of Low Energy States

Under the effect of confinement, pair of bound domain-walls are confined, creating a quasiparticle with mass. The mass of these quasiparticles can be extracted from the dynamics of the observables since all local observables should exhibit oscillations with frequencies proportional to the energy gap between these bound states [97, 101]. Here, we choose to measure the time evolution of selected spins $\langle \sigma_i^z(t) \rangle$ under the quantum quench. Then, these oscillations are extracted to obtain the low-energy excitations.

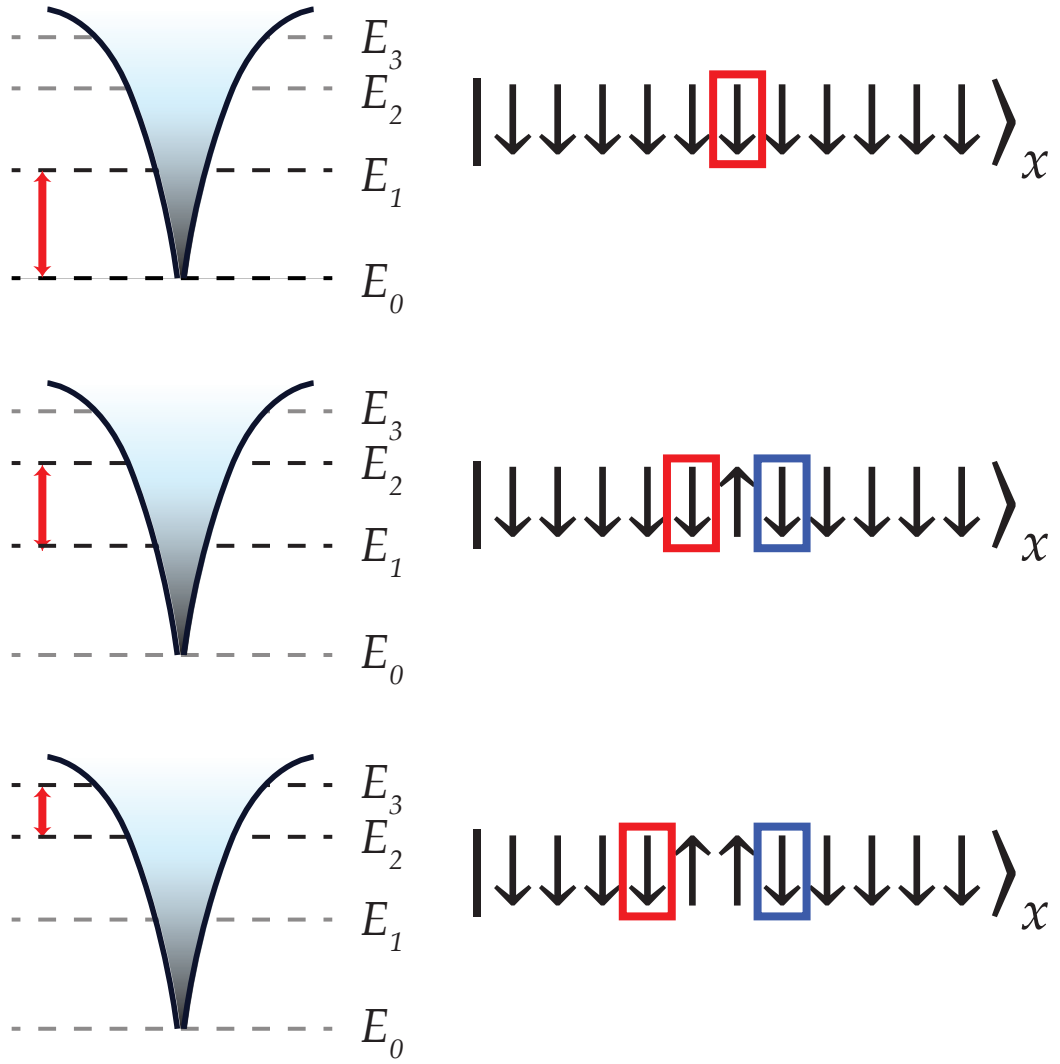


Figure 6.6: Initial states that predominantly overlap with the low-energy eigenstates of the confinement Hamiltonian. The oscillation frequencies from the dynamics of the color box spins (right) represents the corresponding bound-state energy differences (left).

6.3.2.1 Initial State and Measurement

In the confinement regime, we prepare the initial states such that they predominantly overlap with low-energy eigenstates of the confinement Hamiltonian [101]. The initial state $|n\rangle$ can be written as a superposition of post-quench eigenstates $|s\rangle$

$$|n\rangle = \sum_s c_{ns} |s\rangle \quad (6.8)$$

where c_{ns} is the overlap of $|s\rangle$ with the initial state $|n\rangle$. Thus, any observable M as a function of time is:

$$\langle M(t) \rangle = \sum_{ss'} c_{ns} c_{ns'}^* e^{-i(E_s - E_{s'})} \langle s' | M | s \rangle \quad (6.9)$$

where E_s is the energy of state $|s\rangle$. Therefore, $\langle M(t) \rangle$ exhibits oscillation frequencies corresponding to multiple bound-state energy differences, $\Delta E_{s,s'} = E_s - E_{s'}$ with different amplitudes, depending on the initial state (Fig. 6.6). In the experiment, we prepare initial states that overlap closely with low-energy eigenstates of the confinement Hamiltonian in Eq. 6.7 and choose to observe spins on the outer boundaries of the domain walls. This allows us to maximize the matrix elements ($\langle s' | M | s \rangle$) which couple the lower-energy bound state i to the adjacent higher-energy bound state $i + 1$. Therefore, the oscillation frequencies that we observe in Fig. 6.7 represent $\Delta E_{i,i+1}$.

Following this prescription, we extract oscillation frequencies using single-frequency sinusoidal fits of $\langle \sigma_i^z(t) \rangle$ to obtain the energy gap between each initialized state and the neighboring excited state (Fig. 6.7 a-c). We compare these extracted energies to values predicted by numerical simulation. We find excellent agreement

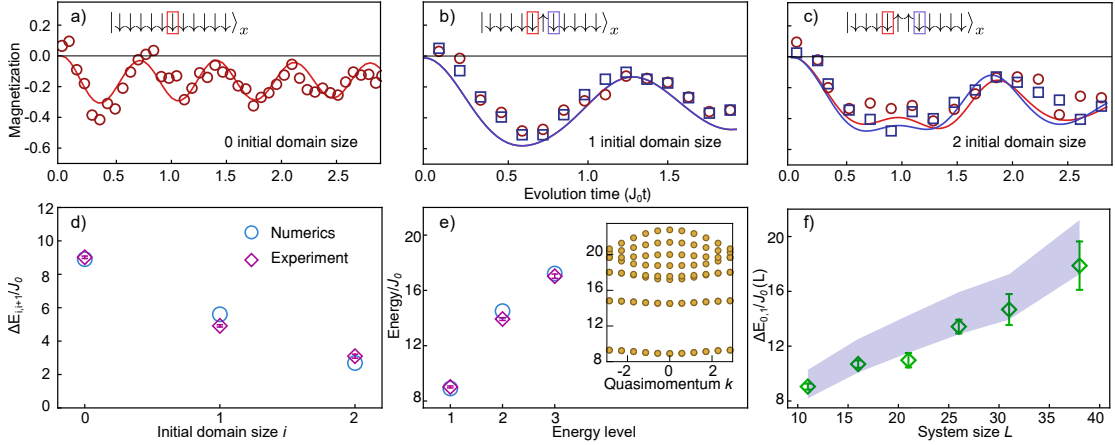


Figure 6.7: Low-energy excited states. a)-c), show the magnetizations of the boxed spins on the edges of the center domain at $B/J_0 \approx 0.75$. These magnetization oscillation frequencies correspond to the normalized energy gap, $\Delta E_{i,i+1}/J_0$. Solid colored lines represent theoretical calculations of dynamics by solving the Schrödinger equation. The error bars, $\pm 1\text{s.d.}$, are smaller than their plot markers and are not shown in a)-c). a) Zero initial domain size: $\Delta E_{0,1}/J_0$ is given by the frequency of the 6th spin. b) Initial domain size of one: $\Delta E_{1,2}/J_0$ is given by the frequency of the 5th and 7th spins. c) Initial domain size of two: $\Delta E_{2,3}/J_0$ is given by the frequency of the 4th and 7th spins. d) $\Delta E_{i,i+1}/J_0$ for $i \leq 2$ are measured with three different initial domain size spin configurations at $B/J_0 \approx 0.75$. The first three energy gaps ($i \leq 2$) are extracted from the magnetization oscillation frequencies shown in the top row. e) We construct the bound state energy levels at quasimomentum $k \approx 0$ using experimental data in d, where E_0/J_0 is set to zero. Inset: Theoretical bound state energy bands with different quasimomentum, k , within the two-domain-wall model. f) Scaling of $\Delta E_{0,1}/J_0$ with system size at $B/J_0 \approx 1$. The blue shaded region shows the two-domain-wall model numerical prediction of $\Delta E_{0,1}/J_0$, with a confidence band considering $\pm 10\%$ fluctuations in the Ising interaction strength J_0 .

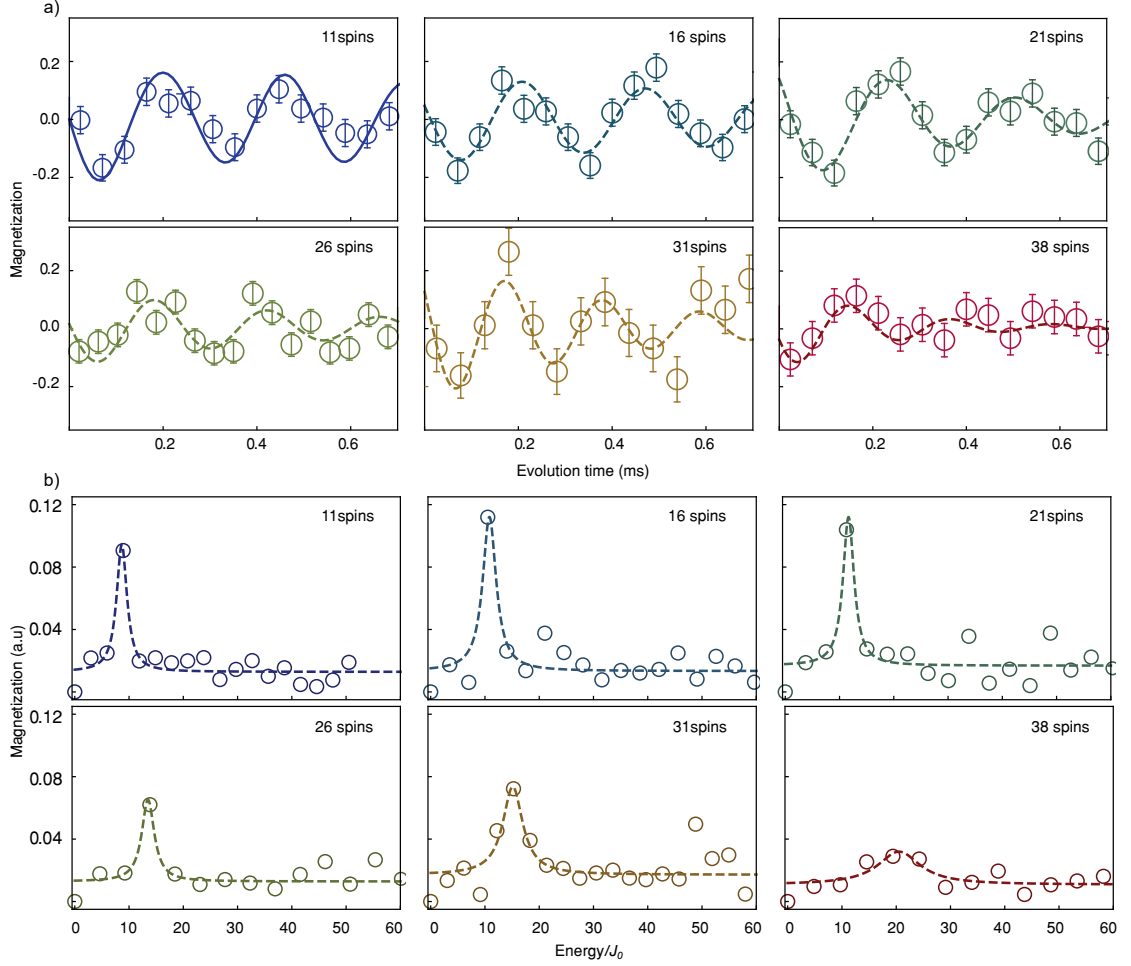


Figure 6.8: $\Delta E_{0,1}/J_0$ of all system sizes L at $B/J_0 \approx 1$ for Fig. 6.7 f). Circular dots indicate experimental data. a), shows the magnetization evolution of the center spin in a zero domain size initial state of various sizes L , measured in the y -basis. Solid blue line represents theoretical calculations of dynamics by solving the Schrödinger equation for the center spin of the $L = 11$ spin chain. Dashed colored lines show best fit curves of an exponentially-decaying sine function for $L = 16$ through $L = 38$. The oscillation frequencies are extracted from the fit and are normalized to each respective J_0 to obtain $\Delta E_{0,1}/J_0$. The error bars, ± 1 s.d., are calculated from the standard deviation of the mean with > 150 experiments per point. b) Fourier-transformed experimental results from a. Each $\Delta E_{0,1}/J_0$ of the different system sizes is extracted using a Lorentzian fit.

between the measured energies and the energies predicted numerically (Fig. 6.7 d). Using these experimentally measured energy gaps, we can systematically construct the low-energy excitation spectrum of the many-body system for quasimomentum $k \approx 0$ (Fig. 6.7 e). In general, quasiparticles with arbitrary quasimomenta can be excited by a quantum quench. However, since the confining potential is steep, excited quasiparticles remain localized, and their quasimomenta are close to zero.

Furthermore, leveraging the scalability of trapped-ion systems, we perform this experiment with up to 38 spins. In order to numerically investigate these large system sizes, we use a phenomenological two-domain-wall model. With this model, by restricting the full Hilbert space to a subspace of states containing only zero or two domain walls, we calculate the bound quasiparticle spectrum of Hamiltonian (Eq. 6.7) for system sizes that would be challenging to exactly simulate with classical resources (Fig. 6.7 f). We find reasonable agreement in the first excitation energy gap $\Delta E_{0,1}$ between the experimental data and numerical predictions for all system sizes (Fig. 6.7 f, 6.8, and 6.9). We attribute the systematic discrepancy in larger systems to variations in J_0 during the time evolution. These results, taken together, suggest that quench dynamics are dominated by the confinement effect between two-domain-wall quasiparticles.

6.3.2.2 Extracting Oscillation Frequencies

Due to the limited coherence time of the system, we cannot resolve the Fourier spectrum of the dynamics, especially for $\Delta E_{2,3}$ (Fig. 6.7 c), to extract the bound-state energy differences. Instead, we fit these frequencies to an exponentially-

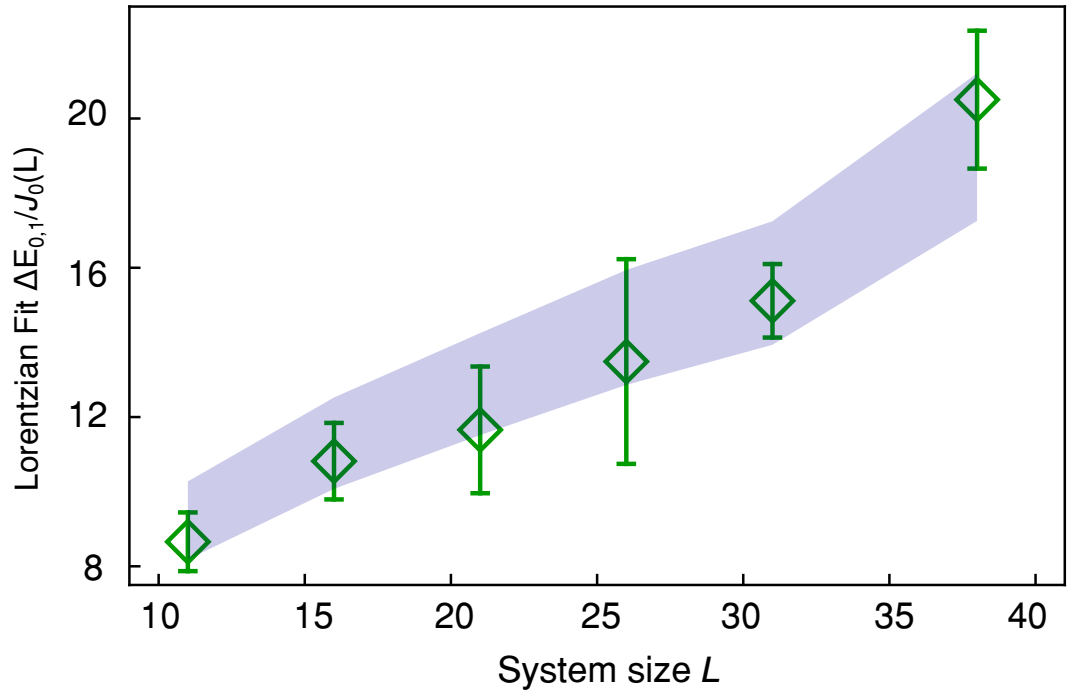


Figure 6.9: $\Delta E_{0,1}/J_0$ extracted from Lorentzian fit in different system sizes L . Diamond markers show $\Delta E_{0,1}/J_0$ for each system size with error bars from the fit (See Fig. S4). The blue band shows the two-domain-wall model numerical prediction of $\Delta E_{0,1}/J_0$, with a confidence band considering $\pm 10\%$ fluctuations in the Ising interaction strength J_0 .

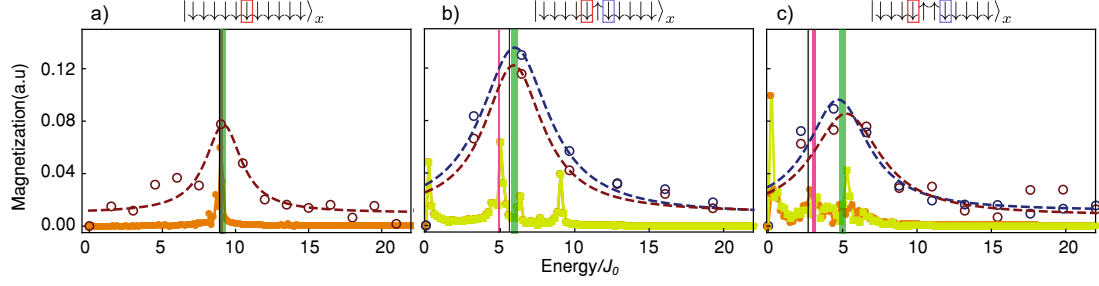


Figure 6.10: The Fourier-transformed spectrum of the bound-state energies with three different initial center-domain-size states in the $L = 11$ spin chain. The top row represents the initial state before the quantum quench. The dashed colored lines show the Fourier transform of the experimental data corresponding to the boxed spin shown in the top row. The black line describes the value predicted from the numerical calculations using the two-domain-wall model. The magenta band shows the bound-state energies from the sine fit of the data along with the errors of the fit. The green band represents the bound-state energies from Lorentzian fits of the Fourier-transformed experimental data along with the errors of the fits. The orange and yellow lines are the Fourier transform of theoretical calculations of dynamics by solving the Schrödinger equation for the corresponding labeled spins of each initial state.

decaying sine function. The error bars are the standard errors of these fits (Fig. 6.7 d-f). This fitting choice works well because we maximize the signal for $\Delta E_{i,i+1}$. $\Delta E_{i,i+1}$ also decreases as the energy level i increases (inset of Fig. 6.7 e). Using this knowledge, we can measure $\Delta E_{i,i+1}$ starting from the lowest energy initial state (all x -polarized) to the higher energy initial state (two domain walls with a domain size of two). Then, we take a suitable single frequency as a guess value in fitting the quench dynamics. The guess value is chosen such that it is the next lowest frequency from the oscillation frequency measured in the lower energy initial state. In the end, this method yields results that match closely with the two-domain-wall model and numerical simulations calculated by solving the Schrödinger equation. For a complete picture, we also Fourier-transformed experimental data (Fig. 6.10).

6.3.3 Number of Domain Walls at Various B-field Strength

At the final part, we go beyond the confinement regime to study the number of domain walls after the quantum quench with a wide range of B_z field strength. We start with all spin-polarized in the x -direction. For large B_z -fields, the strong quench can excite many domain walls that subsequently become unbounded, and the confinement picture for these parameters no longer captures the out-of-equilibrium dynamics. The observable we choose to explore this regime is the cumulative time average of the total number of domain walls:

$$\langle \mathcal{N} \rangle = \frac{1}{t_2 - t_1} \int_{t_1}^{t_2} \sum_{i=1}^{L-1} \frac{\langle 1 - \sigma_i^x(t) \sigma_{i+1}^x(t) \rangle}{2}, \quad (6.10)$$

where t_1 and t_2 enclose a window where $\langle \mathcal{N} \rangle$ converges to a stable value (Fig. 6.11). The expectation value is normalized by $1/2$ to correctly count the number of domain walls between neighboring spins [110]. We measure $\langle \mathcal{N} \rangle$ as a function of B for different system sizes (Fig. 6.12 a-e). We observe that, for small B fields, Ising interactions dominate the dynamics, and the global quench can only excite a small number of domain walls. However, for a large enough transverse field, the number of generated domain walls saturates to a value that scales nearly linearly with system size (Fig. 6.12 f). Here, we observe a transition between these two dynamical regimes at intermediate values of B for different system sizes. This behavior is analogous to the confinement-deconfinement crossover conjectured in QCD, in which increasing energy density (controlled by B in this experiment) causes hadronic matter to form a quark-gluon plasma or other exotic phase [96]. In both models, beyond a critical energy density, weaker interactions allow particles to freely move with negligible

energy penalty.

6.3.4 Domain-walls number at large B-field and at infinite temperature

In this domain wall investigation, we use the following Bloch sphere mapping: $z \leftrightarrow x$. The orientation of the i th spin in the Bloch sphere is defined as $|\psi_i(t)\rangle = \cos \theta(t)/2 |0\rangle + e^{i\phi} \sin \theta(t)/2 |1\rangle$. Let $|\psi\rangle = |\psi_i(t)\rangle \otimes |\psi_{i+1}(t)\rangle$ since we are interested in a two-body correlator for $\langle \mathcal{N} \rangle$. At high transverse B -field, global Larmor precession about the transverse direction dominates over the Ising interaction term in Eq. 6.7. The expectation value of the two-body correlator along z is $\langle \sigma_i^z(t) \sigma_{i+1}^z(t) \rangle = 1 - \sin^2(\theta(t))$. Inserting $\langle \sigma_i^z(t) \sigma_{i+1}^z(t) \rangle$ into Eq. 6.10 gives

$$\langle \mathcal{N} \rangle = \frac{1}{t_2 - t_1} \int_{t_1}^{t_2} \sum_i^{L-1} \frac{\sin^2(\theta(t))}{2} dt \quad (6.11)$$

Therefore, $\langle \mathcal{N} \rangle = 0.25(L - 1)$ when $B \gg J_0$ which gives the density of domain walls $\langle n \rangle_{B \gg J_0} = 0.25$ (purple dashed line in Fig 6.12 f). Values of t_1 and t_2 are chosen to include the plateaus of $\langle \mathcal{N} \rangle$ while excluding dephasing of the spins. We fix the scaled integration time $J_0(t_2 - t_1)$, as J_0 differs with system size (Fig. 6.11).

With a canonical ensemble at infinite temperature, there is equal probability in all the eigenstate of the confinement Hamiltonian. The spins are no longer correlate with each other. As a result, $\langle \sigma_i^z(t) \sigma_{i+1}^z(t) \rangle = 0$ and $\langle n \rangle_T = 0.5$. We note that, for $B \gg J_0$, the experiment operates in the prethermal region in which a transient Hamiltonian is approximately conserved for an exponentially long time [111–114]. Therefore, we expect the number of domain walls to approach the thermal value,

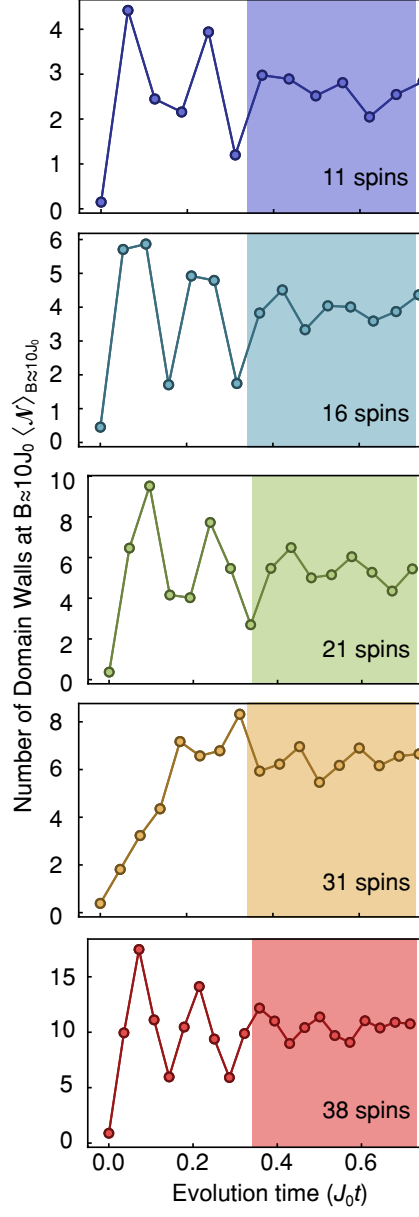


Figure 6.11: Evolution of domain wall population. Experimental data of evolution of the number of domain walls $\langle \mathcal{N} \rangle$ during a quench of Hamiltonian (Eq. 6.7) with $B/J_0 \approx 10$ for multiple system sizes. The shaded area indicates when $\langle \mathcal{N} \rangle$ converges to a steady-state and before qubit dephasing occurs.

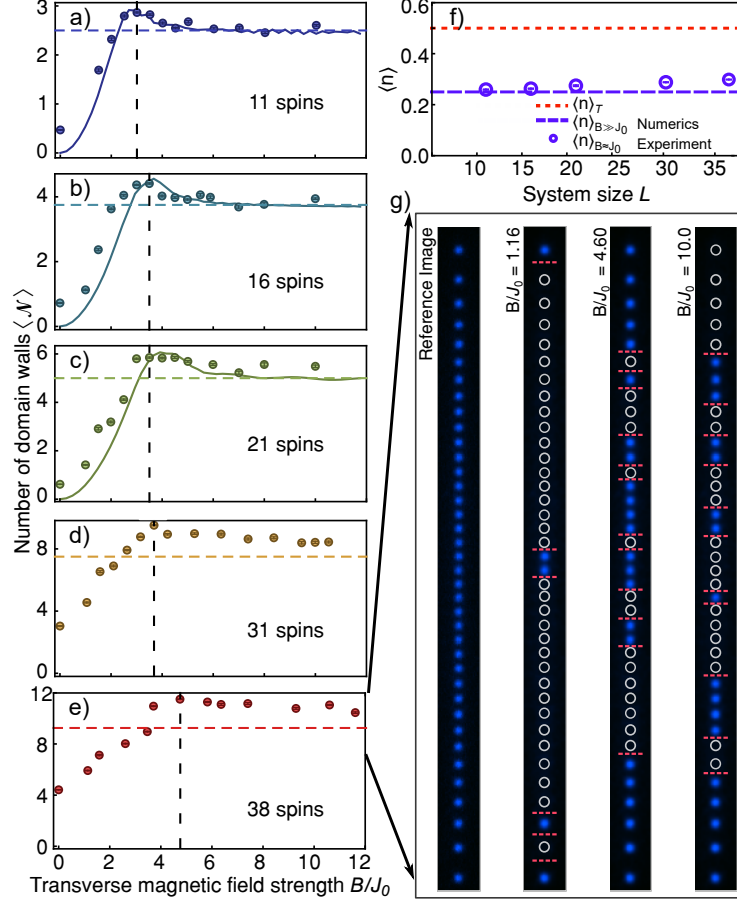


Figure 6.12: Number of domain walls in two dynamical regimes. a)-e) Exploring the two dynamical regimes with increasing transverse B -field strength in different system sizes. Circular dots indicate experimental data. Horizontal lines show the theoretical predictions of $\langle \mathcal{N} \rangle = 0.25(L - 1)$ at $B \gg J_0$. Colored continuous lines represent numerical results predicted by solving the Schrödinger equation. Vertical dashed lines indicate the experimental maxima of $\langle \mathcal{N} \rangle$. Theoretical lines for system sizes $L = 31$ and $L = 38$ are absent because we cannot compute the predicted evolution numerically for the experimental parameters. f) Dashed purple horizontal line shows the theoretical prediction of domain wall density at $B \gg J_0$, $\langle n \rangle_{B \gg J_0}$. The purple circular dots indicate experimental data of domain wall density at $B \approx 10J_0$, $\langle n \rangle_{B \approx 10J_0}$. The dashed red line at $\langle n \rangle_T = 0.5$ shows the density of domain walls using the canonical ensemble at infinite temperature. All the experimental data is integrated within the time interval $J_0 t_1 \approx 0.34$ and $J_0 t_2 \approx 0.73$. g) Reconstructed images based on binary detection of spin states. The leftmost image is a reference image of a 38 ion chain in a 'bright' state ($|\uparrow\rangle_x$). At the beginning of the experiment, the spins are initialized in the 'dark' state ($|\downarrow\rangle_x$). The three right images show experimental data of a combination of 'bright' and 'dark' states, marked in blue and white circles respectively, for three different B/J_0 values within the integrated time frame. The occurrences of domain walls are highlighted with orange horizontal dashed lines. The error bars are ± 1 s.d. with >150 experiments.

$\langle n \rangle_T = 0.5$, only after an exponentially long time, beyond the reach of this experiment.

6.4 Summary

In summary, we have presented a real-time observation of domain-wall confinement caused by long-range interactions in trapped-ion spin systems. By measuring oscillating magnetizations, we were able to construct the spectrum of low-energy domain wall bound states. Furthermore, we observed a transition between distinct dynamical behaviors using the number of domain walls generated by the global quench. This work demonstrates that confinement, naturally induced by long-range interactions, may provide a novel mechanism for protecting quantum information without engineering disorder. Such a feature may be applied in future studies to use long-range interactions to stabilize non-equilibrium phases of matter. Altogether, this work establishes the utility of trapped-ion quantum simulators for precisely studying real-time dynamics of many-body systems, potentially extending to exotic phenomena such as quark collision and string breaking [\[104\]](#).

Bibliography

- [1] N. M. Linke, D. Maslov, M. Roetteler, S. Debnath, C. Figgatt, K. A. Landsman, K. Wright, and C. Monroe. Experimental Comparison of Two Quantum Computing Architectures. *Proceedings of the National Academy of Sciences*, 114:3305–3310, March 2017.
- [2] P. Murali, N. M. Linke, M. Martonosi, A. J. Abhari, N. H. Nguyen, and C. H. Alderete. Full-Stack, Real-System Quantum Computer Studies: Architectural Comparisons and Design Insights. arXiv, 2017.
- [3] C. Monroe, W. C. Campbell, L. M. Duan, Z. X. Gong, A. V. Gorshkov, P. Hess, R. Islam, K. Kim, G. Pagano, P. Richerme, C. Senko, and N. Y. Yao. Programmable Quantum Simulations of Spin Systems with Trapped Ions. arXiv, 2019.
- [4] Y. Wang, M. Um, J. Zhang, S. An, M. Lyu, J. N. Zhang, L. M. Duan, D. Yum, and K. Kim. Single-qubit Quantum Memory Exceeding Ten-minute Coherence Time. *Nature Photonics*, 11:646–650, September 2017.
- [5] P. Wang, C. Y. Luan, M. Qiao, M. Um, J. Zhang, Y. Wang, X. Yuan, M. Gu, J. Zhang, and K. Kim. Single ion qubit with estimated coherence time exceeding one hour. *Nat Commun*, 12:233, January 2021.
- [6] A. H. Myerson, D. J. Szwer, S. C. Webster, D. T. C. Allcock, M. J. Curtis, G. Imreh, J. A. Sherman, D. N. Stacey, A. M. Steane, and D. M. Lucas. High-Fidelity Readout of Trapped-Ion Qubits. *Phys. Rev. Lett.*, 100:200502, May 2008.
- [7] S. Crain, C. Cahall, G. Vrijsen, E. E. Wollman, M. D. Shaw, V. B. Verma, S. W. Nam, and J. Kim. High-speed Low-crosstalk Detection of a $^{171}\text{Yb}^+$ Qubit Using Superconducting Nanowire Single Photon Detectors. *Nature Comm. Physics*, 2, August 2019.
- [8] C. Monroe, D. M. Meekhof, B. E. King, W. M. Itano, and D. J. Wineland. Demonstration of a Fundamental Quantum Logic Gate. *Phys. Rev. Lett.*, 75, December 1995.

- [9] A. Seif, K. A. Landsman, N. M. Linke, C. Figgatt, C. Monroe, and M. Hafezi. Machine learning assisted readout of trapped-ion qubits. *Journal of Physics B: Atomic, Molecular and Optical Physics*, 51(17):174006, aug 2018.
- [10] K. A. Landsman, Y. Wu, P. H. Leung, D. Zhu, N. M. Linke, K. R. Brown, L. Duan, and C. Monroe. Two-qubit entangling gates within arbitrarily long chains of trapped ions. *Phys. Rev. A*, 100, August 2019.
- [11] G. Pagano, P. W. Hess, H. B. Kaplan, W. L. Tan, P. Richerme, P. Becker, A. Kyprianidis, J. Zhang, E. Birkelbaw, M. R. Hernandez, Y. Wu, and C. Monroe. Cryogenic trapped-ion system for large scale quantum simulation. *Quantum Science and Technology*, 4(1):014004, Oct 2018.
- [12] L. Feng, W. L. Tan, A. De, A. Menon, A. Chu, G. Pagano, and C. Monroe. Efficient Ground-State Cooling of Large Trapped-Ion Chains with an Electromagnetically-Induced-Transparency Tripod Scheme. *Phys. Rev. Lett.*, 125:053001, Jul 2020.
- [13] W. L. Tan, P. Becker, F. Liu, G. Pagano, K. S. Collins, A. De, L. Feng, H. B. Kaplan, A. Kyprianidis, R. Lundgren, W. Morong, S. Whitsitt, A. V. Gorshkov, and C. Monroe. Domain-wall confinement and dynamics in a quantum simulator. *Nature Physics*, March 2021. Reproduced with permission from Springer Nature.
- [14] S. Olmschenk, K. C. Younge, D. L. Moehring, D. N. Matsukevich, P. Maunz, and C. Monroe. Manipulation and detection of a trapped Yb^+ hyperfine qubit. *Phys. Rev. A*, 76:052314, November 2007.
- [15] S. Olmschenk, D. Hayes, D. N. Matsukevich, P. Maunz, D. L. Moehring, K. C. Younge, and C. Monroe. Measurement of the lifetime of the $6p^2P_{1/2}^0$ level of Yb^+ . *Phys. Rev. A*, 80:022502, August 2009.
- [16] H. J. Metcalf and P. van der Straten. *Laser Cooling and Trapping*. Springer-Verlag New York, 1999.
- [17] W. M. Itano and D. J. Wineland. Laser cooling of ions stored in harmonic and Penning traps. *Phys. Rev. A*, 25:35, January 1982.
- [18] J. D. Wong-Campos. *Demonstration of a Quantum Gate with Ultrafast Laser Pulses*. PhD thesis, University of Maryland, 2017.
- [19] M. G. Raizen, J. M. Gilligan, J. C. Bergquist, W. M. Itano, and D. J. Wineland. Ionic crystals in a linear Paul trap. *Phys. Rev. A*, 45:6493–6501, May 1992.
- [20] D. J. Berkeland, J. D. Miller, J. C. Bergquist, W. M. Itano, and D. J. Wineland. Minimization of ion micromotion in a Paul trap. *Journal of Applied Physics*, 83(10):5025–5033, 1998.

- [21] S. Olmschenk. *Quantum Teleportation Between Distant Matter Qubits*. PhD thesis, University of Michigan, 2009.
- [22] P. K. Ghosh. *Ion Traps*. Oxford University Press, January 1996.
- [23] S. Fishman, G. D. Chiara, T. Calarco, and G. Morigi. Structural phase transitions in low-dimensional ion crystals. *Phys. Rev. B*, 77:064111, Feb 2008.
- [24] K. Mølmer and A. Sørensen. Multiparticle entanglement of hot trapped ions. *Phys. Rev. Lett.*, 82:1835–1838, March 1999.
- [25] A. Sørensen and K. Mølmer. Entanglement and quantum computation with ions in thermal motion. *Phys. Rev. A*, 62:022311, July 2000.
- [26] D. F. V. James. Quantum dynamics of cold trapped ions with application to quantum computation. *Applied Physics B*, 66:181–190, July 1998.
- [27] K. Sosnova, A. Carter, and C. Monroe. Character of motional modes for entanglement and sympathetic cooling of mixed-species trapped-ion chains. *Phys. Rev. A*, 103:012610, Jan 2021.
- [28] M. A. Mamun, A. A. Elmustafa, M. L. Stutzman, P. A. Adderley, and M. Poelker. Effect of heat treatments and coatings on the outgassing rate of stainless steel chambers. *Journal of Vacuum Science & Technology A*, 32(2):021604, 2014.
- [29] G. Gabrielse, A. Khabbaz, D. S. Hall, C. Heimann, H. Kalinowsky, and W. Jhe. Precision Mass Spectroscopy of the Antiproton and Proton Using Simultaneously Trapped Particles. *Phys. Rev. Lett.*, 82:3198–3201, Apr 1999.
- [30] Q. A. Turchette, D. Kielpinski, B. E. King, D. Leibfried, D. M. Meekhof, C. J. Myatt, M. A. Rowe, C. A. Sackett, C. S. Wood, W. M. Itano, C. Monroe, and D. J. Wineland. Heating of trapped ions from the quantum ground state. *Phys. Rev. A*, 61:063418, May 2000.
- [31] M. Niedermayr, K. Lakhmanskiy, M. Kumph, S. Partel, J. Edlinger, M. Brownnutt, and R. Blatt. Cryogenic surface ion trap based on intrinsic silicon. *New Journal of Physics*, 16(11):113068, November 2014.
- [32] M. Brownnutt, M. Kumph, P. Rabl, and R. Blatt. Ion-trap measurements of electric-field noise near surfaces. *Rev. Mod. Phys.*, 87:1419–1482, Dec 2015.
- [33] M. E. Poitzsch, J. C. Bergquist, W. M. Itano, and D. J. Wineland. Cryogenic linear ion trap for accurate spectroscopy. *Review of Scientific Instruments*, 67(1):129–134, 1996.
- [34] P. B. Antohi, D. Schuster, G. M. Akselrod, J. Labaziewicz, Y. Ge, Z. Lin, W. S. Bakr, and I. L. Chuang. Cryogenic ion trapping systems with surface-electrode traps. *Review of Scientific Instruments*, 80(1):013103, 2009.

- [35] M. F. Brandl, M. W. van Mourik, L. Postler, A. Nolf, K. Lakhmanskiy, R.R. Paiva, S. Möller, N. Daniilidis, H. Häffner, V. Kaushal, T. Ruster, C. Warschburger, H. Kaufmann, F. Schmidt-Kaler U.G. Poschinger, P. Schindler, T. Monz, and R. Blatt. Cryogenic setup for trapped ion quantum computing. *Review of Scientific Instruments*, 87(11):113103, 2016.
- [36] W. W. Macalpine and R. O. Schildknecht. Coaxial Resonators with Helical Inner Conductor. *Proceedings of the IRE*, 47(12):2099–2105, 1959.
- [37] J. D. Siverns, L. R. Simkins, S. Weidt, and W. K. Hensinger. On the application of radio frequency voltages to ion traps via helical resonators. *Appl. Phys. B*, 107:921–934, January 2012.
- [38] K. G. Johnson, J. D. Wong-Campos, A. Restelli, K. A. Landsman, B. Neyenhuis, J. Mizrahi, and C. Monroe. Active stabilization of ion trap radiofrequency potentials. *Review of Scientific Instruments*, 87(5):053110, 2016.
- [39] J. Ekin. *Experimental Techniques for Low-Temperature Measurements: Cryostat Design, Material Properties and Superconductor Critical-Current Testing*. Oxford University Press, January 2010.
- [40] S. M. Brewer, J.-S. Chen, A. M. Hankin, E. R. Clements, C. W. Chou, D. J. Wineland, D. B. Hume, and D. R. Leibrandt. $^{27}\text{Al}^+$ Quantum-Logic Clock with a Systematic Uncertainty below 10^{-18} . *Phys. Rev. Lett.*, 123:033201, Jul 2019.
- [41] K. G. Johnson, J. D. Wong-Campos, A. Restelli, K. A. Landsman, B. Neyenhuis, J. Mizrahi, and C. Monroe. Active stabilization of ion trap radiofrequency potentials. *Review of Scientific Instruments*, 87(5):053110, 2016.
- [42] C. Zipkes, L. Ratschbacher, C. Sias, and M. Köhl. Kinetics of a single trapped ion in an ultracold buffer gas. *New Journal of Physics*, 13(5):053020, may 2011.
- [43] M. Cetina, A. T. Grier, and V. Vuletić. Micromotion-Induced Limit to Atom-Ion Sympathetic Cooling in Paul Traps. *Phys. Rev. Lett.*, 109:253201, Dec 2012.
- [44] K. Chen, S. T. Sullivan, and E. R. Hudson. Neutral Gas Sympathetic Cooling of an Ion in a Paul Trap. *Phys. Rev. Lett.*, 112:143009, Apr 2014.
- [45] V. L. Ryjkov, X. Zhao, and H. A. Schuessler. Simulations of the rf heating rates in a linear quadrupole ion trap. *Phys. Rev. A*, 71:033414, Mar 2005.
- [46] J. Zhang, G. Pagano, P. W. Hess, A. Kyprianidis, P. Becker, H. Kaplan, A. V. Gorshkov, Z.-X. Gong, and C. Monroe. Observation of a many-body dynamical phase transition with a 53-qubit quantum simulator. *Nature*, 551:601–604, November 2017.

- [47] P. Langevin. Une formule fondamentale de theorie cinetique. *Annales de Chimie et de Physique*, 5:245–288, 1905.
- [48] K. Jachymski, M. Krych, P. S. Julienne, and Z. Idziaszek. Quantum Theory of Reactive Collisions for $1/r^n$ Potentials. *Phys. Rev. Lett.*, 110:213202, May 2013.
- [49] H. Lehmitz, J. Hattendorf-Ledwoch, R. Blatt, and H. Harde. Population trapping in excited Yb ions. *Phys. Rev. Lett.*, 62:2108–2111, May 1989.
- [50] K. Sugiyama and J. Yoda. Production of YbH^+ by chemical reaction of Yb^+ in excited states with H_2 gas. *Phys. Rev. A*, 55:R10–R13, Jan 1997.
- [51] Y. Aikyo, G. Vrijsen, T. W. Noel, A. Kato, M. K. Ivory, and J. Kim. Vacuum characterization of a compact room-temperature trapped ion system. *Applied Physics Letters*, 117(23):234002, 2020.
- [52] K. Kim, M.-S. Chang, R. Islam, S. Korenblit, L.-M. Duan, and C. Monroe. Entanglement and Tunable Spin-Spin Couplings between Trapped Ions Using Multiple Transverse Modes. *Phys. Rev. Lett.*, 103:120502, September 2009.
- [53] I. V. Inlek, G. Vittorini, D. Hucul, C. Crocker, and C. Monroe. Quantum gates with phase stability over space and time. *Phys. Rev. A*, 90:042316, Oct 2014.
- [54] C. Ospelkaus, U. Warring, Y. Colombe, K. R. Brown, J. M. Amini, D. Leibfried, and D. J. Wineland. Microwave quantum logic gates for trapped ions. *Nature*, 476:181–184, 2011.
- [55] R. T. Sutherland, R. Srinivas, S. C. Burd, H. M. Knaack, A. C. Wilson, D. J. Wineland, D. Leibfried, D. T. C. Allcock, D. H. Slichter, and S. B. Libby. Laser-free trapped-ion entangling gates with simultaneous insensitivity to qubit and motional decoherence. *Phys. Rev. A*, 101:042334, April 2020.
- [56] D. A. Steck. Quantum and Atom Optics. available online at <http://steck.us/teaching>. (revision 0.13.4 September 2020).
- [57] L. Deslauriers. *Cooling and Heating of the Quantum Motion of Trapped Cadmium Ions*. PhD thesis, University of Michigan, 2006.
- [58] S. Sachdev. *Quantum Phase Transitions*. Cambridge University Press, May 2011.
- [59] T. Choi, S. Debnath, T.A. Manning, C. Figgatt, Z.-X. Gong, L.-M. Duan, , and C. Monroe. Optimal Quantum Control of Multimode Couplings between Trapped Ion Qubits for Scalable Entanglement. *Phys. Rev. Lett.*, 112:190502, May 2014.
- [60] S. L. Zhu, C. Monroe, and L. M. Duan. Arbitrary-speed quantum gates within large ion crystals through minimum control of laser beams. *EPL (Europhysics Letters)*, 73:485, Jan 2006.

- [61] S. L. Zhu, C. Monroe, and L. M. Duan. Trapped Ion Quantum Computation with Transverse Phonon Modes. *Phys. Rev. Lett.*, 97:050505, August 2006.
- [62] A. C. Lee. *Engineering a Quantum Many-Body Hamiltonian with Trapped Ions*. PhD thesis, University of Maryland, 2016.
- [63] C.-C. J. Wang and J. K. Freericks. Programmable Quantum Simulations of Spin Systems with Trapped Ions. arXiv, 2010.
- [64] C.-C. J. Wang and J. K. Freericks. Intrinsic phonon effects on analog quantum simulators with ultracold trapped ions. *Phys. Rev. A*, 86, September 2012.
- [65] P. C. Haljan, K. A. Brickman, L. Deslauriers, P. J. Lee, and C. Monroe. Spin-Dependent Forces on Trapped Ions for Phase-Stable Quantum Gates and Entangled States of Spin and Motion. *Phys. Rev. Lett.*, 94:153602, April 2005.
- [66] S. Ejtemaee and P. C. Haljan. 3D Sisyphus Cooling of Trapped Ions. *Phys. Rev. Lett.*, 119:043001, Jul 2017.
- [67] D. Leibfried, R. Blatt, C. Monroe, and D. Wineland. Quantum dynamics of single trapped ions. *Rev. Mod. Phys.*, 75:281–324, Mar 2003.
- [68] G. Morigi, J. Eschner, and C. H. Keitel. Ground State Laser Cooling Using Electromagnetically Induced Transparency. *Phys. Rev. Lett.*, 85:4458–4461, Nov 2000.
- [69] J. S. Chen, K. Wright, N. C. Pisenti, D. Murphy, K. M. Beck, K. Landsman, J. M. Amini, and Y. Nam. Efficient-sideband-cooling protocol for long trapped-ion chains. *Phys. Rev. A*, 102:043110, Oct 2020.
- [70] S. E. Harris. Electromagnetically Induced Transparency. *Physics Today*, 50:36, July 1997.
- [71] E. Arimondo and G. Orriols. Nonabsorbing atomic coherences by coherent two-photon transitions in a three-level optical pumping. *Lettere al Nuovo Cimento (1971-1985)*, 17:333–338, November 1976.
- [72] H. R. Gray, R. M. Whitley, and C. R. Stroud. Coherent trapping of atomic populations. *Optics Letters*, 3:218–220, 1978.
- [73] B. Lounis and C. Cohen-Tannoudji. Coherent population trapping and Fano profiles. *J. Phys. II France*, 2:579–592, April 1992.
- [74] P. M. Radmore and P. L. Knight. Two-photon ionisation: Interference and population trapping. *Physics Letters A*, 102:180–185, May 1984.
- [75] W. W. Erickson. Electromagnetically Induced Transparency, Undergraduate thesis, Reed College, 2012.

- [76] R. Lechner, C. Maier, C. Hempel, P. Jurcevic, B. P. Lanyon, Thomas Monz, M. Brownnutt, R. Blatt, and C. F. Roos. Electromagnetically-induced-transparency ground-state cooling of long ion strings. *Phys. Rev. A*, 93:053401, May 2016.
- [77] J. Evers and C. H. Keitel. Double-EIT ground-state laser cooling without blue-sideband heating. *EPL (Europhysics Letters)*, 68:370, October 2004.
- [78] Y. Lu, J.-Q. Zhang, J. M. Cui, D. Y. Cao, S. Zhang, Y. F. Huang, C. F. Li, and G. C. Guo. Dark-state cooling of a trapped ion using microwave coupling. *Phys. Rev. A*, 92:023420, Aug 2015.
- [79] I. A. Semerikov, I. V. Zalivako, A. S. Borisenko, K. Y. Khabarova, and N. N. Kolachevsky. EIT Ground State Cooling Scheme of $^{171}\text{Yb}^+$ Based on the $^2\text{S}_{1/2} \rightarrow ^2\text{P}_{1/2}$ Cooling Transition. *Journal of Russian Laser Research*, 39:568–574, November 2018.
- [80] N. Scharnhorst, J. Cerrillo, J. Kramer, I. D. Leroux, J. B. Wübbena, A. Retzker, and P. O. Schmidt. Experimental and theoretical investigation of a multi-mode cooling scheme using multiple electromagnetically-induced-transparency resonances. *Phys. Rev. A*, 98:023424, Aug 2018.
- [81] M. Qiao, Y. Wang, Z. Cai, B. Du, P. Wang, C. Luan, W. Chen, H. R. Noh, and K. Kim. Double-EIT Ground-State Cooling of Stationary Two-Dimensional Ion Lattices. arXiv:2003.10276, 2020.
- [82] A. Shankar, E. Jordan, K. A. Gilmore, A. Safavi-Naini, J. J. Bollinger, and M. J. Holland. Modeling near ground-state cooling of two-dimensional ion crystals in a Penning trap using electromagnetically induced transparency. *Phys. Rev. A*, 99:023409, Feb 2019.
- [83] T. D. Ladd, F. Jelezko, R. Laflamme, Y. Nakamura, C. Monroe, and J. L. O’Brien. Quantum Computer. *Nature*, 464:45–53, March 2010.
- [84] M. A. Nielsen and I. L. Chuang. *Quantum Computation and Quantum Information*. Cambridge University Press, June 2000.
- [85] G. Pagano, A. Bapat, P. Becker, K. S. Collins, A. De, P. W. Hess, H. B. Kaplan, A. Kyprianidis, W. L. Tan, C. Baldwin, L. T. Brady, A. Deshpande, F. Liu, S. Jordan, A. V. Gorshkov, and C. Monroe. Quantum approximate optimization of the long-range Ising model with a trapped-ion quantum simulator. *Proceedings of the National Academy of Sciences*, 117(41):25396–25401, 2020.
- [86] H. B. Kaplan., L. Guo, W. L. Tan, A. De, F. Marquardt, G. Pagano, and C. Monroe. Many-Body Dephasing in a Trapped-Ion Quantum Simulator. *Phys. Rev. Lett.*, 125:120605, Sep 2020.

- [87] B. Nachtergaele, Y. Ogato, and R. Sims. Propagation of Correlations in Quantum Lattice Systems. *J Stat Phys*, 124:1–13, July 2006.
- [88] P. Hauke and L. Tagliacozzo. Spread of Correlations in Long-Range Interacting Quantum Systems. *Phys. Rev. Lett.*, 111:207202, Nov 2013.
- [89] K. A. Landsman, C. Figgatt, T. Schuster, N. M. Linke, B. Yoshida, N. Y. Yao, and C. Monroe. Verified quantum information scrambling. *Nature*, 567:61–65, March 2019.
- [90] P. Richerme, Z.-X. Gong, A. Lee, C. Senko, J. Smith, M. Foss-Feig, S. Michalakakis, A. V. Gorshkov, , and C. Monroe. Non-local propagation of correlations in quantum systems with long-range interactions. *Nature*, 511:198–201, July 2014.
- [91] M.Foss-Feig, Z.-X. Gong, A. V. Gorshkov, and C. W. Clark. Entanglement and spin-squeezing without infinite-range interactions, 2016.
- [92] E. H. Lieb and D. W. Robinson. The finite group velocity of quantum spin systems. *Commun.Math. Phys.*, 28:251–257, September 1972.
- [93] T. Kuwahara and K. Saito. Strictly Linear Light Cones in Long-Range Interacting Systems of Arbitrary Dimensions. *Phys. Rev. X*, 10:031010, Jul 2020.
- [94] M. C. Tran, C.-F. Chen, A. Ehrenberg, A. Y. Guo, A. Deshpande, Y. Hong, Z.-X. Gong, A. V. Gorshkov, and A. Lucas. Hierarchy of Linear Light Cones with Long-Range Interactions. *Phys. Rev. X*, 10:031009, Jul 2020.
- [95] J. Greensite. *An Introduction to the Confinement Problem*. Springer, Berlin, Heidelberg, 2011.
- [96] N. Brambilla, S. Eidelman, P. Foka, S. Gardner, A. S. Kronfeld, M. G. Alford, R. Alkofer, M. Butenschoen, T. D. Cohen, J. Erdmenger, et al. QCD and strongly coupled gauge theories: challenges and perspectives. *Eur. Phys. J. C*, 74(2981), October 2014.
- [97] M. Kormos, M. Collura, G. Takács, and P. Calabrese. Real-time confinement following a quantum quench to a non-integrable model. *Nature Physics*, 13:246–249, November 2017.
- [98] L. F. Santos, F. Borgonovi, and G. L. Celardo. Cooperative Shielding in Many-Body Systems with Long-Range Interaction. *Phys. Rev. Lett.*, 116:250402, Jun 2016.
- [99] A. Leroose, B. Žunkovič, A. Silva, and A. Gambassi. Quasilocal excitations induced by long-range interactions in translationally invariant quantum spin chains. *Phys. Rev. B*, 99:121112, Mar 2019.

- [100] A. J. A. James, R. M. Konik, and N. J. Robinson. Nonthermal States Arising from Confinement in One and Two Dimensions. *Phys. Rev. Lett.*, 122:130603, Apr 2019.
- [101] F. Liu, R. Lundgren, P. Titum, G. Pagano, J. Zhang, C. Monroe, and A. V. Gorshkov. Confined Quasiparticle Dynamics in Long-Range Interacting Quantum Spin Chains. *Phys. Rev. Lett.*, 122:150601, Apr 2019.
- [102] P. P. Mazza, G. Perfetto, A. Leroose, M. Collura, and A. Gambassi. Suppression of transport in nondisordered quantum spin chains due to confined excitations. *Phys. Rev. B*, 99:180302, May 2019.
- [103] A. Leroose, F. M. Surace, P. P. Mazza, G. Perfetto, M. Collura, and A. Gambassi. Quasilocalized dynamics from confinement of quantum excitations. *Phys. Rev. B*, 102:041118, July 2020.
- [104] R. Verdel, F. Liu, S. Whitsitt, A. V. Gorshkov, and M. Heyl. Real-time dynamics of string breaking in quantum spin chains. *Phys. Rev. B*, 102:014308, July 2020.
- [105] B. Neyenhuis, J. Zhang, P. W. Hess, J. Smith, A. C. Lee, P. Richerme, Z.-X. Gong, A. V. Gorshkov, and C. Monroe. Observation of prethermalization in long-range interacting spin chains. *Science Advances*, 3(8), 2017.
- [106] P. Calabrese and J. Cardy. Time Dependence of Correlation Functions Following a Quantum Quench. *Phys. Rev. Lett.*, 96:136801, Apr 2006.
- [107] M. Schreiber, S. S. Hodgman, P. Bordia, H.P. Lüschen, M. H. Fischer, R. Vosk, E. Altman, U. Schneider, and I. Bloch. Observation of many-body localization of interacting fermions in a quasirandom optical lattice. *Science*, 349(6250):842–845, 2015.
- [108] R. Nandkishore and D. A. Huse. Many-Body Localization and Thermalization in Quantum Statistical Mechanics. *Annual Review of Condensed Matter Physics*, 6(1):15–38, 2015.
- [109] P. W. Hess, P. Becker, H. B. Kaplan, A. Kyprianidis, A. C. Lee, B. Neyenhuis, G. Pagano, P. Richerme, C. Senko, J. Smith, W. L. Tan, J. Zhang, and C. Monroe. Non-thermalization in trapped atomic ion spin chains. *Phil. Trans. R. Soc. A*, 375:20170107, 2017.
- [110] A. del Campo and W. H. Zurek. Universality of phase transition dynamics: Topological defects from symmetry breaking. *Int. J. Mod. Phys. A*, 29:1430018, 2014.
- [111] D. Abanin, W. D. Roeck, W. W. Ho, and F. Huveneers. A Rigorous Theory of Many-Body Prethermalization for Periodically Driven and Closed Quantum Systems. *Commun. Math. Phys.*, 354:809–827, 2017.

- [112] J. C. Halimeh, V. Zauner-Stauber, I. P. McCulloch, I. de Vega, U. Schollwöck, and M. Kastner. Prethermalization and persistent order in the absence of a thermal phase transition. *Phys. Rev. B*, 95:024302, Jan 2017.
- [113] M. C. Tran, A. Ehrenberg, A. Y. Guo, P. Titum, D. A. Abanin, and A. V. Gorshkov. Locality and heating in periodically driven, power-law-interacting systems. *Phys. Rev. A*, 100:052103, Nov 2019.
- [114] F. Machado, D. V. Else, G. D. Kahanamoku-Meyer, C. Nayak, and N. Y. Yao. Long-range prethermal phases of nonequilibrium matter. *Phys. Rev. X*, 10:011043, Feb 2020.